Development of confocal microscope for polarimetry of semiconductor nano-structures

Meryem Benelajla

THÈSE

En vue de l'obtention du

DOCTORAT DE L'UNIVERSITÉ DE TOULOUSE

Délivré par l'Institut National des Sciences Appliquées de Toulouse

---

Présentée et soutenue par

Meryem BENELAJLA

Le 3 novembre 2020

Développement d'un microscope confocal pour la polarimétrie des nanostructures semi-conductrices

---

Ecole doctorale : **SDM - SCIENCES DE LA MATIERE - Toulouse**

Spécialité : **Physique**

Unité de recherche :

LPCNO-IRSAMC - Laboratoire de Physique et Chimie des Nano-Objets

Thèse dirigée par

Bernhard URBASZEK

Jury

M. Jean-Jacques Greffet, Rapporteur
M. Olivier Krebs, Rapporteur
Mme Isabelle Philip, Examinatrice
M. Vincent Paillard, Examinateur
M. Khaled Karrai, Examinateur
M. Bernhard Urbaszek, Directeur de thèse

Acknowledgements

"Ce que l'on conçoit bien s'énonce clairement,
et les mots pour le dire arrivent aisément." Nicolas Boileau-Despréaux

It is my pleasure to acknowledge the members of my thesis committee: Jean-Jacques Greffet, Olivier Krebs, Isabelle Robert-Philip, Vincent Paillard, Khaled Karrai, Bernhard Urbaszek for generously offering their time, support, guidance and good will throughout the preparation and review of this document.

This journey would not have been possible without the support of my family, professors and mentors, and friends. I spend in total three years at the company attocube systems, including my secondments at the Laboratoire de Physique et Chimie des Nano-Objets. Those years have been rich in scientific achievements. I had the chance to cross the way of many interesting and exciting people without whom this thesis would not have been possible.

Most of all, I would like to express my gratitude to my supervisor at the company attocube; Prof. Khaled Karrai for his continuous support, patience, motivation, enthusiasm, and immense knowledge. Your insightful feedback during the planning and development of this research work pushed me to sharpen my thinking and brought my work to a higher level. Your willingness to help at any time has been very much appreciated. Thank you for all the opportunities you provides me and all the work methods I learned at your contact during those 3 years. I will keep a very good memory of that workshop on Lake Achensee in Austrian Alps. I very much enjoyed walking in the panoramic view of the lake and mountains and breathe in the fresh, clean air. Encore une fois, merci beaucoup Khaled!

My grateful thanks are also extended to my supervisor at the University of Toulouse; Prof. Bernhard Urbaszek who has provided me with extensive personal and professional guidance throughout the duration of my Ph.D. thesis. Your valuable advice, ingenious recommendations and profound belief in my work were a key element that allows me to achieve a successful thesis with a many scientific results and a lot of new experiences. I had a wonderful memorable time in Toulouse that I will never forget. I enjoyed our walking tour together with Shivangi very much and all the tasty local food especially the Homemade Waffles with Salted Caramel Sauce. Ein letzes mal, vielen dank Bernhard!

My sincere thanks to R. Warburton, M. Kroner, L. Novotny, Alexander Högele, Massimo Gurioli, Elena Kammann and C. Schaefermeier for useful discussions and valuable suggestions. This research project has received funding from the European Union's Horizon 2020 research and innovation programme under the Marie Skłodowska-Curie grant agreement No721394 ITN 4PHOTON. Thank you 4PHOTON team for the wonderful meetings and workshops. It was a perfect mix of topics, people, science and social gathering!

My special gratitude to many people I met, worked with; who helped me in different ways throughout my studies. I tried to list them all but I probably forget some, thank you, everyone, and please accept my apologies!

- attocube colleagues: E. Kammann, C. DalSavio, C. Schaefermeier, J. Lindlau, H. Thierschmann, S. Vadia, C. K. V. Grundherr, P. Kuehnemann, G. Wuest, K. Grafenstein, S. Muller, T. Maier, P. Leubner, P. Kellner, I. Park, T. Rind, O. Seidel, A. Schmidt, M. Matheus, T. Lesnicar, N. Grill, K. Hoefling, Y. Heubeck, L. Zierl, A. Reuter, V. Dahlmeier, F. Otto, K. Bittner, K. Simi, B. Sipos, V. Kuemmerling, G. Schindler, S. Oberbauer, M. Bacani, T. Linderberg, V. Gentz, E. Trommer, M. Potsi, A. Piccolo, F. Valmorra.

- LPCNO colleagues: S. Shree, B. Han, X. Marie, C. Robert, T. Amand, D. Lagarde, H. Fang, G. Wang, E. Courtade, I. Paradeisanos, M. Manca, P. Renucci, L. Lombez, A. Balocchi, H. Carrere, L. Ren, J. Rajagopal, H. Tornatzky, J-F. Leherissier, B. Lassagne, T. Blon and É. Palleau.

- 4PHOTON colleagues: S. Stanguinetti, S. Bietti, S. Soubes, R. Waburton, L. Zhai, A. Tartakovskii, A. Fognini, A. Guardiani, A. Tuktamyshev, B. Giorgios, D. Toliopoulos, G. Bester, G. Pirard, H. Cristian, H. Liu, J. Muller, L. Ranasinghe, M. Abbarchi, M. Gurioli, M. Flatte, M. Glazov, P. Sheard, P. M. Koenraad, P. Zotev, P. A. Wronski, S. Dorenbos, S. Hofling, V. Zwiller, W. Hansen, A. Ludwig, D. Ritchie, R. S. R. Gajjela, A. Cruz, A. Shields, R. M. Stevenson.

Meryem

Abstract

Confocal microscopy is an essential imaging tool for biological systems, in solid-state physics and nano-photonics. Using confocal microscopes allows performing resonant fluorescence experiments, where the emitted light has the same wavelength as the excitation laser. Theses challenging experiments are carried out under linear cross-polarization conditions, rejecting laser light from the detector. In this work, we uncover for the first time the physical mechanisms that are at the origin of the yet unexplained high polarization rejection ratio which makes the resonant fluorescence measurements possible. We show in both experiment and theory that the use of a reflecting surface (i.e. the beam-splitter and mirrors) placed between two polarizers in combination with a confocal arrangement explains the giant cross-polarization extinction ratio of 10^8 and beyond. We map the modal transformation of the polarized optical Gaussian beam. We find an intensity "hole" in the reflected beam under cross-polarization conditions. We interpret this as a manifestation of the Imbert-Fedorov effect. We confirm these experimental findings for a large variety of commercially available mirrors and polarizers, allowing their practical implementation in many experiments.

Learning from this first part, we moved our exploration to a more fundamental aspect of optics in order to test the predictive power of the model. The Imbert-Fedorov shift, also known as "spin-Hall effect of light", was first measured for a laser beam of circularly polarized light in a glass prism under total internal reflectivity condition. Depending on the chirality of its circular polarization, the trajectory of a circularly polarized beam will shift above or below the plane of reflectivity when reflected off a surface. This shift is due to spin-orbit coupling of light upon each reflection and is normally very small, typically, several order of magnitudes smaller than the photon wavelength. For this reason, it has previously required using complex detection schemes limiting detailed experimental investigations. Here, we report about a novel method to measure and map the Imbert-Fedorov shift based on a dark-field cross-polarization technique in a confocal arrangement. In our proposed dark-field configuration in circular polarization, the majority photons reflected off a silver surface that are not contributing to the shift are filtered-out. The minority photons possess the proper chirality for spin-orbit coupling enabling this way the magnification of the Imbert-Fedorov shift by several orders of magnitudes. We verified that the out of plane of incidence shift measured this way is a direct consequence of the conservation of total angular momentum. Building on our detailed model for Gaussian beams derived for the first part of this work we have verified quanti-

tatively experimentally that the shift increases significantly when decreasing the angle of incidence, this, to the best of our knowledge, is a novel regime that was not explored previously. The analytical model show an excellent agreement with our measurements performed on high reflectivity metals such as silver. In particular, the model reveals clearly a regime of lower angle of incidence below which the simplistic approach of quasi plane wave would lead to an unphysical divergence of the shift at vanishing angles. In such a low angle regime, our model eliminates this shift divergence and predicts instead a modal transformation of the reflected minority photons to the next higher Hermite-Gaussian mode in a way very similar to that explored in the first part of this work. First data indicate the transition into such a regime.

Finally, this work opens the way to methodical design of sensitive laser resonant-fluorescence microscopes with extreme background extinction, for a broad range of applications in quantum optics and solid-state physics. The new methods developed here can also be applied for measuring material optical properties.

Résumé

La microscopie confocale est un outil d'imagerie essentiel pour les systèmes biologiques, en physique du solide et en nano-photonique. L'utilisation d'un tel microscope permet de réaliser des mesures de fluorescence résonante, où la lumière émise a la même longueur d'onde que la source. Ces mesures difficiles sont menées en condition de polarisation croisée linéaire, rejetant la lumière laser du détecteur. Dans ce travail, nous expliquons pour la première fois les mécanismes physiques du taux de rejet de polarisation élevé encore inexpliqué qui rend possible les mesures de fluorescence résonante. Nous montrons à la fois dans l'expérience et la théorie que l'utilisation d'une surface réfléchissante (le séparateur de faisceau et les miroirs) placée entre deux polariseurs en combinaison avec un arrangement confocal explique le taux d'extinction géant de 10^8 et au-delà. Nous illustrons la transformation modale du faisceau gaussien polarisé. Nous trouvons un «trou» d'intensité dans le faisceau réfléchi dans ces conditions. Nous interprétons cela comme une manifestation de l'effet Imbert-Fedorov. Nous confirmons ces résultats pour une grande variété de miroirs et polariseurs disponibles dans le commerce, permettant leur mise en œuvre pratique dans de nombreuses expériences.

Par la suite, nous avons exploré un aspect plus fondamental de l'optique pour tester notre modèle. Le décalage d'Imbert-Fedorov, également connu comme l'«effet de spin-hall de la lumière», a d'abord été mesuré pour un faisceau laser de lumière polarisée circulairement dans un prisme de verre en condition de réflectivité interne totale. En fonction de la chiralité de sa polarisation, la trajectoire d'un faisceau polarisé circulairement se déplacera au-dessus ou au-dessous du plan de réflectivité lorsqu'il est réfléchi sur une surface. Ce décalage est dû au couplage spin-orbite de la lumière à chaque réflexion et est normalement très petit, typiquement, plusieurs ordres de grandeur plus petits que la longueur d'onde du photon. Pour cette raison, il était auparavant nécessaire d'utiliser des schémas de détection complexes limitant les investigations expérimentales. Ici, nous rapportons une nouvelle méthode pour mesurer et illustrer ce décalage basée sur une technique de polarisation croisée en champ sombre dans un arrangement confocal. Dans cette configuration, la majorité des photons réfléchis par le miroir qui ne contribuent pas au décalage sont filtrés. Les photons minoritaires possèdent la chiralité appropriée pour le couplage spin-orbite permettant ainsi le grossissement du décalage de plusieurs ordres de grandeur. Nous avons vérifié que le décalage hors plan d'incidence mesuré de cette manière est une conséquence directe de la conservation du moment cinétique total. En se basant

sur notre modèle dérivé en première partie, nous avons vérifié expérimentalement que le décalage augmente de manière significative en diminuant l'angle d'incidence, ceci, à notre connaissance, est un nouveau régime qui n'a pas été exploré. Le modèle montre un excellent accord avec nos mesures effectuées sur un mirror métallique. En particulier, le modèle révèle un régime d'angle d'incidence inférieur en dessous duquel l'approche simpliste de la quasi-onde plane mène à une divergence non physique du décalage. Dans un tel régime, notre modèle élimine cette divergence de décalage et prédit une transformation modale des photons minoritaires réfléchis vers le mode Hermite-Gaussien supérieur suivant d'une manière similaire à celle explorée dans la première partie de ce travail. Les premières données indiquent la transition vers un tel régime.

Enfin, ces travaux ouvrent la voie à la conception méthodique de microscopes à fluorescence résonante laser sensibles à extinction de fond extrême, pour une large gamme d'applications en optique quantique et en physique du solide. Les méthodes développées ici peuvent également être appliquées pour mesurer les propriétés optiques des matériaux.

Contents

Chapter 1

Resonant spectroscopy: the motivation to go beyond instrument's limit

Adapted from [1]:
Meryem Benelajla, Elena Kammann, Bernhard Urbaszek, and Khaled Karrai, **"The physical origins of extreme cross-polarization extinction in confocal microscopy"**, arXiv:2004.13564 (2020).

1.1 Introduction

In optical spectroscopy experiments it is crucial to excite an emitter with a laser very close to its transition energy. Experiments under resonant excitation are essential for accessing the intrinsic optical and spin-polarization properties of large class of emitters [2–7]. Using linear cross-polarization in a confocal setup has been successfully employed as a dark-field method to carry out resonant fluorescence experiments to suppress scattered laser light, with the added benefit of high spatial resolution [8, 9]. Resonant fluorescence experiments allow crucial insights into light-matter coupling, such as the interaction of a single photon emitter with its environment [10], with optical cavities [11] and also studying single defects in atomically thin materials such as WSe_2 [12]. Dark-field confocal techniques allow developing single photon sources with high degrees of photon indistinguishability [13–15] and longer coherence [16]. In practice dark-field laser suppression is not just a spectroscopy tool, it is also a key part of more matured quantum technology systems [17].

Despite many advances based on experiments in confocal microscopes with cross-polarization laser rejection, the physical mechanisms that make these experiments possible are not well understood, hampering further progress in this field. The key figure of merit is the suppression of the excitation laser background by at least six orders of magnitude. Indeed a suppression by a factor of 10^8 [18] up to 10^{10} (this work) has been measured. But this is very surprising as mirrors and beam-splitter in such a system reduce the theoretical extinction

limit to the 10^3 to 10^4 range.

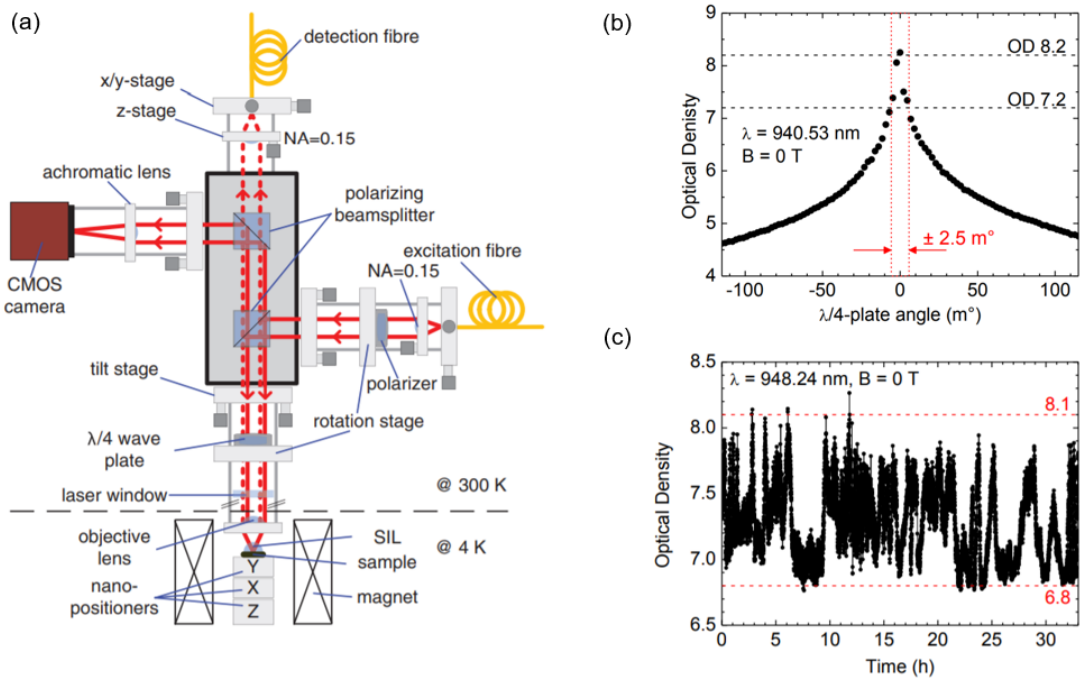

Figure 1.1: *taken from [18].* (a) Microscope setup for resonance fluorescence experiments on a single InGaAs quantum dot. (b) Sensitivity of the laser suppression to the quarter-wave plate angle. (c) Long-term behaviour. The optical density (OD), defined as $OD = -log(1/T)$ with transmission T, is plotted as a function of time. The microscope is stable over many hours with an $OD > 6.8$.

In this work we explain the physics behind the giant enhancement of the extinction ratio by up to seven orders of magnitude that make microscopy based on dark-field laser suppression possible. The measurements of resonant fluorescence are typically performed in an epifluorescence geometry [18], for which laser excitation and fluorescence collection are obtained through the same focusing lens. This involves necessarily the use of a beam-splitter orienting the back-reflected light containing the fluorescence towards a detection channel as depicted in Fig. 1.1. The back-reflected laser is suppressed by rotating a quarter-wave plate, switching between laser rejection maximally on and maximally off. The implementation of this scheme Fig. 1.1(a) demonstrated an impressively high suppression of laser excitation background in excess of a factor of 10^8 (Fig. 1.1. (b) and (c)) corresponding to an optical density OD=8. Fig. 1.1. (b) shows that this giant extinction depends on the quarter-wave plate angle and a change of only few mdeg can decrease the level of background rejection by one order of magnitude. In another words, this emphasizes the need for a mdeg rotation resolution and an extreme control of polarization to be able to perform a resonance fluorescence experiments on quantum emitters.

In our work we identify two key ingredients that explain the giant amplification of the cross-polarization extinction ratio: (i) a reflecting surface (i.e.

the beam-splitter) placed between a polarizer and analyzer, and (ii) a confocal arrangement. We demonstrate giant extinction ratios in our experiments for different mirrors (silver, gold, dielectric, beam-splitter cubes) and polarizers (Glan-Taylor, nanoparticle thin films). We demonstrate that behind this general observation lies the intriguing physics of the Imbert-Fedorov effect [19, 20], which deviates a reflected light beam depending on its polarization helicity. We discover that a confocal arrangement not only amplifies the visibility of the Imbert-Fedorov effect dramatically, taking it from the nanometer to the micrometer scale, but also exploits conveniently the symmetry of the newly observed Imbert-Fedorov modes to insure that the cross-polarized laser beam is not coupled, explaining the near complete suppression of the laser background signal. In other words, we cannot treat the spatial (i.e. modal) and polarization properties of light separately in our dark-field confocal microscope analysis. In addition to new developments in dark-field microscopy our experiments provide powerful tools to understand spin-orbit coupling of light [21–23], in the broader context of topological photonics [22, 23].

In our work we setup a robust, highly reproducible experiment and derive a convenient classical formalism to investigate these remarkable effects at the cross roads of quantum optics and topological photonics.

1.2 Scope of the thesis

The thesis is structured as follows, in chapter 2 we introduce the confocal microscope setup with polarization extinction, confocal microscope design for cryogenic spectroscopy is discussed in section 2.1, the simplified confocal arrangement for cross-polarization extinction measurement is described in section 2.2. Cancellation of polarization leakage is measured and discussed in a first simplified model in chapter 3. The modal transformation of a reflected Gaussian beam is analyzed in chapter 4. Direct imaging of the Imbert-Fedorov shift effect using circular polarization state of light is presented in chapter 5.

Chapter 2

Confocal microscope setup with polarization extinction

Adapted from [24]:
Meryem Benelajla, Elena Kammann, Bernhard Urbaszek, and Khaled Karrai
"Modal imaging of a laser Gaussian-beam reflected off a surface",
Proceedings Volume 11485, Reflection, Scattering, and Diffraction from Surfaces VII; 114850E (2020).

In this chapter we start by describing the attocube fiber-based confocal microscope instrument for nanoscale spectroscopy at cryogenic temperatures and in high magnetic fields (section 2.1.1). As a demonstration of the microscope performance, applications in the spectroscopy of single quantum emitters are presented in section 2.1.2. The confocal microscope presented in section 2.1 is designed to obtain a high polarization extinction ratio with a convenient switching between laser rejection maximally on and maximally off. Section 2.2 describes the simplified confocal arrangement we used in order to focus on the most relevant physics leading to extreme laser rejection. A detailed description of the optical elements contained in the experimental setup is also presented.

2.1 Confocal microscope for cryogenic spectroscopy

2.1.1 Optical design

Experiments on semiconductor nanostructures present challenging demands on the optical system. It requires low temperature, high spatial resolution, mechanical stability and magnetic field. This features could be performed by attocube's commercial confocal microscope *attoCFM* and *attoDRY*1000 cryostat, as depicted below:

Figure 2.1: The attocube fiber-based confocal microscope *attoCFM* and *attoDRY*1100 cryostat. (1) Collimator. (2) *FC/APC* coupled single mode fiber to/from excitation laser or detector/spectrometer. (3) Beam-splitter position easily switchable from outside. (4) Two additional filter mounts on beam-splitter cube. (5) Beam-splitter options. (6) Optional: polarizing beam-splitter cube. (7) Optional: non-polarizing beam-splitter cube. (8) Filter drawer. (9) Theta/phi mirrors for each channel easily adjustable from the outside.

The low temperature *attoCFM* has been designed to provide the user a maximum amount of flexibility and convenient operation. The head of the microscope consists of two main channels which allow the excitation and detection of optical signals. The microscope optical train typically consists of a commercially available collimator, filters, mirrors, beam-splitter cubes, microscope objective, detector, and single mode fibers are used as pinholes to connect the microscope to the excitation source and detection channel. Spatial resolution is crucial for spectroscopy measurements. This is achieved using attocube piezo-driven positioners that allow a precise movement of $10nm$ in x, y, z directions, even at low temperature and strong magnetic fields. The spatial resolution is generally related to the microscope objective numerical aperture for which the collection

efficiency may vary from one wavelength to the other due to chromatic aberration effect. The use of attocube objective $LT-APO$ solves the problem.

Despite the fact that some optical spectroscopy experiments are conducted at room temperature, low temperature measurements are of strong interest to study in fine details the intrinsic optical properties of a large class of quantum emitters [2–6]. This feature is fully enabled by attocube $attoDRY1100$ helium free cryostat with different base temperatures down to $300mK$. In this system, the helium is used as a gas and is then liquefied in a closed cycle following a standard thermodynamic processes of compression and cooling.

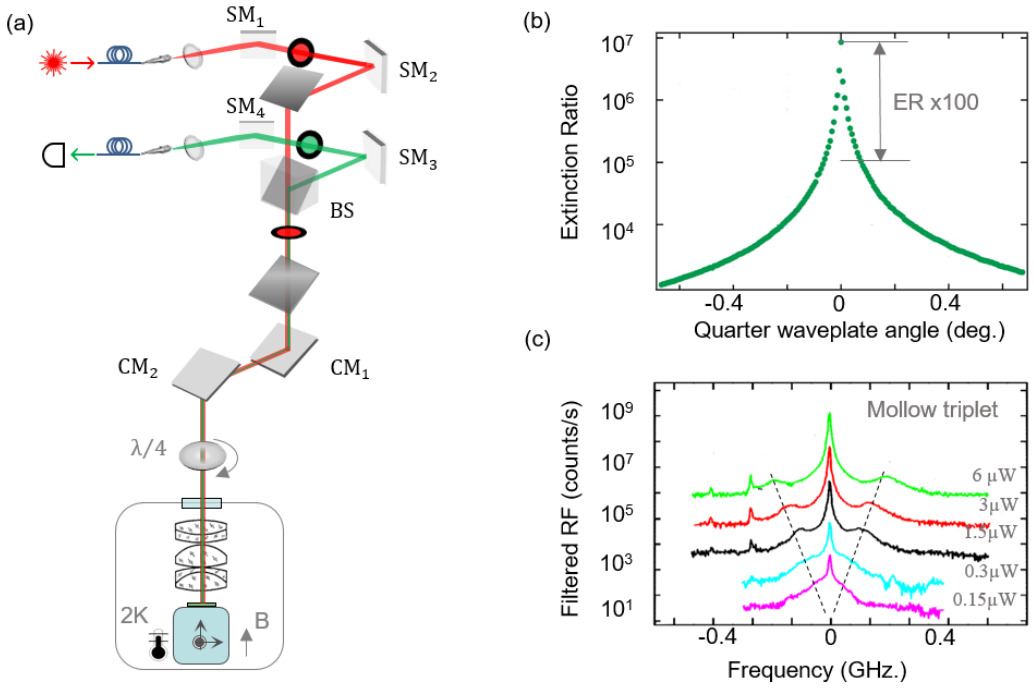

Figure 2.2: (a) Schematic drawing of the low temperature attoCFM where sample is mounted on a x,y,z piezo-driven nanopositioners as explained in the text. (SM), (CM) denote steering and coupling mirrors respectiveley. ($\lambda/4$) quarter-wave plate mounted on a piezo-driven rotator to control the state of polarization (b)The extinction ratio plotted as a function of the angle of the quarter-wave plate. In a narrow angular region of about 30 mdeg the extinction exceeds six orders of magnitude ultimately demonstrating the need for high resolution piezo-driven rotators. (c) Mollow triplet of a two-level system at resonant excitation. Measured spectra of the quantum dot resonance fluorescence signal for different excitation powers starting from 0.15 μW until 6 μW. The two side peaks move away from the central peak with increasing excitation power.

The schematic drawing of such microscope is shown in Fig. 2.2.(a). A laser light from a single mode fiber is collimated and is transmitted through a linear polarizer so as to define the excitation polarization state. Next, the laser light is reflected by several mirrors and beam-splitter cubes. It is then focused on a sample by an achromatic low temperature objective. The back reflected light from the sample is collimated through the same objective, and is transmitted

through a second linear polarizer (analyzer) to define the detection polarization state. Another collimator focuses the light beam onto a single mode fiber for detection. A quarter-wave plate aligned with both polarizer and analyzer, is used for controlling the state of polarization and also for compensating any distortion from linear to elliptical polarization in the excitation and detection polarization states. In this case, the quarter-wave plate allows for switching between transmission and laser rejection mode.

2.1.2 Application to nanoscale spectroscopy

Resonant fluorescence was a long-term experimental challenge as it is difficult to discriminate between the emitted light and the excitation laser. This difficulty has been successfully overcome over the past decade using linear cross-polarization in a confocal setup as a dark-field method to suppress scattered laser light from the detector. In our case, the confocal microscope with its complex design enabled us to achieve a level of laser background suppression of 7 orders of magnitude, a factor 10 away from the work [18]. Fig. 2.2.(b) is a plot of the polarization extinction ratio as a function of the angle of the quarter-wave plate which is mounted on an high precision rotator allowing a mdeg rotation resolution. Further, we define the polarization extinction ratio (ER) as the ratio of minimum to maximum transmission of an impinging laser beam whose electric field direction is either parallel (p-polarized) or orthogonal (s-polarized) to the plane of incidence. More interestingly, we conducted a resonance fluorescence measurements on single quantum dots with such system. Fig. 2.2.(c) correspond to the resonant quantum dot emission filtered through a high finesse scanning Fabry-Pérot spectral filter. It reveals two side peaks which move away from the central peak with increasing excitation powers starting from 0.15 μW until 6 μW. The resulting fluorescence spectrum of a two-level system driven by a resonant incident field is known as a Mollow triplet [25].

2.1.3 Conclusion

Following this brief overview, it can be noticed that mirrors and beam-splitter cubes are commonly used for applications in confocal fluorescence microscopy under both resonant and non-resonant excitation source. Non-resonant excitation introduces spin and charge noise leading to dephasing and decoherence of optical and spin states [16]. Compared to photoluminescence [26], resonant fluorescence measurement enables the generation of indistinguishable single photons of high fidelity [17]. Further, it allows a spin to be initialized, coherently manipulated, and read-out optically [2–7]. In the next section, we introduce a simplified optical confocal microscope arrangement to enhance by several orders of magnitude the otherwise normally best achievable laser extinction, making this way the resonant fluorescence experiments possible .

2.2 Confocal arrangement for cross-polarization extinction

2.2.1 Confocal setup design

We used a simplified confocal arrangement as depicted in Fig. 2.3a,b in order to focus on the most relevant physics leading to extreme laser rejection. A diode laser beam (1) at $\lambda = 905\ nm$ wavelength is launched into a single mode fibre (2). The light emerges from the 4° angled flat-polished end with a nearly perfect Gaussian beam with $\omega_f = 2.5\ \mu m$ mode waist radius at $1/e^2$ of the maximum intensity. A diffraction limited microscope objective (3) of numerical aperture NA= 0.25 and focal length of $f = 26\ mm$ focused on the fiber end collimates the light into a 3 mm waist radius Gaussian beam. We choose the NA to be significantly larger than the diverging beam half-angle out of the fiber in order to preserve the Gaussian quality of the beam.

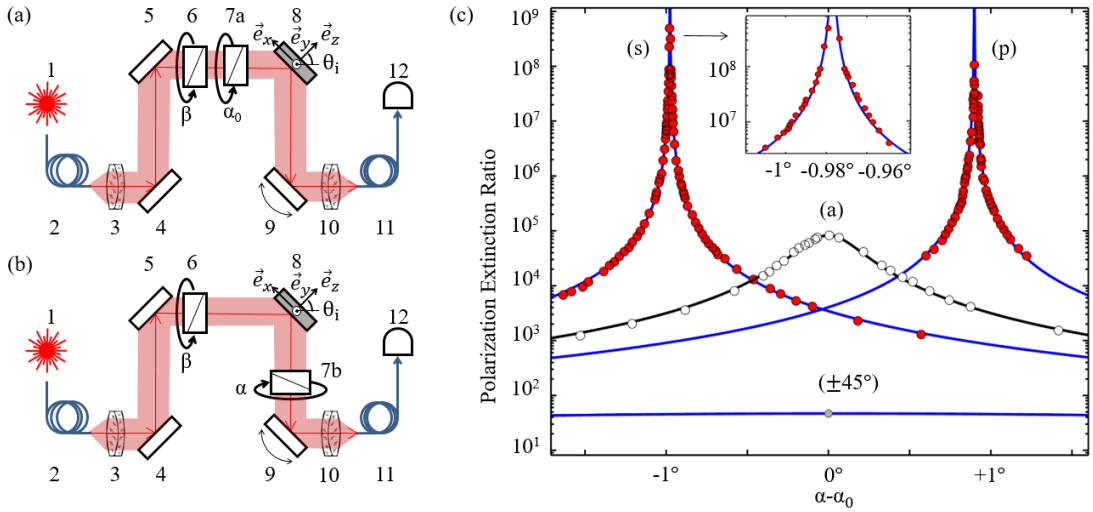

Figure 2.3: (a)(b) Cross-polarization extinction setup in a confocal microscope arrangement setup as described in the text. (c) Measured and modeled linear polarization extinction ratio for both *p*- and *s*-polarized beam around cross-polarization conditions obtained by placing the analyzer before (panel (a)) and after (panel (b)) a protected silver mirror. A giant extinction enhancement of more than 3 orders of magnitudes is obtained in configurations *s*- and *p*- with the reflecting surface placed between crossed polarizers. The inset is a magnification of the polarization extinction near maximum for the *s*-polarization. An angular shift of the location of maxima of extinction is systematically found for the *s*- and *p*-polarization with respect to the reference. (±45°) Measured and modeled linear polarization extinction ratio for ±45° linearly polarized beam around cross-polarization conditions obtained by placing the analyzer after (panel (b)) a protected silver mirror.

A pair of mirrors (4,5) mounted on two axis tilt-stages allows for fine steering

of the collimated beam axis. Next the beam travels to a linear polarizer (6) oriented at an angle β and mounted on a piezoelectric stepping stage rotating with 20 μrad resolution around the optical axis. The beam travels then towards a mirror (8), the key element of this experiment, either by passing first through an analyzing polarizer (Fig. 1.1a) oriented at an angle α_0 for the control measurement (7a), or by passing through the analyzer oriented at an angle α after a reflecting surface for the test experiment (7b). We mounted the analyzer also on a piezo stepper fine rotation stage. The mirror (9) mounted on two-axis piezo controlled tilt stage steers the beam into a microscope objective (10) identical to (3) focusing the light into the core of a single mode fiber (11) identical to (2) allowing for Gaussian TEM_{00} modal confocal filtering and optical detection (12) at the other end of the $5m$ fiber cable.

2.2.2 Confocal setup concept

This confocal arrangement simulates the essential components of the resonant fluorescence confocal microscopes. The reflecting surface plane (8) at 45° of incidence, defines the standard p and s state of polarization with projections along $\vec{e}_x$ and $\vec{e}_y$ respectively. The reflecting test surfaces in position (8) of Fig. 2.3a,b we used in this work were commercial protected silver, aluminum and dielectric high reflectivity Bragg mirrors, evaporated gold film, as well as non-polarizing beam-splitter cubes. All such reflecting surfaces are typically used in diffraction limited confocal microscopes. The results were qualitatively very similar for all these reflecting surfaces. We choose to show here the data measured with silver mirrors only, this with the exception of data measured for comparison on a glass surface reflecting from air as discussed at chapter 4.

We now discuss the measurements in the configuration shown in Fig. 2.3b, for which the reflecting test surface is sandwiched between the polarizer and the analyzer. First, the polarizer angle β is adjusted near 0 or $\pi/2$, for p- or s-polarization respectively, while setting the analyzer angle α near cross-polarization at $\beta \pm \pi/2$. Then the polarizer and analyzer are subsequently finely rotated to reach maximum extinction at values β and α respectively. Once the optimization reached, β remains untouched and the analyzer in its rotator is subsequently placed before the reflecting surface just after the polarizer for our control extinction measurement (Fig. 2.3 a). The analyzer angle must be then be adjusted to a new value α_0 in order to recover maximum nominal extinction specification inherent to the polarizers; α_0 defines then the p or s reference. The extinction data measured as a function of the analyzer angle α in reference to α_0 are shown in Fig. 2.3c for the control measurement (Fig. 2.3a) as well as for the p- and s-polarizations in the configuration (Fig. 2.3b). Two striking observations stands out. (i) For all the tested reflectors indicated above, the extinction ratio obtained this way was enhanced beyond the 10^8 range when the test mirror surface was sandwiched between the polarizer and the analyzer, reducing this way significantly the polarization leakage of the polarizers. (ii) The analyzer angle for maximum extinction is shifted away from α_0 by $+0.898°$ and $-0.977°$ for the p- and s-polarization respectively, a significant angular deviation given our resolution of about 10^{-3}

deg. In the chapter 3, we provide a first explanation for these two striking observations.

2.2.3 Confocal setup realization

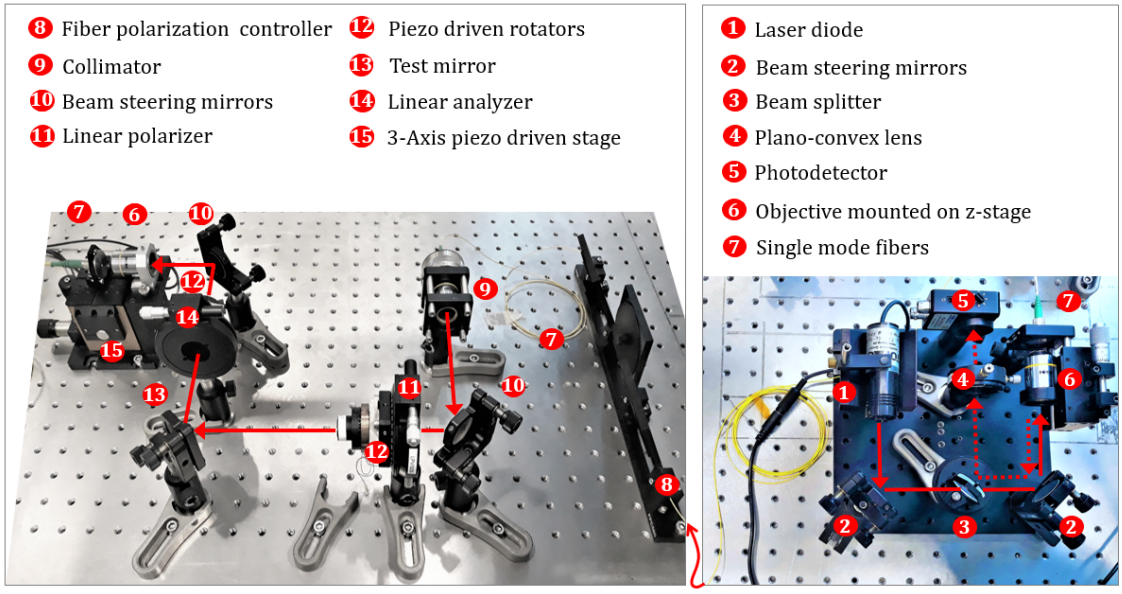

Figure 2.4: Experimental realization of the cross-polarization extinction setup in a confocal arrangement (left). Coupling of the laser source is done in a separate step (right). Red solid and dashed lines indicate the excitation and the reflection ray path respectively as explained in the text.

The exact realization of the schematic design described in section 2.2.1 is shown in Fig. 2.4. The unit on the right of Fig. 2.4 is used for coupling the laser beam into the single mode fiber (7). The unit on the left corresponds to the basic confocal arrangement used later in this work for polarization extinction measurement and mode imaging. Alignment procedure of both units is explained in next section 2.2.4. In what follows, we discuss and characterize all necessary components for our experiment, like coupling unit, test surfaces (including mirrors and beam-splitter cube), detector, polarizers and rotators.

Beam steering mirrors
In both units, we implement a beam-walk technique using a pair of protected silver mirrors (2,10) (Thorlabs mirrors, protected silver PF10-03-P01 - Ø1) with a reflectance higher than 96% for laser wavelength 905 *nm* (Fig. 2.4). This process is used to ensure that the laser beam is aligned and it involves a successive adjustment of the two steering mirrors in such a way that a maximum intensity is reached at the detector.

Test surfaces
The reflecting test surfaces in position (13) of Fig. 2.4 (left) we used in this work

were commercial protected silver (Thorlabs mirror, protected silver PF10-03-P01 - Ø1), aluminum (Thorlabs mirror, aluminum PFSQ20-03-G01) and dielectric high reflectivity Bragg mirrors (Thorlabs mirror, dielectric BB1-E03 - Ø1), evaporated gold film (Thorlabs mirror, gold PF10-03-M03), as well as non-polarizing beam-splitter cubes (Thorlabs non-polarizing cube beam-splitters 30:70). All such reflecting surfaces are optimized for the laser wavelength 905 nm and typically used in diffraction limited confocal microscopes.

Objectives
In both units, we use same objectives (Olympus Plan Achromat Objectives, NA =0.25, $f = 26mm$) for beam collimation or for focusing the laser light into single mode fibers. The collimation of the light beam is optimized by means of a retroreflector (Thorlabs, TIR Retroreflector Prisms PS975-M) which we place just after the collimator (9) and before the mirror (10). The dashed line in Fig. 2.4 (right) indicates the reflection ray path. Then, the light beam is again focused by the collimation objective (9) onto the single mode fiber (7) and is back-reflected into the laser coupling unit. We used a beam-splitter (3) with a transmission ratio of 70:30, a plano-convex lens (4) (Thorlabs LA1131, $f = 50\ mm$) and a photodetector (5) (Thorlabs PDA36A-EC - Si Switchable Gain Detector, 350 - 1100 nm) with internal gain to check the reflected light. Next, the z-position of the collimation objective (9) is finely adjusted until maximizing the signal on the detector. Indeed, the focal plane of the objective coincides with z-position for which all rays of light are focused into the single mode fiber and thus leading to a high signal value on the detector. Here, the focused spot waist radius i.e the fiber Gaussian mode size ω_f, is given by $\omega_f = \lambda f/\pi\omega_0 = 2.5\ \mu m$ with f is the focal length and $\omega_0 = 3mm$ is the beam radius of the collimated laser beam.

Polarizers and rotators
Selecting the appropriate polarizers enables excellent extinction ratio performance. For this experiment, we used the best quality commercial linear polarizers with an extinction in direct cross-polarization limited to 10^5 for nanoparticle thin film polarizer (Thorlabs LPVIS050) and to 10^6 for Glan-Thomson crystal polarizers (Thorlabs GTH10M). Both polarizers are mounted on a piezoelectric stepping stage rotating (attocube systems, ANR240/RT - rotator 360° endless) with 20 μrad resolution around the optical axis. A digital controlling unit (attocube systems, ANC 350 multi-functional piezo controller for driving attocube's rotators) is used to drive the rotators of the polarizer and the analyzer.

Detector
In this experiment, we used a photo-detector (Femto OE-200- Si-photodiode) which converts the incident optical signal into voltage. The resulted signal after photo-detection is measured on a voltmeter. The photo-detector is operating from fW to mW and has an adjustable conversion gain from 10^3 to $10^{11} V/W$ with a bandwidth up to 500 kHz. One of the most important measures that quantify the sensitivity of photo-detectors is the Noise Equivalent Power (NEP), usually expressed in Watts per square root of Hertz ($W/\sqrt{Hz}$). It corresponds

to the input signal power that results in a signal-to-noise ratio (S/R) of 1 in a 1 Hz output bandwidth. Basically, this represents the threshold above which a signal can be detected. For most detectors, the output noise density can be measured without incident light when the optical input is completely darkened. In our case, the signal is detected using an integration time 5 ms in a bandwidth $\Delta f = 200\ Hz$, with a detector of NEP down to $6 fW/\sqrt{Hz}$. The theoretical minimum detectable power using such detector is then $NEP \times \sqrt{\Delta f} = 84.85\ fW$.

2.2.4 Confocal setup alignment

The laser coupling unit (Fig. 2.4 (right)) is made of a diode laser beam (1) (TOPAG 3-5mW output power at 905 nm) of laser type 3R specified with a wavelength of 905 nm, microscope objective (6) mounted on a z-translation stage, beam steering mirrors (2) and a beam-splitter 70:30 (4). A photodetector (5) in combination with a plano-convex lens (4) (Thorlabs LA1131, $f = 50\ mm$) will be used for measuring the coupling of the laser in the confocal arrangement Fig. 2.4(left). Laser coupling can pose many challenges, like optical distortions and losses. First, we start with measuring the laser power output using a power meter sensor, the measured power before mirror (2) is about $5mW$. The objective (6) is connected to a single mode fiber (7) which is placed in polarization paddles (8) (Thorlabs Manual fiber polarization controllers FPC560) to control the random polarization of the light inside the fiber. Next, a beam-walk technique is implemented by means of mirrors (2) to ensure a maximum output intensity at the collecting fiber (7). The measured laser power at the output of the fiber polarization controller is about $P_0 = 1\ mW$. After the laser coupling is done, the collimating and collecting objectives of the confocal arrangement (Fig. 2.4(left)) are aligned with respect to the optical axis by means of a z-translation stage. The measured laser power after collimator (9) and before mirror (10) is about $70\%P_0$ which means that the lens causes 23% loss of light at the laser wavelength 905 nm. Then, a beam-walk technique is again used to ensure that the laser beam is aligned. The laser power after all mirrors (without any polarizers) and after focusing into the fiber (6) (Fig. 2.4(left)) is about $50\%P_0$. This value is good enough for performing our experiment, but it is possible to reach an output power of more than 0.5 mW, by using high power industrial fiber lasers to avoid coupling losses in fiber optic.

2.2.5 Conclusion

In conclusion, we can comment that the confocal arrangement has a simplistic design but it requires a high degree of polarization control and alignment precision. In particular, the measured cross-polarization extinction was for a long time experimentally limited to 10^8 value. Considerable progress has been made over the last year of the Ph.D. and we have reached a record level of about 10^{10} for which the limiting factor was the dark noise of our detector. This topic will be discussed further at the end of chapter 4. In next chapter, we will

explain the physical origins of the huge cross-polarization extinction in confocal microscopy.

Chapter 3

The physical origins of cancellation of polarization leakage

Adapted from [1]:
Meryem Benelajla, Elena Kammann, Bernhard Urbaszek, and Khaled Karrai, **"The physical origins of extreme cross-polarization extinction in confocal microscopy"**, arXiv:2004.13564 (2020).

3.1 Polarization leakage equation

Intuitively, the significant reduction of the polarization leakage field must find its root in a destructive interference effect. The first challenge towards finding an answer to our problem is to offer a model of the polarization leakage. In order to determine the light field at various planes such as after the polarizers and mirrors, we define a right hand coordinate system $\vec{p}$, $\vec{s}$ transverse to the optical beam propagation axis $\vec{p}\times\vec{s}$ according to the definition of p- and s-polarization with respect to the plane of incidence with the test surface (8) of Fig. 2.3b. For clarity, $\vec{s}\equiv\vec{e}_y$ is perpendicular to the incidence plane. In this section, we will test first the simplistic idea that the collimated laser beam can be approximated by a plane wave. We use a Jones matrices formalism projecting the field components along $\vec{p}$, $\vec{s}$ after each relevant optical element namely the matrix $\bar{\bar{P}}(\beta)$ of the polarizer, $\bar{\bar{M}}$ of the reflecting test surface and $\bar{\bar{A}}(\alpha)$ that of the analyzer. In this formalism an ideal linear polarizer along $\vec{p}$ and $\vec{s}$ is represented by

$$\bar{\bar{P}}_{p_0}=\begin{bmatrix}1 & 0\\ 0 & 0\end{bmatrix},\ \bar{\bar{P}}_{s_0}=\begin{bmatrix}0 & 0\\ 0 & 1\end{bmatrix} \tag{3.1}$$

We will assume now that a real physical linear polarizer along $\vec{p}$ or $\vec{s}$ represented by $\bar{\bar{P}}_p=\bar{\bar{L}}\bar{\bar{P}}_{p_0}$ and $\bar{\bar{P}}_s=\bar{\bar{L}}\bar{\bar{P}}_{s_0}$ respectively and is characterized by a polarizer leakage Jones matrix $\bar{\bar{L}}$. Many conditions result in the light leakage such as light scattering, misalignment of crossed polarizers, errors during the manufacturing process. The assumption we are making about the physical origin of the leakage is that it is due to lossless coherent scattering such as Rayleigh scattering inclusions in

the crystal. In particular, when light travels through a polarizing sheet made of nanoparticles chains, it interacts with the medium and this causes the scattering of light. Photons with a polarization direction along the chains are strongly absorbed, whereas the absorption is weak for the photons with a polarization direction perpendicular to these. Absorption causes the nanoparticles to vibrate and then re-emit the photons in random directions, but with same frequency and wavelength. Rayleigh scattering is a type of coherent scattering interaction which causes the transmitted light to be $(\pi/2)$ out of phase with the initial beam light. In this interaction, the energy of the scattering particles is not changed. The second assumption, which we verified experimentally, is that the leakage should be invariant upon an arbitrary angular rotation φ around the optical axis $\vec{p}\times\vec{s}$, namely $\bar{\bar{L}} = \bar{\bar{R}}(\varphi)\ \bar{\bar{L}}\ \bar{\bar{R}}(-\varphi)$ where the rotation matrix $\bar{\bar{R}}(\varphi)$ is given by

$$\bar{\bar{R}}(\varphi) = \begin{bmatrix} \cos\varphi & -\sin\varphi \\ \sin\varphi & \cos\varphi \end{bmatrix} \tag{3.2}$$

We choose to represent the polarization leakage by a matrix

$$\bar{\bar{L}} = \begin{bmatrix} a & ib \\ -ib & a \end{bmatrix} \tag{3.3}$$

where $a^2 + b^2 = 1$. Such a form is invariant upon rotation. For a high quality commercially available linear polarizer $a^2 \gg b^2$, which is the case in our setup since from our experiment we determine $a^2/b^2 \cong (1.5 \pm 0.5) \times 10^5$. This is the measured nominal leakage seen in Fig. 2.3c. We note that the formalism can also be extended to circular polarizers, in which case $a^2 \cong b^2$ and the leakage stems from the slight difference between the two terms.

We assume an incoming laser field $\vec{E}_p$ initially p-polarized that we rotate at an angle β aligning it with the polarizer such $\vec{E}(\beta) = \bar{\bar{R}}(\beta)\vec{E}_p$. This field first traverses the leaky polarizer also rotated at β such $\bar{\bar{P}}(\beta) = \bar{\bar{R}}(\beta)\ \bar{\bar{L}}\bar{\bar{P}}_{p_0}\ \bar{\bar{R}}(-\beta)$ followed by the mirror matrix $\bar{\bar{M}}$ and by the analyzer matrix rotated at an angle α namely $\bar{\bar{A}}(\alpha) = \bar{\bar{R}}(\alpha)\ \bar{\bar{L}}\bar{\bar{A}}_{p_0}\ \bar{\bar{R}}(-\alpha)$ so the field $\vec{E}$ just after the analyzer writes

$$\vec{E} = \bar{\bar{A}}(\alpha)\bar{\bar{M}}\bar{\bar{P}}(\beta)\bar{\bar{R}}(\beta)\vec{E}_p \tag{3.4}$$

The calculation, shown in detail in Appendix A.2. The mirror Jones matrix for a plane wave writes

$$\bar{\bar{M}} = \begin{bmatrix} r_p & 0 \\ 0 & r_s \end{bmatrix} \tag{3.5}$$

Where $r_{p,s}$ are the complex valued Fresnel reflectivity coefficients $r_p = (\epsilon cos\theta_i - \sqrt{\epsilon - sin^2\theta_i})/(\epsilon cos\theta_i + \sqrt{\epsilon - sin^2\theta_i})$ and $r_s = (cos\theta_i - \sqrt{\epsilon - sin^2\theta_i})/(cos\theta_i + \sqrt{\epsilon - sin^2\theta_i})$ [27] where the test surface material enters through its complex-valued dielectric function $\epsilon = \epsilon_1 + i\epsilon_2$ or equivalently its optical constant $n^2 = \epsilon$, which is tabulated

for noble mirror metals [28]. After a lengthy but straightforward calculation (Appendix A.3), we determine the light intensity just after the analyzer

$$I = a^2 \mid r_p \cos\alpha \cos\beta + r_s \sin\alpha \sin\beta \mid^2 + b^2 \mid r_p \cos\alpha \sin\beta - r_s \sin\alpha \cos\beta \mid^2 \\ - 2abIm(r_p r_s^*) \cos\alpha \sin\alpha \tag{3.6}$$

The polarization extinction ratio is then simply given by $1/I$. A practical check for $p(s)$ polarized light, namely for $\beta = 0(\pi/2)$ and the corresponding cross-polarization $\alpha = \pi/2(0)$ leads to the expected finite polarization leakage $I = b^2 \mid r_{p/s} \mid^2$. For a hypothetical perfect mirror, $r_p = 1$ and $r_s = -1$ making it in this idealized case $I = b^2$. Because the reflecting surface has real and imaginary components for r_s and r_p, equation (3.6) shows that for a "sufficiently small value" of b^2 we can always find a choice of angles α, β that leads to $I = 0$, canceling this way the undesired leakage. This is always true under condition of total internal reflection which is the case of a metallic mirror in the visible and infrared range and for a typical cube beam-splitter. A "sufficiently small value" of depolarization to obtain perfect cancellation means in the context of our work typically $b^2 < 6 \times 10^{-3}$ when using a silver mirror as we will derive later in the text. The reflecting test surface in combination with the polarizers rotation act to interfere destructively with the residual rotation invariant lossless polarization leakage inherent to even best commercial linear polarizers. Conversely, for a purely dielectric surface such a glass (i.e. BK7) reflecting from the air-side, for which r_p and r_s are both real, no full polarization leakage cancellation was possible.

3.2 Material and angular dependency

To get a better feel for the relevant parameters at work in canceling almost perfectly the polarization leakage we use the form $r_p = \rho_p \; exp(i\varphi_p)$ and $r_s = \rho_s \; exp(i\varphi_s)$. Consider high reflectivity mirrors for which $\rho_p \approx \rho_s \approx 1$. Solving equation 3.6 for field cancellation leads to the first order in $\mid b \mid \ll 1$ to a set of two equations $\cos(\alpha + \beta) = b/\tan\Delta$ and $\cos(\alpha - \beta) = b \; \tan\Delta$ where $\Delta = (\varphi_p - \varphi_s)/2$. This way both α and β can be analytically calculated (Appendix A.4). In the particular case of dielectrics reflecting from the air side for which $\Delta = \pi/2$ we see already that there are no solutions. Instead we need the condition $\Delta \neq \pi/2$ which is always verified in condition of total internal reflection. For pure silver at $\lambda = 905 \; nm$, $\varphi_p - \varphi_s = 192.52°$ implying $\tan\Delta = -9.12$ which in turn shows that for this particular case a solution $I = 0$ exist for polarizers with leakage levels $b^2 < 0.012$. One more step is required to make use of these equations towards interpreting our results because we did not find any easy way to measure independently an absolute value α and β to the precision required for our measurements. As explained in the previous section the value we can measure experimentally with the required accuracy is the shift $\alpha - \alpha_0$. In the reference measurement with the analyzer placed directly after the polarizer we assume that the cross-polarization condition $\alpha_0 - \beta = \pi/2$ holds. For the test experiment, the equation $\cos(\alpha - \beta) = b \; \tan\Delta$ is developed in the limit of

Material	ϕ_p	ϕ_s	$\mid r_p \mid^2$	$\mid r_s \mid^2$	Δ
Silver (Ag)	25.036°	-167.482°	0.995	0.997	96.259°
Aluminium (Al)	18.404°	-170.798°	0.854	0.924	94.601°
Gold (Au)	29.026°	-165.487°	0.959	0.979	96.941°
Air to glass	0.000°	-180.000°	0.008	0.094	90.000°
Glass to air	76.893°	+38.446°	1.000	1.000	19.223°

Table 3.1: Optical properties of common reflecting surfaces at an angle of incidence $\theta_i = 45°$ and wavelength $\lambda = 905\ nm$. *Values are taken from* [28]

small leakage $\mid b\ \tan\Delta \mid \ll 1$, so that we get $\alpha - \beta = \pi/2 \mp b\ \tan\Delta$ for the near p and s conditions respectively. This shows that the correction to the analyzer is simply $\alpha - \alpha_0 = \mp b\ \tan\Delta$ corresponding to $\alpha - \alpha_0 = +0.898°$ with a measured leakage $1/b^2 = 8.3 \times 10^4$ and $-0.977°$ with $1/b^2 = 9.6 \times 10^4$ for the p- and s-state respectively in the case of the measurement of Fig. 2.3b, for a protected silver mirror. Hence, we determine $\Delta = 102.48°$ and $\Delta = 100.7°$ for p and s beam respectively. Given the measured leakage limiting the nominal extinction at $1/b^2 = (1.5 \pm 0.5)10^5$ we determine $b = (2.7 \pm 0.5)10^{-3}$ which in turn allows determining $\Delta = 99.7° \pm 1.7°$ a value to be compared to the value for pure silver of $\Delta = 96.27°$ (see table 3.1). The difference could be possibly related to the effect of the protective layer or on the purity of the silver mirror we used.

From another point of view, we can get an exact value of Δ with a reflectivity measurements of a $\pi/4$ linearly polarized incident beam in a cross-polarization configuration (Fig. 2.3c, $\pm 45°$). The normalized intensity just after the analyzer is given by equation (3.6) for $\beta = \pm\pi/4$ and $\alpha = \pm\pi/4$. This is expressed as:$I_{\pm\pi/4} = |r_p + r_s|^2/4$. Recalling Fresnel reflectivity coefficients $r_p = \rho_p\ exp(i\varphi_p)$ and $r_s = \rho_s\ exp(i\varphi_s)$ with $\rho_p \approx \rho_s \approx 1$, we get $|r_p + r_s|^2 = 4\cos^2\Delta$ where $\Delta = (\varphi_p - \varphi_s)/2$. After simplifying, we get $I_{\pm\pi/4} = \cos^2\Delta$. The corresponding cross-polarization extinction is $1/I_{\pm\pi/4} = 4/|r_p + r_s|^2$, which is also $1/(\cos^2\Delta)$. This simple novel method shows that we can conveniently measure the phase shift $\varphi_p - \varphi_s$ between p- and s-polarization after reflection for metals. The measurements (Fig. 2.3c, $\pm 45°$) performed using a high reflectivity silver mirror for $\beta = \pm\pi/4$ show an extinction ratio 44.4 ± 2.4 leading to a phase shift $\varphi_p - \varphi_s = 98.63° \pm 0.23°$ between the p- and s-reflected components. The results of this approach based on reflectivity measurements at $\pm\pi/4$ polarization are more promising comparing to the angular shift measurements as discussed in chapter 5.

The full measurements shown in Fig. 2.3c are fitted using equation (3.6) accounting convincingly for the cross-polarization extinction amplification and the slight polarizer and analyzer rotation shift required to reach it. In the limit $\rho_s \approx \rho_p$, we calculate that the polarization leakage should be sufficiently small to allow perfect extinction when the condition $b^2 < (1 - \sqrt{\tan^2\Delta - 1}/\sqrt{\tan^2\Delta + 1})/2$ is verified (Appendix A.5). For our experimental case, this corresponds to

$b^2 < 1.26\ 10^{-2}$ and for a pure silver to $b^2 < 6.00\ 10^{-3}$. Such values are in fact relatively large and thus allow realistically achieving polarization leakage cancellation for most standard commercial polarizers.

3.3 Wavelength dependency

A last practical aspect to address is the wavelength dependency of this effect. For a highly reflecting mirror, the wavelength dependency is to be found in the phase difference $\Delta(\lambda)$. As a result, the correction to the analyzer angle $\alpha(\lambda) - \alpha_0 = \mp b \tan\Delta(\lambda)$ calculated for reaching maximum extinction is also a function of wavelength. Hence, we see that the polarizer angle α of maximum extinction shifts as a function of wavelength as $\partial\alpha/\partial\lambda = \mp b(\partial\Delta/\partial\lambda)/\cos^2\Delta$ which can easily be evaluated using the formula of Fresnel coefficient and the corresponding dielectric constant of the mirror relevant material. For a perfect silver mirror and a polarization leakage of 10^5 we evaluate a chromaticity rate of $\partial\alpha/\partial\lambda = 0.0019°/nm$ for a wavelength around $\lambda = 905\ nm$. In this particular example, keeping the analyzer angle at value of maximum extinction for 905 nm, the wavelength could be shift by up to $\pm 10\ nm$ and still keep the extinction up to a level $> 10^7$.

3.4 Conclusion

At this point we could conclude our work here as we were able to explain convincingly all the features of the enhanced polarization extinction. Our analysis has however occulted so far a crucial point, namely the experimental fact that the leakage cancellation was only measurable in a confocal arrangement, a point that is elucidated in the next chapters. More specifically, the analysis we conducted leading to the main result in equation (3.6) so far was done purely for a plane wave for which the Jones matrix formalism is valid. In reality however, the finite size of the collimated Gaussian laser beam imposes a finite angular wave distribution around the angle of incidence on the mirror [29]. The Fresnel coefficient r_p and r_s becomes then a function of the angular distribution [29]. This as we will see, leads to significant geometrical depolarization effects in form of new optical modes limiting the total extinction to the 10^4 range. We will see that a confocal arrangement filters away the depolarization modes and that the result of this chapter turns out to be fortuitously usable.

Chapter 4

Modal transformation of a reflected polarized Gaussian beam

Adapted from [1]:
Meryem Benelajla, Elena Kammann, Bernhard Urbaszek, and Khaled Karrai, **"The physical origins of extreme cross-polarization extinction in confocal microscopy"**, arXiv:2004.13564 (2020).

4.1 Experimental modal analysis of beam reflectivity

4.1.1 Experimental details

To find the origin of the unexpectedly high polarization rejection ratio $> 10^8$, we performed an x, y scanning imaging of the detected intensity in cross-polarization conditions. Imaging can be achieved by scanning a mirror (9) or scanning the spatial position of the collecting fiber in the focal plane of the focusing objective (Fig. 2.3b). Scanning the fiber position with respect to the fix objective has the advantage that the optical system is fixed in space and avoids the problem of misalignment but mirror scanning can be faster and offer wider range of scan. In this work, we use the fiber scanning technique. The output fiber is mounted on a piezo electric scanner (Thorlabs scanner, PE4 piezo electric actuator) which has a maximum travel range of $15\mu m$ when $150\ V$ is applied to the piezo actuator x or y (Fig. 4.1). We use the attocube ASC500 scan and imaging controller with xy-scan generator to create the voltage necessary for the scan. Such controller has a maximum allowed voltage output $\pm 15V$ and for this reason, we use the attocube scan voltage amplifier ANC200 to amplify the maximum allowed voltage by a factor 10 in order to reach the $150V$ at the piezo scanner. In this configuration, the x, y output scanners of the ASC500 are connected into the x, y DC in of the ANC200. Then, the x, y output of the ANC200 are connected to the x, y piezo scanner. The photo-detector measured power intensity $I_{x,y}$ corresponding to each pixel location x, y on the scan is collected via a single mode fibre in

combination with the femto variable gain photo-receiver (see specifications in section 2.2.3). The electrical output signal is then connected to the signal input of the ASC500 controller. The recorded signal is imaged into a two dimensional color plot using the ASC500 software.

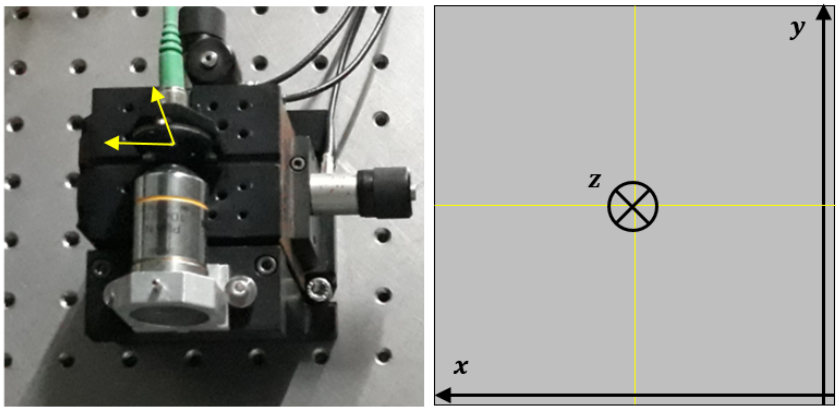

Figure 4.1: (Left) xyz-piezo electric scanner when no voltage is applied to the actuators. (Right) Plane at objective focus, looking into the objective back aperture towards the optical fiber entrance. x (y respectively) increasing in the direction of the axis x (y respectively) on the drawing for voltages increasing from 0 to up. Manual Resolution:1μm. Piezo travel range: 15μm. Piezo driving voltage 150V. Piezo capacitance: 1.4μF.

4.1.2 Confocal imaging of Imbert-Fedorov modes

In the absence of a reflecting surface between the analyzer and polarizer in cross-polarization, namely the reference configuration in Fig. 2.3a, the measurements in Fig. 4.2a,b (upper row) show a pure TEM_{00} Gaussian mode field attenuated by 8.3×10^4 and 9.6×10^4 for p- and s- polarized beam, respectively. This level is expected for the polarizer leakage specifications. In contrast, when we place the analyzer after the reflecting test surface, the measurements show that the mode splits into two lobes distributed along $\vec{e}_y$ and located above and below the reflectivity plane. In this cross-polarized configuration, we find an intensity "hole" at the location of the optical fiber center. There the intensity extinction is slightly higher than 10^8, a factor 100 away from our actual setup sensing-limit discussed later in this work.

To get a feel for the measured modal transformation for p- and s-, we measured and showed in Fig. 4.3 and Fig. 4.4 the evolution of the confocal light intensity maps for different analyzer rotation angles variation $\delta\alpha$ around the symmetrically split mode. Fig. 4.3d and 4.4d show quantitatively for p- and s-polarizations the measured positions of beam-peak shifts along $\vec{e}_y$ and splitting above and below the plane of incidence as a function of $\delta\alpha$. We observed a very similar behavior for beam-splitter cubes typically used in the resonant fluorescence setup such as in reference [8, 9, 16, 18], with the difference however that equivalent figure looks instead mirrored with respect to the axis $\Delta y = 0$.

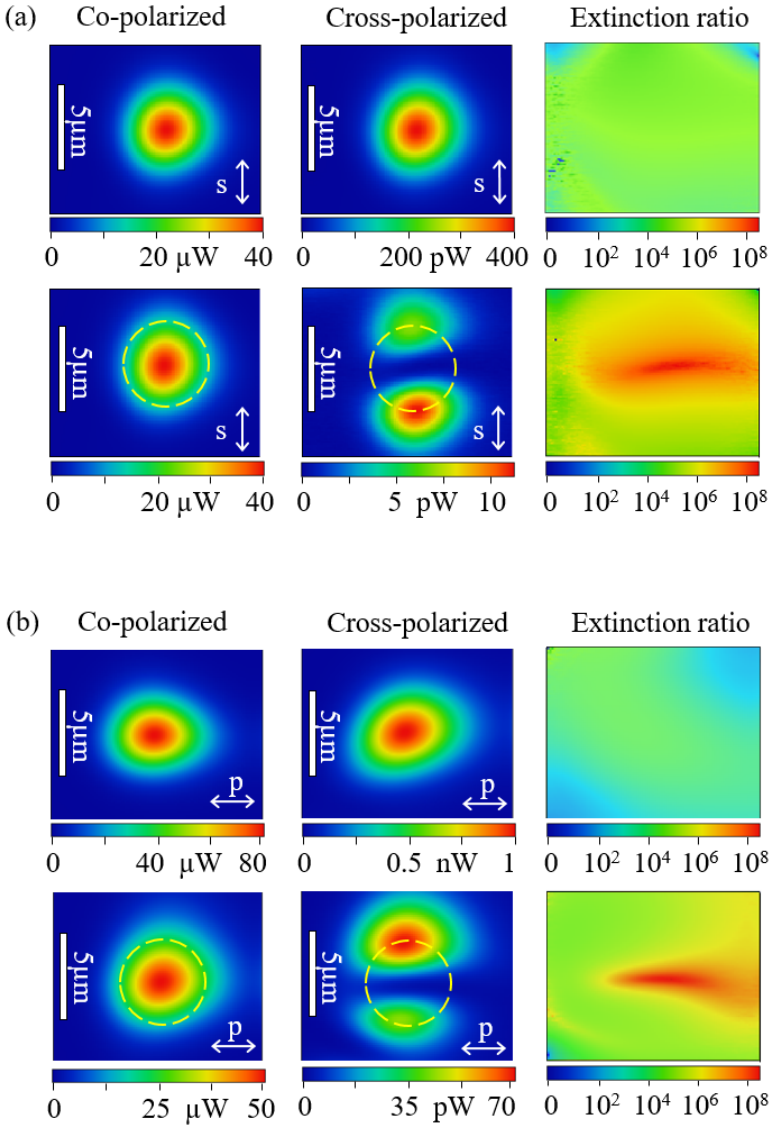

Figure 4.2: Confocal mapping of *s*- (a) and *p*- (b) laser beam in co- and cross-polarization using a scanning mirror (9). The upper and lower rows of the figures are measurements with the analyzer placed before (Fig. 2.3a) and after (Fig. 2.3b) the test reflecting surface respectively, in *s*-polarization and *p*-polarization (panel a and b). We plot the extinction ratio map by dividing, pixel per pixel, the co- with the cross-polarized data. In cross-polarization, a modal splitting along $\vec{e_y}$ above and below the plane of incidence is observed both for the *s*- and *p*-polarization. The dotted line circle is the $1/e$ intensity level of the Gaussian distribution resulting from the confocal convolution between the focused spot and the collecting fiber mode. The location of the maxima of the modal splitting lie exactly on that circle. The diameter of this circle gives also the non-convoluted focal spot waist diameter at $1/e^2$ focused on the collecting fiber end. The vertical white bar represents 5μm.

In all cases, such split-lobes intensity distribution is very reminiscent of a TEM_{01} Hermite-Gaussian mode.
Figure 4.3c and 4.4c show on careful inspection that the minima of intensity or maxima of extinction do not occur exactly at $y = 0$ but instead are very slightly displaced symmetrically along y for both the *p*- and *s*-polarization. This mean that there is not a single position of the fibre location y that can lead to a maximum extinction for both *p*- and *s*-polarization at the same time. This is also clearly seen in Fig. 2.3c for which the extinction is beyond the 10^9 range for the *s*-polarization and 10^8 for *p*- in that particular measurement. This observation suggest clearly that the novel modes along y do seem to assist in boosting the extinction well beyond the 10^8 level. We have reached a record level of 10^{10} for which the limiting factor was the dark noise of our detector. The challenge in such experiment is to have a polarization rotator that enable stepping with small enough rotation angles. At this point we need to find out why (i) the confocal arrangement enables the dramatic extinction enhancement as seen in Fig. 2.3c, and (ii) why does the beam shift and split at cross-polarization in Fig. 4.2 (lower row) and this always above and below the plane of incidence. To answer these questions we need to first model the spatial field distribution at the focal plane of the focusing lens just before the collecting single mode optical fiber (see section 4.2.1) and then use the collecting fiber as the confocal Gaussian filter function porting the light to the detector (see section 4.2.2).

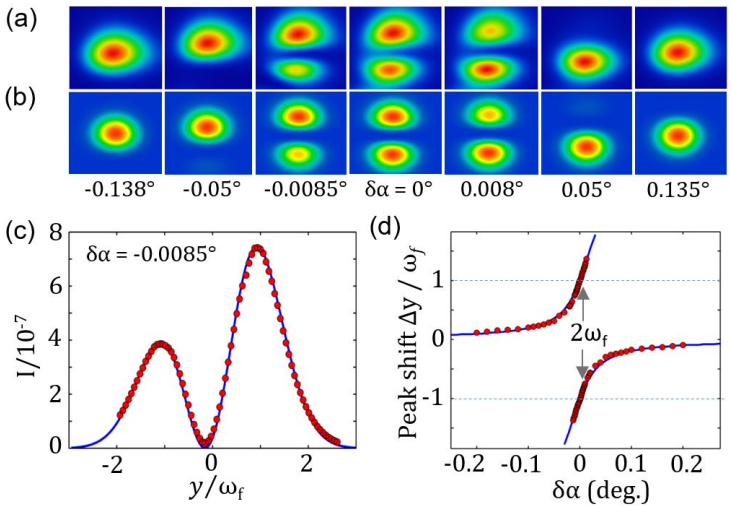

Figure 4.3: *p*-polarized beam reflected off a silver mirror. Measured (a) and simulated (b) evolution of the modal confocal imaging mapping through maximum extinction (c) for different analyzer angles $\delta\alpha$ as explained in text. In (d), the beam peak-shift and splitting positions are shown in units of beam waist ω_f at focus which we modeled for our silver mirror $\Delta = 102.48°$and a leakage of $1/b^2 = 8.3 \times 10^4$

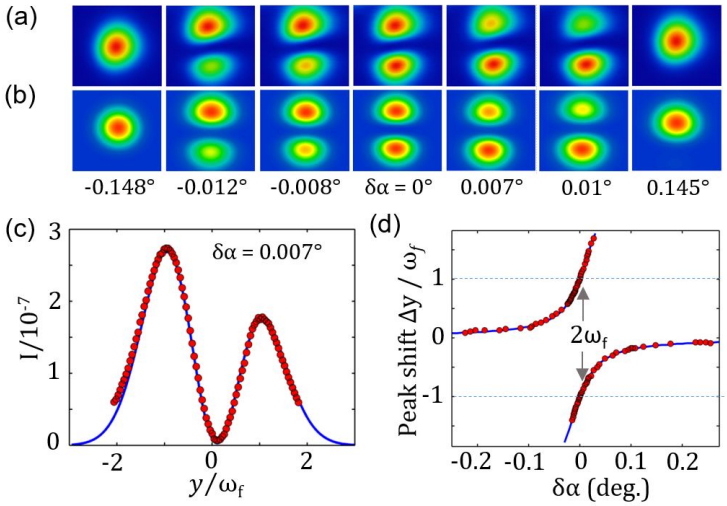

Figure 4.4: s-polarized beam reflected off a silver mirror. Measured (a) and simulated (b) evolution of the modal confocal imaging mapping through maximum extinction (c) for different analyzer angles $\delta\alpha$ as explained in text. In (d), the beam peak-shift and splitting positions are shown in units of beam waist ω_f at focus which we modeled for a silver mirror $\Delta = 100.7°$and a leakage of $1/b^2 = 9.6\times10^4$

4.2 Theoretical modal analysis of beam reflectivity

4.2.1 Mirror transfer matrix in angular domain

In this section, we will model the spatial field distribution $\vec{\mathcal{E}}_{f\,x,y}$ at the focal plane of the focusing lens just before the collecting single mode optical fiber. The finite size beam before the mirror results from a Gaussian-weighted superposition of plane waves propagating along an angular distribution $\vec{k}/k_0 = u\vec{p} + v\vec{s} + w\vec{k_0}/k_0$ very narrowly centered around $\vec{k}_0$ the wave vector along the optical axis with $k_0 = 2\pi/\lambda$ as depicted in figure 4.5. In the paraxial approximation u and v are both $\ll 1$, so they represent the angular spread of the collimated beam. The focusing lens transforms each plane wave field $\vec{E}_{u,v}$ of the angular distribution into a field density $\vec{\mathcal{E}}_{f\,x,y}$ in the focal plane, hence the beam reaching the focal plane at distance f result from a coherent superposition of all such focused components (Appendix B.2). Assuming that all these waves are paraxial and applying the Fresnel approximation [30] one can establish that

$$\vec{\mathcal{E}}_{f\,x,y} = \frac{-i}{\lambda f}\exp\Big(+ik_0 f\Big)\iint_{-\infty}^{+\infty}\vec{E}_{u,v}\;exp\Big[+ik_0(xu+yv)\Big]\,du\,dv \tag{4.1}$$

The integrals run normally within the maximum boundaries -1 and 1 for u, v, but for mathematical convenience they are extended to infinities as this does not affect the result in a paraxial approximation, namely because $\vec{E}_{u,v}$ vanishes rapidly when u, v are no longer much less than unity. In what follows

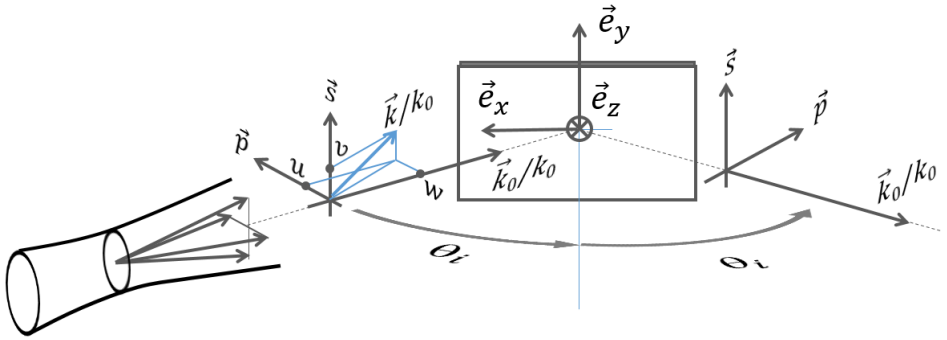

Figure 4.5: Geometry of beam reflection off a mirror. The incident beam has a Gaussian field distribution in the transverse plane. The transverse u, v and longitudinal w wavenumbers depend on the angle of incidence as explained in text.

we will drop the propagation phase term $\exp{+ik_0 f}$ as we from now on just concern with establishing the field at focal plane only. The next step is to obtain the angular distribution $\vec{E}_{u,v}$. Such problem was modeled for a Gaussian field distribution in [31] by Aiello and Woerdman. We derive here a simplified version conveniently describing the essential physics needed to model our observations. We begin with the field just before the polarizer for which we assume a linearly polarized Gaussian-field normalized angular distribution $\vec{E}_{0uv}$

$$\vec{E}_{0uv} = \frac{E_0}{\pi\theta_0^2}\, exp\Big(-\frac{u^2+v^2}{\theta_0^2}\Big)\begin{bmatrix}\cos\beta\\ \sin\beta\end{bmatrix} \tag{4.2}$$

The mode divergence $\theta_0 = 2/(k_0\omega_0) = \omega_0/l$ results from the finite size of the collimated laser beam with beam radius $\omega_0 \equiv 3mm$, and the Rayleigh range $l = k_0\omega_0^2/2$ is 10^4 m, a value much larger than the size of our experimental setup allowing us to ignore the role of beam propagation up to the focusing lens. With this convention a $p(s)$ polarized light is obtained at $\beta = 0(\pi/2)$.
When the beam reflects off the test surface, each plane wave component acquires an angle dependent Fresnel reflection coefficient $r_{p,uv}$ and $r_{s,uv}$ that are function not only of θ_i but also of u, v [29]. Consequently, for each plane wave component, we choose a coordinate system $\vec{e}_p$, $\vec{e}_s$, $\vec{k}/k_0$ that defines a local incidence plane for that wave. The longitudinal basis vector is $\vec{k}/k_0$ and the transverse ones are $\vec{e}_s = \vec{k}/k_0 \times \vec{e}_z$ and $\vec{e}_p = (\vec{k}/k_0 \times \vec{e}_z) \times (\vec{k}/k_0)$ in the s- and p- planes respectively. To obtain the reflectivity of the mirror for each plane wave, we determine first the weights of p- and s- field components, given by the weighted projections $r_{p,uv}(\vec{e}_p \cdot \vec{E}_{0uv})$ and $r_{s,uv}(\vec{e}_s \cdot \vec{E}_{0uv})$. We determine then the resulting reflected field transverse field along the corresponding reflected basis $\vec{e}_{s,R} = \vec{k}_R/k_0 \times \vec{e}_z$ and $\vec{e}_{p,R} = (\vec{k}_R/k_0 \times \vec{e}_z) \times (\vec{k}_R/k_0)$ such $\vec{E}_{uv} = r_{p,uv}(\vec{e}_p \cdot \vec{E}_{0uv})\vec{e}_{p,R} + r_{s,uv}(\vec{e}_s \cdot \vec{E}_{0uv})\vec{e}_{s,R}$. Here $\vec{k}_R$ is the mirrored wave vector after reflection. In the paraxial limit, for a beam impinging, the Fresnel coefficients are developed to the first order in u around θ_i and v around 0, giving $r_{p,uv} = r_p + u\ \partial r_p/\partial\theta_i$ and $r_{s,uv} = r_s + u\ \partial r_s/\partial\theta_i$. The

first order derivatives $\partial r_{p/s\ uv}/\partial v$ in the s-plane vanish both for r_p and r_s leaving just derivative $r_p^{'} = \partial r_p/\partial\theta_i$ and $r_s^{'} = \partial r_s/\partial\theta_i$. We calculate the components of the incoming and reflected basis vectors $\vec{e}_p$, $\vec{e}_s$, $\vec{k}/k_0$ and $\vec{e}_{p,R}$, $\vec{e}_{s,R}$, $\vec{k}_R/k_0$ in the paraxial limit $u, v << \theta_i$. After a lenghty but straightforward calculation we obtain the reflected field distribution after the mirror for each angle u, v (see Appendix B.1) . We express the result conveniently in terms of Matrix notation $\vec{E}_{uv} = \bar{\bar{M}}_{u,v}\ \vec{E}_{0uv}$ where

$$\bar{\bar{M}}_{u,v} = \begin{bmatrix} r_p & 0 \\ 0 & r_s \end{bmatrix} + u \begin{bmatrix} r_p' & 0 \\ 0 & r_s' \end{bmatrix} + v \frac{r_p + r_s}{\tan\theta_i} \begin{bmatrix} 0 & -1 \\ 1 & 0 \end{bmatrix} \tag{4.3}$$

Upon inspection of the expression 4.3 for symmetries we see now that the reflectivity Jones matrix transforms an impinging perfect Gaussian mode, such as equation (4.2), into the sum of TEM_{00}, TEM_{01} and TEM_{10} Hermite-Gauss modes. The indices for TEM_{nm} indicate the number of nodes along the $\vec{p}$ and $\vec{s}$ direction repectively. The first term in the right hand side is the normal test surface reflectivity we used in the first part of this paper. The second term is responsible for generating a TEM_{10} mode along $\vec{p}$ in the plane of incidence. This term is in fact responsible for the Goos-Hänchen effect [32–37], as it has its physical origin in the angular dispersion of the reflectivity terms at θ_i. Here the different plane wave components acquire slightly different phases upon reflectivity shifting the beam in the plane of incidence. Because this matrix is diagonal, we see that for a perfect p- or s-polarization the Goos-Hänchen effect does not contribute to depolarization. The third term, the most relevant to this work, is responsible for generating an out of plane of incidence TEM_{01} mode with two lobes along $\vec{e}_y$. This term is the physics responsible for the Imbert-Fedorov effect [19, 20, 22, 33–38] known to deviate a reflected light beam above or below the plane of incidence depending on its right handed or left handed polarization helicity. The calculation detailed above shows that this term originates purely from geometrical projections in which the gradual phase-shift gained by each plane wave component upon reflection, sums to a cross-diagonal matrix that mixes the p- and s- phase shifted reflected plane wave components. Consequently this term is responsible for an intrinsic reflectivity induced depolarization for p- and s-polarization even when using ideally perfect polarizers. Because of the purely geometrical projections nature of the argumentation, compelling connections between the Imbert-Fedorov effect, Berry's phase and spin-Hall effect of light are discussed in the literature [22, 38]. Because of the direct proportional dependency of this matrix on the angle v and in particular its sign, it creates a TEM_{10} mode asymmetric along $\vec{e}_y$, adding/suppressing field to/from the symmetric main mode displacing this way its weight above or below the plane of incidence depending on its helicity. This can be easily verified using a circular polarization version of equation (4.2) with the Jones matrix equation (4.3). From this simple derivation, it is worth appreciating that in the paraxial approximation equation (4.3) express both Goos-Hänchen and Imbert-Fedorov effects in an elegant and compact way. At this point, we can see from a symmetry argument that our confocal arrangement enhances cross-polarization extinction. Without the confocal arrangement, the extinction would have been naturally limited in the 10^4 range

in our experiment as we will discuss in the section 4.2.3.

4.2.2 Mirror transfer matrix in space domain

In the following step we express the field distribution transmitted through the polarizer, the mirror and analyzer at the back aperture of the focusing lens $\vec{E}_{uv} = \bar{\bar{A}}(\alpha)\bar{\bar{M}}_{u,v}\bar{\bar{P}}(\beta)\vec{E}_{0uv}$ used in the Fourier transform equation (4.1). Before providing the general solution, we get first a feel for the physical parameters governing the Imbert-Fedorov cross-polarized mode. For this, we consider the special case of a p- or s-polarized light impinging on the mirror and subsequently analyzed in cross-polarization configuration. Here, only the third matrix on the r.h.s of equation (4.3) is relevant, all other terms cancel. After some algebra (Appendix B.2) we obtain the cross-polarized field for the $p(s)$ incident light

$$\vec{\mathcal{E}}_{f\perp} = \frac{\pm E_0}{\pi\omega_f^2}\frac{r_p + r_s}{\tan\theta_i}\frac{y}{l_f}\, exp\Big(-\frac{x^2+y^2}{\omega_f^2}\Big)\,\vec{e}_s \tag{4.4}$$

here the focused spot waist radius $\omega_f = \lambda f/\pi\omega_0 \simeq 2.5\mu m$ is the fiber Gaussian mode size and $l_f = k_0\omega_f^2/2$ corresponding Rayleigh range, in our case $21.7\mu m$. We notice that the field is an antisymmetric function of y with two lobes with opposite phase located at $y = \pm\omega_f/\sqrt{2}$ above and below the plane of incidence. The field peak intensity normalized to the maximum of co-polarized peak intensity is proportional to the ratio ω_f/l_f which is nothing else than $\theta_f = 2/(k_0\omega_f)$ the half cone angle of the focused beam which in our experiment is the numerical aperture of the single mode fiber. An important result emerges, namely that the lens amplifies dramatically the Imbert-Fedorov mode field strength. It is easy to show that the amplification factor of the light intensity is ω_0^2/ω_f^2 when comparing the peak strength just after the reflecting test surface (i.e $\omega_0 = 3mm$) and at the focal plane. In our case we obtain an amplification of $3mm/2.5\mu m = 1200$. This is the reason for which we can detect this mode so clearly in a confocal configuration.

The other essential physical parameter that governs the Imbert-Fedorov mode field intensity is the sum $r_p + r_s$ given by the material reflecting properties. To get a more physical insight we use the representation $r_p = \rho_p\, exp(i\varphi_p)$ and $r_s = \rho_s\, exp(i\varphi_s)$ that can be conveniently symmetrized using $\rho_s = \rho + \delta\rho/2$, $\rho_p = \rho - \delta\rho/2$ for the reflectivity and $\Delta = (\varphi_p - \varphi_s)/2$ the phase difference. This way we obtain

$$r_p + r_s = 2\rho\cos\Delta + i\delta\rho\sin\Delta \tag{4.5}$$

to within a constant proportional phase term $expi(\varphi_p + \varphi_s)/2$ identical for all modes of equation (4.3). We now see that the difference $\varphi_p - \varphi_s$ governs the intensity and the phase of the Imbert-Fedorov mode. For instance in the case of the air side reflectivity off a perfect dielectric we have $\varphi_p - \varphi_s = \pi$, hence $r_p + r_s = i\delta\rho$, so the Imbert-Fedorov mode field intensity is directly proportional

to the pure differential reflectivity between the p and s waves. In contrast, for dielectrics under total internal reflectivity and for metals we have $\delta\rho \approx 0$ and $\rho \approx 1$ so that $r_p + r_s = 2\cos\Delta$. In this case the strength of the depolarizing mode is fully governed by the phase difference $\varphi_p - \varphi_s$. We conclude that mapping the Imbert-Fedorov mode fields in a confocal microcopy setup provides a direct and sensitive access to the differential reflectivity amplitude and phases of a reflecting surface. To move forward with our analysis on the more general case we have performed the Fourier optics transformation equation (4.3). The calculation, shown in detail in Appendix B.3. The result is that the field image at focal plane for the test experiment with the mirror placed between the polarizers is $\vec{\mathcal{E}}_{fxy} = \bar{\bar{A}}(\alpha)\bar{\bar{M}}_{x,y}\bar{\bar{P}}(\beta)\vec{\mathcal{E}}_{0x,y}$ where the effective reflectivity Jones matrix is given by

$$\bar{\bar{M}}_{x,y} = \begin{bmatrix} r_p & 0 \\ 0 & r_s \end{bmatrix} + i\frac{x}{l_f}\begin{bmatrix} r'_p & 0 \\ 0 & r'_s \end{bmatrix} + i\frac{y}{l_f}\frac{r_p + r_s}{\tan\theta_i}\begin{bmatrix} 0 & -1 \\ 1 & 0 \end{bmatrix} \tag{4.6}$$

The spatial distribution of the field $\vec{\mathcal{E}}_{0x,y}$ results from the lens transforming the unperturbed linearly polarized laser field angular distribution of equation (4.2) into a spatial normalized distribution now at the focal point such

$$\vec{\mathcal{E}}_{0x,y} = \frac{-iE_0}{\pi\omega_f^2}\, exp\Big(-\frac{x^2+y^2}{\omega_f^2}\Big)\begin{bmatrix}\cos\beta \\ \sin\beta\end{bmatrix} \tag{4.7}$$

This result turns out to be within a Gouy phase $-i$ at focus, the one discovered in a different context in the insightful and pioneering work of Aiello *et al.* [39]. In their work the authors provided within a paraxial approximation, a complete analytical solution for the field distribution of a single mode Gaussian beam reflected off a mirror. The essential finding from our work is that the confocal arrangement transforms the collimated beam waist ω_0 and Rayleigh length l and of Aiello *et al.* [39] field distribution at the mirror plane, into l_f and ω_f in our case. This result appears benign at first but as discussed earlier amounts to a sizeable amplification of the weak mode intensity in proportion to ω_0^2/ω_f^2. Aiello *et al.* [39] showed that it is the finite size of the beam at the reflecting surface that are responsible for the additional field terms that affect the initial Gaussian mode. From our work it is becoming now clear here that using a confocal arrangement, the size of the beam at the mirror is not relevant to our measurements but rather the size of the focused beam that plays a crucial role. This fact, at first non-intuitive, provides a valuable advantage to explore experimentally the cross-polarization geometry with sufficient sensitivity and a very fine spatial resolution. In particular, high extinction cross-polarization extinction is kin to the "weak measurement procedure" of Aharonov *et al.* [40, 41] which we extend here to a confocal arrangement enabling the added benefit of spatial resolution. Recent literature [22] provides an interpretation for the depolarization as resulting from an effective spin-orbit interaction of light occurring at the mirror surface manifesting itself in the form of a spin-Hall effect of light [42]. In the work, we restrict ourselves to a purely modal interpretation and leave the discussion concerning spin-orbit aside.

4.2.3 Effect of confocal filtering

The one final point we need to address to get a full quantitative interpretation of our experiment is to address the effect of the confocal filter function of the collecting fibre. The single mode fiber collects and ports the field to the photo-detector, it does this however by acting as a Gaussian spatial filter. For our symmetric setup shown in Fig. 2.3 we illuminate and collect light with a single mode fibers of identical mode size, and with identical collimating and focusing lenses. The spatial filtering is a convolution between the field spatial distribution at focal plane and the fiber Gaussian mode amounting to a detected field strength $\vec{E}_D$ location x_0, y_0 with respect to the optical axis. The results of the calculation for the field are the following (Appendix C.1). First we get the mapping of the reference field without use of polarizer and reflecting surface as seen by the detector

$$\vec{E}_{D0,0} = -\frac{iE_0}{2}\, exp\left(-\frac{x_0^2+y_0^2}{2\omega_f^2}\right)\begin{bmatrix}\cos\beta\\ \sin\beta\end{bmatrix} \tag{4.8}$$

We note that beam waist at focus appears now to be broadened by a factor $\sqrt{2}$ when comparing with the distribution of equation (4.7). Second we found that the confocal filtering by convolution with a Gaussian mode leads to a modified effective Jones matrix for the reflecting surface acting on the field as seen from the detector (see Appendix C.2)

$$\bar{\bar{M}}_{Dx_0,y_0} = \begin{bmatrix} r_p & 0\\ 0 & r_s\end{bmatrix} + i\frac{x_0}{2l_f}\begin{bmatrix} r'_p & 0\\ 0 & r'_s\end{bmatrix} + i\frac{y_0}{2l_f}\frac{r_p+r_s}{\tan\theta_i}\begin{bmatrix} 0 & -1\\ 1 & 0\end{bmatrix} \tag{4.9}$$

With the confocal filtering, the Goos-Hänchen and the Imbert-Fedorov fields terms (i.e. the second and third terms of the r.h.s in the equation) are halved when compared to equation (4.6). The Jones matrix related to the polarizers and polarization leakage remain unchanged. With this last correction, we have now all the equations required in order to simulate the modal transformation induced by a reflecting surface acting on a polarized Gaussian beam and this for any arbitrary polarization and polarization leakage level. Finally the full scanning confocal mapping of the detected field is given by the analytical form

$$\vec{E}_D(x_0,y_0) = \bar{\bar{A}}(\alpha)\bar{\bar{M}}_{Dx_0,y_0}\bar{\bar{P}}(\beta)\vec{E}_{D0,0} \tag{4.10}$$

The first important result we are getting from equation (4.10) and the mirror matrix term in equation (4.9) is when the location of the fiber center and the focal spot axis coincide, namely for $x_0 = 0$ and $y_0 = 0$. In this case the result is the same as found in the simplified plane wave analysis of chapter 3 and the equation of polarization cancellation given in equation (3.6) holds fortuitously. This is the case because the filtering function of the confocal arrangement eliminates the higher depolarizing modes. Without the confocal filtering (see Appendix D), the normalized integrated total intensity in cross-polarization detected in wide field imaging of the focused point, or for collected with a wide core multimode fiber,

is obtained using equations (4.4) and (4.7):

$$\frac{\iint |\vec{\mathcal{E}}_{f\perp}|^2\, dxdy}{\iint |\vec{\mathcal{E}}_{0x,y}|^2\, dxdy} = \frac{1}{4}\frac{|r_p + r_s|^2}{\tan^2\theta_i}\left(\frac{\omega_f}{l_f}\right)^2 \tag{4.11}$$

For our experimental parameters and using equation (4.5), the collected depolarized field would limit the extinction to 1.56×10^3 and 2.1×10^3 for p- and s-polarized beam respectively. This demonstrates the key role of the confocal arrangement for the giant polarization extinction reached in the state of the art resonance fluorescence measurements [8, 9, 16, 18].

The second significant result is illustrated, applying equation (4.10) on a purely p- or s-polarized beam measured in cross-polarization, by mapping the focused spot position (x_0, y_0) across the single mode fiber end. The result is an intensity map displaying two lobes maxima located at the fiber location at $x_{0max} = 0$ and $y_{0max} = \pm\omega_f$ above and below the plane of incidence. This is in complete agreement with our measurements as seen in Fig. 4.2 for silver. We confirmed quantitatively these findings for Bragg mirrors and thin-film based beam-splitter cubes. As seen in figure Fig. 4.3 and Fig. 4.4, equation (4.10) maps closely the evolution of the mode transformation near cross-polarization condition for a metallic surface. In our experiment the material parameter of the high reflectivity surface that governs most of the effects we observed is the phase difference $\varphi_p - \varphi_s$. In particular for high reflectivity materials the intensity of the lobe maxima at cross-polarization are obtained from equation (4.10) at fiber location $(x_0, y_0) = (0, \pm\omega_f)$

$$|\vec{E}_D(0,\pm\omega_f)/\vec{E}_{D0,0}|^2 = \frac{1}{4e}\frac{|r_p + r_s|^2}{\tan^2\theta_i}\left(\frac{\omega_f}{l_f}\right)^2 \tag{4.12}$$

See Appendix C.3 for more details. In particular for high reflectivity materials, from equation (4.5) we have $|r_p + r_s|^2 = 4\cos^2\Delta$. For a pure silver surface $\Delta = 192.52°$, the lobe intensity should be 5.9×10^{-5}. For our independently measured values of $\Delta = 102.48°$ and $\Delta = 100.7°$, we should be finding 2.35×10^{-4} and 1.74×10^{-4} for p- and s- polarization respectively. We measure typical lobe maxima in the range of 0.3 to 1.4×10^{-6}. For a reason not yet elucidated, our maximum measured intensities are weaker than modeled. We believe that we are still missing a full quantitative understanding in the way the receiving fiber filters non Gaussian modes. Indeed the sensitivity of our setup should have permitted to detect the higher terms modes TEM_{11} that have a symmetry xy. Such modes originate from the finite sized waist of the Gaussian beam making it naturally divergent [43]. In fact, we can use the exact formalism developed above to show that such terms originate also from geometrical projections around the optical axis. This time the projection is not involving any reflecting surface but just the natural divergence of the beam before the lens, leading to a gradual phase-shift gained by each plane wave component here again depolarizing naturally the beam. Applying the Fourier transform due to the focusing lens and keeping in

mind the convolution imposed by the collecting fiber, we calculated that the expected clover shaped mode is peaking at the four location $(x_0; y_0) = (\pm\omega_f; \pm\omega_f)$ with an intensity given by (see Appendix E):

$$|\vec{E}_D(\pm\omega_f, \pm\omega_f)/\vec{E}_{D0,0}|^2 = \frac{1}{4e^2}\left(\frac{\omega_f}{2\, l_f}\right)^4 \tag{4.13}$$

A result corroborated in ref [43]. Using this expression for our experiment parameters, the mode peak intensity should be 3.8×10^{-7} a value that is well within our sensitivity range. It is a puzzling fact that we did not observe any trace of this TEM_{11} signal. There is no doubt however that this mode is present as measured in [43] , this is why we believe that our understanding of the way the optical fiber is filtering the signal is not complete yet.

4.2.4 Understanding effect of metal mirrors reflectivity

To get a first impression of what a metallic mirror does to a Gaussian beam, it is instructive to use the small angle approximation for the reflectivity matrix (equation (4.9)). The result is expressed as a function of the physical parameters related to the mirror material, the angle of incidence and the Gaussian beam Rayleigh length. The general reflectivity coefficients are given for reflecting material of complex dielectric function $\widetilde{\epsilon}$ under incidence angle θ_i by the following [27]:

$$r_p = \frac{\widetilde{\epsilon}cos\theta_i - \sqrt{\widetilde{\epsilon} - sin^2\theta_i}}{\widetilde{\epsilon}cos\theta_i + \sqrt{\widetilde{\epsilon} - sin^2\theta_i}} \tag{4.14}$$

and

$$r_s = \frac{cos\theta_i - \sqrt{\widetilde{\epsilon} - sin^2\theta_i}}{cos\theta_i + \sqrt{\widetilde{\epsilon} - sin^2\theta_i}} \tag{4.15}$$

In the following we concentrate on the case of total internal reflectivity (i.e. metallic mirrors). We approximate in what follows $\widetilde{\epsilon} \cong -\epsilon$ with ϵ is a real and positive number $\gg 1$. Using this definition (see Appendix F), we can write the Fresnel reflectivity coefficients in the limit of small angle approximation as:

$$r_p \cong 1 - \frac{2}{\epsilon} + \frac{2i}{\sqrt{\epsilon}} + i\frac{\theta_i^2}{\sqrt{\epsilon}} \tag{4.16}$$

and

$$r_s \cong -1 + \frac{2}{\epsilon} - \frac{2i}{\sqrt{\epsilon}} + i\frac{\theta_i^2}{\sqrt{\epsilon}} \tag{4.17}$$

Inserting equation (4.16) and (4.17) into equation (4.9), we find that the Jones matrix for a reflecting surface in the limit of small angle approximation is given

by:

$$\lim_{\theta_i \to 0} \bar{\bar{M}}_{Dx_0,y_0} = \left(1 - \frac{2}{\epsilon} + \frac{2i}{\sqrt{\epsilon}}\right)\begin{bmatrix}1 & 0\\ 0 & -1\end{bmatrix} + i\frac{\theta_i^2}{\sqrt{\epsilon}}\begin{bmatrix}1 & 0\\ 0 & 1\end{bmatrix} - \frac{\theta_i}{\sqrt{\epsilon}}\frac{x_0}{l_f}\begin{bmatrix}1 & 0\\ 0 & 1\end{bmatrix} - \frac{\theta_i}{\sqrt{\epsilon}}\frac{y_0}{l_f}\begin{bmatrix}0 & -1\\ 1 & 0\end{bmatrix} \tag{4.18}$$

The same formula is also conveniently expressed as a function of the beam waist radius and photon wavelength

$$\lim_{\theta_i \to 0} \bar{\bar{M}}_{Dx_0,y_0} = \left(1 - \frac{2}{\epsilon} + \frac{2i}{\sqrt{\epsilon}}\right)\begin{bmatrix}1 & 0\\ 0 & -1\end{bmatrix} + i\frac{\theta_i^2}{\sqrt{\epsilon}}\begin{bmatrix}1 & 0\\ 0 & 1\end{bmatrix} - \frac{\theta_i}{\sqrt{\epsilon}}\frac{\lambda x_0}{\omega_f^2}\begin{bmatrix}1 & 0\\ 0 & 1\end{bmatrix} - \frac{\theta_i}{\sqrt{\epsilon}}\frac{\lambda y_0}{\omega_f^2}\begin{bmatrix}0 & -1\\ 1 & 0\end{bmatrix} \tag{4.19}$$

This formulation is useful to get a feel for how the physical parameters govern the various component in the modal transformation of Gaussian beam reflected off a mirror. The first limit is to understand that in the case of an ideally perfect mirror in which case $(\widetilde{\epsilon} = -\epsilon) \to -\infty$, the mirror reflectivity is

$$\lim_{(\widetilde{\epsilon}=-\epsilon)\to-\infty} \bar{\bar{M}}_{Dx_0,y_0} = \begin{bmatrix}1 & 0\\ 0 & -1\end{bmatrix} \tag{4.20}$$

With this matrix, the reflected mode remains Gaussian and its polarization is mirrored but remain "pure". For finite values of ϵ, new terms appear that now involve the mirror material properties, the angle of incidence θ_i, the Gaussian beam waist and wavelength (or Rayleigh length l_f). The first matrix provides reflectivity at vanishing angle of incidence. It shows first that the p and s reflectivity are 180° out of phase. It is interesting to note that for a purely real and negative dielectric constant $\widetilde{\epsilon} = -\epsilon$ the matrix pre-factor contains an imaginary term. This is the case of total internal reflectivity. This term delays or advance of the reflected light for the p or s polarization with respect to the incident laser field, the relative phase between p and s is constant at 180°. The second term leads to a phase retardation that becomes increasingly different for p and s at finite non-vanishing angle θ_i, the phase difference scales as θ_i^2. This is the term that introduces ellipticity on a linearly polarized field tilted with respect to the incident plane and enables a perfect compensation of the polarization leakage in our experiment. While the first two matrices describes the reflectivity of a plane wave off a metallic mirror, the third and fourth matrix relate to the finite size of a light beam. They do vanish in the limit of infinite beam waist size, namely strictly speaking in the case of a plane wave. These two matrices transform the initial Gaussian mode into the next higher symmetry modes with a node at the location of the fiber position origin. The intensity of these modes scale like inverse Rayleigh length, which represent the depth of field of the light focused onto the confocal filter aperture. The stronger the focusing the larger the weight of the higher order modes. We learn here that in a confocal arrangement, the size of the beam at the mirror location is not directly relevant; instead, the size of focused beam at the location of the collecting aperture drives the intensity and the size of the new modes. This remark, helps determining new measurement strategies compared to previous works. In particular in earlier publications [42] [39], the Gaussian beam was focused on the reflecting surface.

This is no longer a limitation allowing to work with collimated beams over large distances and illuminating larger portions of mirror materials.

The third matrix is responsible for the Goos-Hänchen effect [32–37]. On close inspection, one can see that matrix distributes continuously along x (i.e. in proportion to x_0) the weight to the reflectance components in the plane of incidence across the Gaussian beam field changing its sign past the node at origin. This field added to the original Gaussian distribution results in a displacement of the maximum of the beam intensity in the p-plane. The effect is understood as beam displacement in the plane of incidence. The displacement is positive, namely along $+\vec{p}$ for an s- polarized Gaussian beam and is negative (along $-\vec{p}$) for a p-polarized beam. Measurements for metals were published in [44]. The physics behind this effect is the finite penetration depth of the optical beam under the surface of the mirror. The penetration depth depends on the angle of incidence. The larger the angle the shorter the penetration depth. The finite size of the beam is formed by a superposition of plane waves with a distribution of angle of incidence. This result into a non-uniform penetration depth for the distribution of wave vectors making the finite size beam. This leads to a continuous bending of the beam trajectory to resurface as a displaced beam. The physics that governs the size of the displacement is the local derivative of the reflectance with respect to the angle of incidence, namely the dispersion of the reflectance. The matrix shows that the Goos-Hänchen effect preserves the nature of the incoming polarization for pure p- or s-linearly polarized fields.

The fourth matrix is the only non-diagonal matrix. In actual fact it is anti-diagonal which mean that it transforms equally p- polarization into s and conversely s into p. Further, this matrix adds continuously weight in the field distribution along y a direction perpendicular to the plane of incidence, its sign changes when passing through the origin. As just said, the new mode created by this term is perpendicular in polarization to the incoming p- or s-polarized beam. As a result, the directly reflected original p or s field components and the new mode fields do not interfere and hence cannot shift the beam position. However when the incoming field is circularly polarized, this matrix element adds weight to the fields in such a way that it displaces the beam maximum intensity above or below the plane of incidence depending on the chirality of the polarization [19, 20, 22, 33–38].

4.3 Observation on different materials

In our experiment, we have experimentally verified the stability of the extinction ratio over tens of hours for p- and s-linearly polarized incident light. We observed qualitatively the same effects for incidence angles of θ_i at 9°, 22°, 25°, 30° and 68°. We observed qualitatively the same behavior for different type of polarizers such as crystal polarizer (Glan-Taylor) and nanoparticle thin film linear polarizers, for different mirrors such as silver, gold, aluminum, dielectrics Bragg reflectors and non-polarizing beam-splitter cubes, attesting to the robustness of

this effect. The results were qualitatively very similar for all these reflecting surfaces. We choose to show here the data measured with a Thorlabs non-polarizing beam-splitter cube (700 - 1100 nm) 30:70 (R:T) split ratio (Fig. 4.6(a)(b)) and dielectric high reflectivity Bragg mirror BB1-E03 - Ø1 (Fig. 4.6(c)(d)), this with the exception of data measured for comparison on a dielectric BK7 glass surface reflecting from air as discussed later in this section.

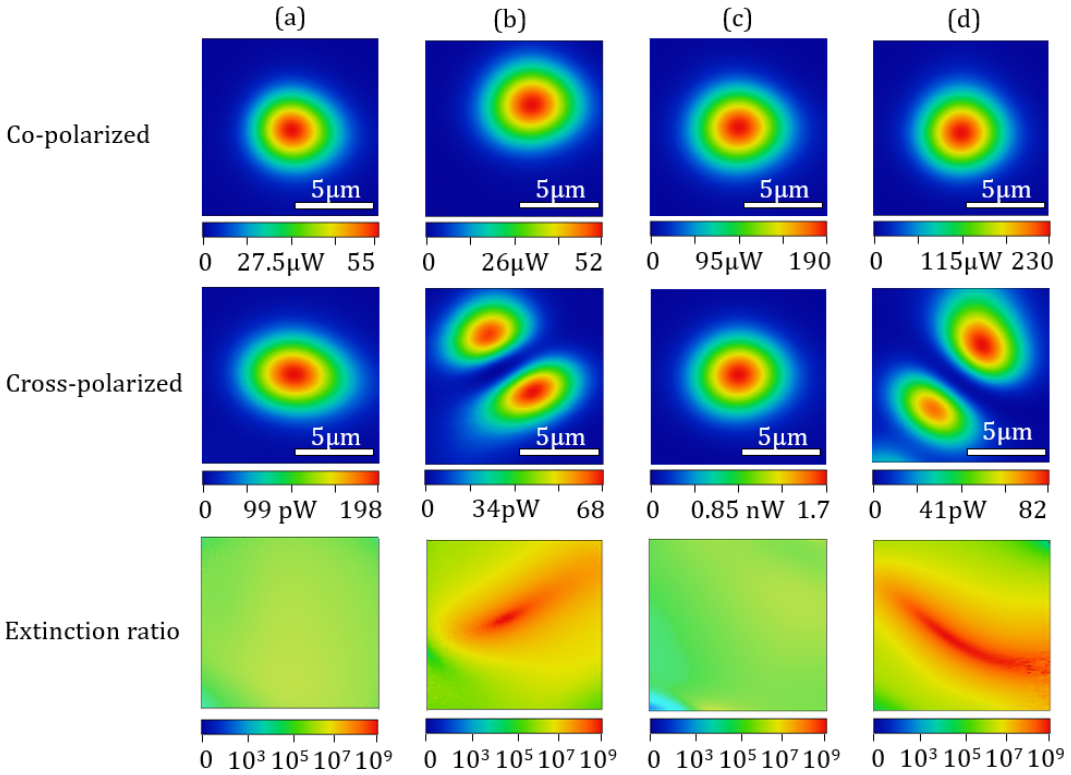

Figure 4.6: Confocal mapping of a polarized beam reflected off a beam-splitter cube (a)(b) and a high reflectivity Bragg mirror (c)(d). Here (a)(c) and (c)(d) are measurements with the analyzer placed before (Fig. 2.3a) and after (Fig. 2.3b) the test reflecting surface respectively. We plot the extinction ratio map by dividing, pixel per pixel, the co-with the cross-polarized data. The horizontal white bar represents 5μm.

As already discussed in previous sections, the measurements in the absence of a reflecting surface between the analyzer and polarizer in cross-polarization (see Fig. 4.6(a)(c)) show a pure TEM_{00} Gaussian mode field attenuated by 2.8×10^5 and 1.11×10^5 for non-polarizing beam-splitter cube and Bragg mirror, respectively. The measurements presented in Fig. 4.6(b)(d) are intended to show that a non-polarizing beam-splitter cube and a high reflectivity Bragg mirror behave like an ordinary metallic mirror in the case of total internal reflection, a condition for which there is an effect of cancellation of the polarization leakage as expected also from chapter 3. Here, the cross-polarization extinction is 2.18×10^8 and 1.01×10^8 for non-polarizing beam-splitter cube and a high reflectivity Bragg mirror, respectively. As shown in Fig. 4.7 (a)(c), the cross-polarization extinction amplification is reached with a correction to the analyzer

angle $\alpha - \alpha_0 = +0.876°$ and $-2.256°$ for a non-polarizing beam-splitter cube and Bragg mirror, respectively. In this respect, we found a striking difference in the maxima beam peak-shift and splitting positions as shown in Fig. 4.7(b)(d). In particular, the corresponding graph for a beam-splitter cube is reversed compared to the graph for the Bragg mirror. In another words, this means that the splitting effect reversed its sign. This effect, although interesting, is not relevant to our experiment since it does not affect the maximum cross-polarization extinction but it can be exploited to study polarization properties of beam-splitter cubes.

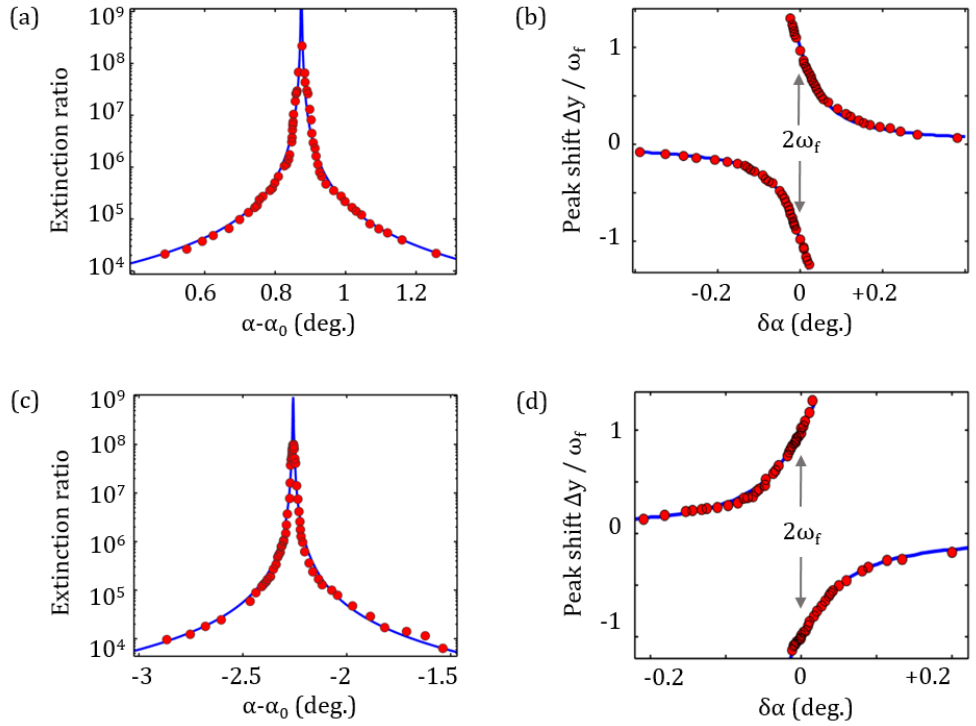

Figure 4.7: Measured and simulated extinction ratio (a)(c) for different analyzer angles α shifts for a polarized beam reflected off a beam-splitter cube (a)(b) and a high reflectivity Bragg mirror (c)(d).The maxima beam peak-shift are shown and modeled in (b)(d) in units of beam waist ω_f. Note that for the beam-splitter cube the peak shifts negatively first and then positively as the angle increased. This is very different from the metal reflectivity case (Fig.4.3 and 4.4).

Another interesting fact is that a tilt of the Imbert-Fedorov mode takes place at cross-polarization condition (Fig. 4.6(b)(d)) revealing that the reflected beam has a larger weight of the x component. This effect has been also measured for a protected silver mirror. For a reason not yet elucidated, this rotation occurs when varying the polarizer angle β through maximum cross-polarization extinction within a range between +4 and -4 degrees. The behavior seems consistent with a TEM_{10} mode that add coherently to the TEM_{01} Imbert-Fedorov mode that cause it to tilt. It is perhaps simply an experimental issue with the exactly optical alignment of our illumination-detection plane with the plane of incidence. This remains to be resolved.

Finally and for comparison we have also tested our model with a purely dielectric BK7 glass surface with reflectivity from the air-side near cross-polarization for the p-polarization. The results are shown in Fig. 4.8. In this configuration as expected from the model discussed in the chapter 3 indeed there is no shift $\alpha - \alpha_0$ between the condition of maximum cross-polarization for the dielectric and the reference measurement. As expected also from chapter 3 there is no effect of cancellation of the polarization leakage. The most remarkable difference is the way of the mode splitting evolves upon rotation of the analyzer. The absence of imaginary terms in r_p and r_s is the reason for this behavior. Here, we see not only the Imbert-Fedorov out of plane splitting at cross-polarization but also the appearance of the Goos-Hänchen mode showing a mixing that bends the beam shape along the plane of incidence. Fig. 4.8 shows in particular the evolution of the beam splitting near cross-polarization condition which is completely different from what is seen for metals such in in Fig. 4.3d and Fig. 4.4d. Because $Im(r_s r_p^*) = 0$ for the reflectivity from the air side of a dielectric there is no term linear in $\delta\alpha$ near cross-polarization conditions as also seen from the experiments. For a dielectric an analytical solution for the location of the lobes intensity maxima for very small analyzer rotation angle $\delta\alpha << 1$ near cross-polarization condition shows the quadratic evolution observed in our measurement.

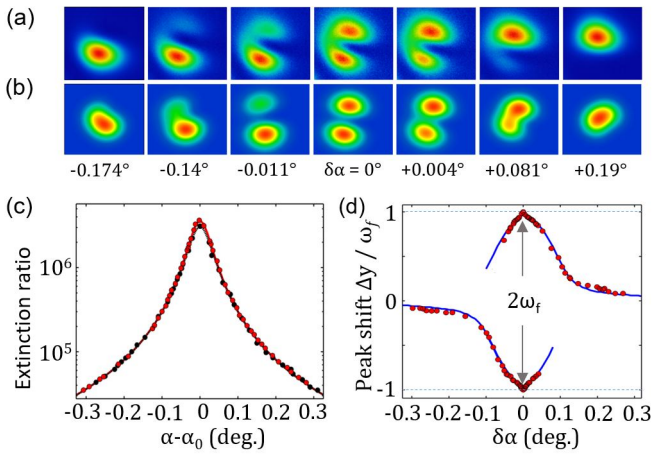

Figure 4.8: Measured (a) and simulated (b) evolution of the modal mapping through maximum extinction for reflectivity from the air side off a glass surface (BK7) in for p-polarization. (c) Red symbols: extinction ratio for different analyzer angles α shifts as explained in text. Black symbols: reference measurement with the analyzer placed just after the polarizers. The maxima beam peak-shift and splitting positions are shown and modeled in (d) in units of beam waist ω_f.

4.4 Experimental limits, so far

We identify three major limiting factors for the detection performance of our experiment; noise, alignment, and the angular resolution in the rotation of the polarizers. The cross-polarization extinction is primarily affected by the noise in photo-detection. We choose to show here the measured intensities at cross-polarization with a silver mirror (Fig. 4.9(a)(b)), beam-splitter cube (Fig. 4.9(e)(f)), Bragg mirror (Fig. 4.9(c)(d)) and dielectric BK7 glass surface reflecting from air (Fig. 4.9(g)(h)) using a logarithmic (a) and linear scale (b). The limit of detection is shown in dashed line and will be discussed in this section.

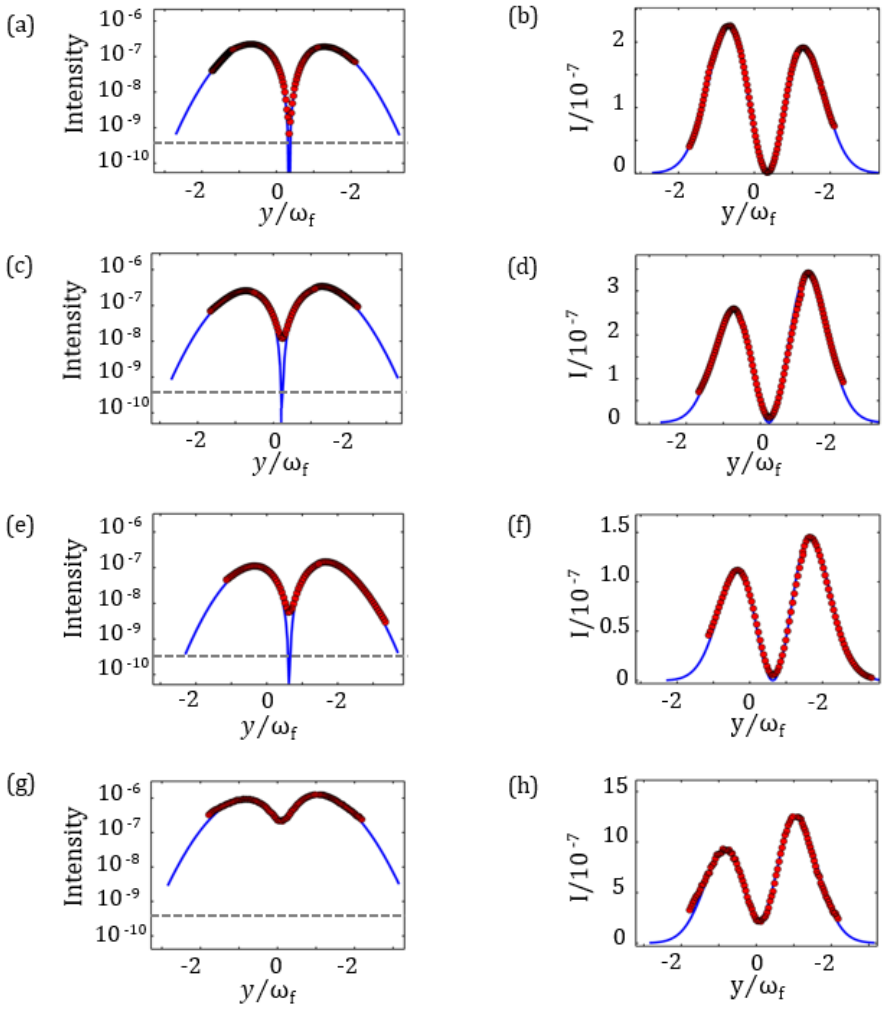

Figure 4.9: A linearly polarized laser beam reflected off a silver mirror (a)(b), (c)(d) Bragg mirror, beam-splitter cube (e)(f) and a glass surface BK7 (g)(h). For all measurements, the cross-polarized intensity is represented in a linear and logarithmic scale for better illustration of the extinction level. The limit of detection is shown in dashed line as discussed in text.

In all cases, except results for BK7 glass surface, an extinction beyond a level 10^8 is observed. At this point, we can conclude that the challenge in such

experiment is to enhance the signal with respect to the noise in photo-detection, known as signal-to-noise ratio. There are numerous sources that generate noise in a photo-diode detector such as thermal noise, shot noise, and dark noise.
As a starting point for discussion, we characterize the dark noise in photo-detection which occurs in the absence of a light input. Fig. 4.10 (a) is a plot of the output noise when the laser is completely darkened. The signal is detected using an integration time 5 ms namely in a bandwidth $\Delta f = 200\ Hz$ shows a noise standard deviation given by a root mean square (rms) value of 107.5 fW, a value comparable to the the manufacturer specification limit 84.85 fW (see section 2.2.3). In our case, the maximum intensity obtained in co-polarization scheme was limited to $233\mu W$. Thus, the noise limit is $N = 107.5\ fW/\ 233\ \mu W = 4.61 \times 10^{-10}$, which corresponds to an extinction limit of $1/N = 2.17 \times 10^{9}$. One way to improve further the extinction at cross-polarization is the use of a photon counting detectors with a dark noise readout usually much lower. Another point worth to mention here is that a good alignment of the setup can definitely lead to an enhancement of the signal-to-noise ratio. The result shown in Fig. 4.10 (b) is a magnification of the cross-polarized beam intensity near minimum for a silver mirror (Fig. 4.9(a)(b)). The minimum detected intensity is $I = 156\ fW/\ 233\ \mu W = 6.7 \times 10^{-10}$, a value to be compared to the dark noise limit $N = 4.61 \times 10^{-10}$. This measurement shows that we have reached a record level in the extinction value for which the limiting factor is the dark noise of the detector.

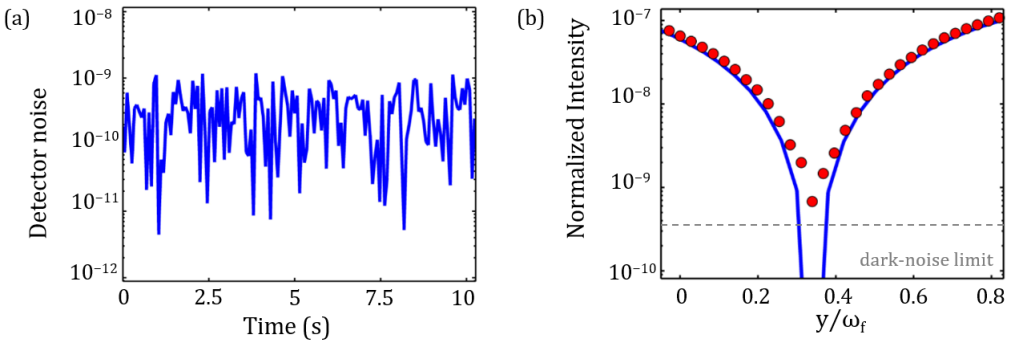

Figure 4.10: (a) The measured output noise without incident light when the laser is completely darkened using a logarithmic scale. (b) A magnification of the cross-polarized beam intensity near minimum for a protected silver mirror using a logarithmic scale. The dashed lines refer to the noise limit as discussed in the text.

We now discuss the shot noise limit in photo-detection. This type of noise is intrinsic to the quantum nature of the source and usually quantified as a function of the number of photons n that are collected by a given detector per unit of time. The standard deviation of shot noise is equal to the square root of the n detected photons per second and the signal-to-noise ratio takes the expression: $SNR = \sqrt{n}$. In our case, the detected signal in bright-field is 233 μW at a wavelength $\lambda = 905\ nm$, which corresponds to a total energy of $n\ \hbar\nu$ with

$\hbar = h/2\pi$ and h is Planck's constant: $6.626 \times 10^{-34}\ Joule - sec$. Since the energy of a single photon is $\hbar\, c/\lambda = 2.19 \times 10^{-19}$, we find a number of photons $n = 1.06\ 10^{15}$ produced per second. Thus, the signal-to-noise ratio is: $SNR = \sqrt{n} = 32 \times 10^6$, which we express in photons per square root of Hz. It implies a shot noise $7.28\ pW/\sqrt{\Delta f} = 102.97\ pW$ in a bandwidth $\Delta f = 200\ Hz$, a value about 1000 times more than the dark noise limit $107.5\ fW$. The shot noise due to the laser intensity is almost canceled at cross-polarization condition. In another words, our measurement procedure seems only affected by the dark noise in photo-detection with the exception of thermal noise, usually present in electronic circuits, that may limit the sensitivity of our photo-detector.

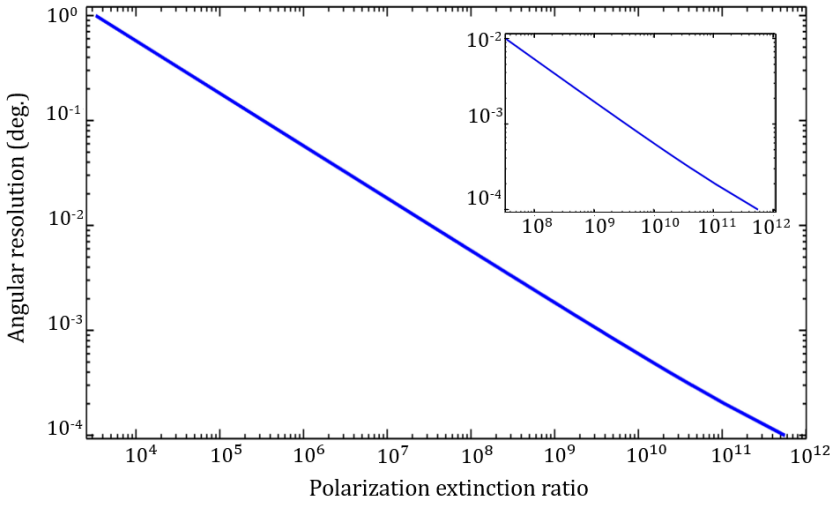

Figure 4.11: Modeled angular resolution as function of the cross-polarization extinction ratio. The inset is a magnification of the positioning resolution near maximum polarization extinction ratio for a linearly polarized beam obtained by placing the analyzer after a protected silver mirror.

Another point regarding the experimental limits that can be discussed is the angular resolution. The challenge in such experiment is to have a polarization rotator that enable stepping with small enough rotation angles. To illustrate this point further, we assume a plane wave and a perfect (non leaking) linear polarizer and analyzer combination. The analyzer is rotated by an angle θ with respect to the polarizer. For such an ideal setup, the detected transmitted intensity (normalized) is

$$I_0 = \cos^2\theta \tag{4.21}$$

The extinction (ER) is reached for $\theta = N\pi/2$ where N is an integer, this leads to $I_0 < 1/ER$. When $ER >> 1$ the condition is reached in a range of $\theta = N\pi/2 - \epsilon$ where $\epsilon << 1$. The goal here is to determine this range of ϵ given an ER limit. It follows

$$\cos^2\theta < 1/ER \tag{4.22}$$

This correspond to

$$\sin^2 \epsilon << 1/ER \tag{4.23}$$

Which for $ER >> 1$ approximates to

$$\epsilon^2 << 1/ER \tag{4.24}$$

In other words

$$-1/\sqrt{ER} < \epsilon < 1/\sqrt{ER} \tag{4.25}$$

This defines a range $\Delta\epsilon = 2/\sqrt{ER}$, which means that the analyzer rotator resolution should be better than $2/\sqrt{ER}$. To illustrate, in order to reach a systematically an extinction level of $ER = 10^{10}$ the resolution should be better than $2\times10^{-5}Rad$ or $1.15\times10^{-3}deg$, the same way to reach $ER = 10^8$ the resolution should be better than $2\times10^{-4}Rad$ or $1.15\times10^{-2}deg$. In practice, it is best to work with an angular resolution that is at least a factor 4 better than this limit and this in order to have enough sensitivity to set comfortably the condition of maximum extinction.
Fig. 4.11 is a plot of the angular resolution as a function of the cross-polarization extinction for which a protected silver mirror is sandwiched between the polarizer and the analyzer. The extinction enhancement strongly depends on the rotation angle and a change of only few mdeg can decrease the extinction intensity by one order of magnitude as seen in Fig. 4.11. For our experimental case, we have reached a record level of $I_0 = 6.7\times10^{-10}$ using a piezo rotating stages with $0.001°$ resolution around the optical axis [45]. This value is comparable with the theoretical resolution $5.17\times10^{-5}Rad$ or $3\times10^{-3}deg$. Thus, higher extinction values can only be reached through a piezo rotating stages with additional precision specifications. So far, this point has not been further investigated in this work.

Chapter 5

Circular polarization basis: direct imaging of Imbert-Fedorov effect in confocal microscopy

5.1 Motivation

Learning from the previous chapters, we are now moving our exploration to a more fundamental aspect of optics in order to test the predictive ability of the model and more importantly the experimental power of confocal microscopy to reveal very weak polarization effects. In particular here we want to focus on how reflecting surfaces affect circularly polarized light. What is well established is that a circularly polarized laser beam is reflected with spatial shift transverse to the plane of incidence [19, 20, 22, 33–38]. This Imbert-Fedorov shift, also known as "spin-Hall effect of light", was first measured by C. Imbert [20] for a laser beam of circularly polarized light in a glass prism under total internal reflectivity condition (Fig. 5.1(a)(b)). Depending on the chirality of its circular polarization, the trajectory of a circularly polarized beam will shift above or below the plane of incidence when reflected off a surface. This shift is due to spin-orbit coupling of light upon each reflection [21, 38, 46, 47] and is normally very small, typically, several orders of magnitude smaller than the photon wavelength. For this reason, it has previously required complex detection schemes limiting detailed experimental investigations. Here, we report about a novel method to measure and map the Imbert-Fedorov shift of Gaussian laser beam based on a dark-field cross-polarization technique in a confocal arrangement.

A considerable amount of literature [42, 48] exists about the measurement of Imbert-Fedorov shift using linear polarization state of light where the reflected beam mode splits into two lobes located above and below the reflectivity plane, as already discussed in previous chapters. In our view, this approach is not relevant to the spin-orbit coupling of light as the notion of a photon spin is usually connected to circular polarization. Because this displacement is perpendicular to the plane of reflectivity, the Imbert-Fedorov effect has been renamed as spin-Hall effect of light by authors like Onoda *et al.* [38], Bliokh *et al.* [46, 47],

Aiello *et al.* [49]. They interpreted the spin-orbit interaction of light in terms of geometrical phases and conservation of the total angular momentum of light, as already predicted by Liberman *et al.* in 1992 in an inhomogeneous medium [21]. More recent evidence of this effect has been shown by Bliokh *et al.* using multiple reflections in a cylinder glass in which the spin-Hall shift accumulates along a helical trajectory (Fig. 5.1(c)). In this case, the spin-Hall splitting is amplified through multiple reflections and becomes noticeable at higher number of turns (Fig. 5.1(d)). In this context, the well-known rotation of the polarization plane for a twisted trajectory is explained based on the Berry phase and the optical Magnus effect. The first observation of this phenomena in case of metallic reflection was demonstrated in [49] by Aiello and his team. In their experiment (Fig. 5.1(e)), they have directly measured the shift of a circularly polarized light instead of looking at the splitting of a linearly polarized light. The detected shift is in the nanometer range and not measurable at angle of incidence below 50° (Fig. 5.1(f)).

Despite the various approaches (Fig. 5.1) that have been developed to investigate the spin-Hall effect of light, this phenomena was not directly observed. It was only measured in some very special situations such as multiple reflections and a weak measurement scheme. This limits the use of this effect as a means for generating, manipulating, and detecting spin-polarized photons. The only evidence so far is a measurement of a polarization-differential shift either by varying the angle of incidence or the position of the detector. The uncertainty associated with the measurement of the shift raises many questions regarding the usefulness and experimental investigation of this effect. In this work, we aim to make a mental bridge between all these works and provide a clear explanation of the fundamental origins of the spin-orbit coupling of light at optical interfaces. For this purpose, we present a mechanical description of trajectory of a circularly polarized plane wave depending on its orbital angular momentum. We find a simple formula of the Imbert-Fedorov shift that reveals the polarization-dependent Hall effect of light previously discussed in literature. Same expression is derived using the full Maxwell approach which is relevant to explain the important subtleties of phase shifts induced by Fresnel coefficients upon reflection. We set up a simple, highly reproducible experiment to directly observe and measure the Imbert-Fedorov shift for circularly polarized Gaussian beam. Further measurements of the shift has been carried out using different angles of incidence $\theta_i = 44°, 30°, 21°, 13°$. We discover that a confocal arrangement in combination with a dark-field technique amplifies the visibility of the effect. In addition to new developments in spin-optics systems our experiments provide powerful tools to understand spin-orbit coupling of light, in the broader context of topological photonics.

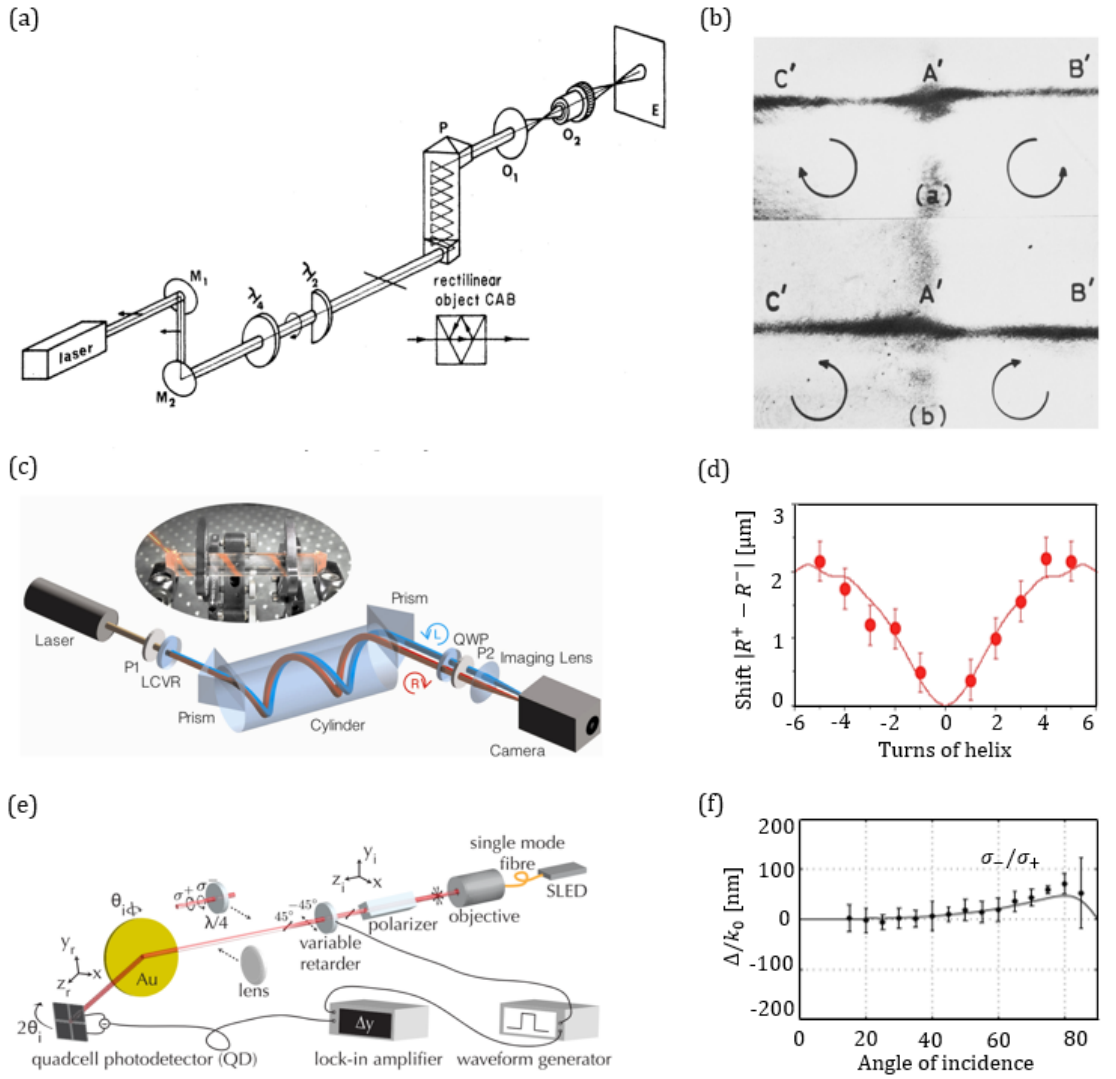

Figure 5.1: (a) Over-all experimental arrangement for measuring Imbert-Fedorov shift in circular polarization state. A laser beam, with horizontal linear polarization, traverses a quarter-wave plate and then a half-wave plate covering half of the beam; the resulting beam, which illuminates the rectilinear object CAB, is thus polarized circularly with opposite helicities on its two halves. This will produce the differential doubling effect we have alluded to. After illuminating the rectilinear object CAB, the beam enters either of our two multiplying prisms, and the image of CAB is finally observed. The high luminosity of the prism P allows this image to be projected on a screen. (b) Image of a rectilinear object displaying the transverse shift of a circularly polarized beam. The circular polarization states of the two halves of the beam are indicated. (See [20] for details). (c) Direct measurement of the spin-Hall of light in a glass cylinder in which the shift accumulates along a helical trajectory. (d) The relative shift between the two spin components versus the turns of the helix. (See [47] for details). (e) The optical set-up to measure the polarization-differential shift of a beam reflected off a thick gold film. (f) Measured polarization-differential shift between σ_-/σ_+ polarized light as function of the angle of incidence. (See [49] for details)

5.2 Spin and angular momentum of a plane wave

Optical angular momentum is an important concept to get a better understanding behind the concept idea of spin-orbit interaction put forward in the literature [38, 46, 47]. In this section, we present an alternative way to explain the transverse Imbert-Fedorov shift i.e spin-Hall effect of light using the conservation law of the z-component of the total angular momentum upon reflection at an optical surface. For an idealized circularly polarized plane wave of a wavevector $\vec{k}_0$ and momentum $\vec{p}$, the total angular momentum is expressed as $\vec{J} = \vec{L}_{ext} + \vec{S}$. It consists of the orbital (extrinsic) momentum $\vec{L}_{ext}$ and the spin (intrinsic) momentum $\vec{S}$ associated with beam trajectory and circular polarization (helicity), respectively. The classical definition of orbital angular momentum per photon is $\vec{L}_{ext} = \vec{r} \times \vec{p}$ where $\vec{r} = (\Delta x, \Delta y, \Delta z)$ is the position vector of the plane wave and $\vec{p} = \hbar \vec{k}_0$, with $\hbar = h/2\pi$, h is the Planck's constant: 6.626×10^{-34} $J.s$. The spin angular momentum per photon is often expressed as $\vec{S} = \sigma \hbar \, \vec{k}_0 / |\, \vec{k}_0 \,|$, with $\sigma = \pm 1$ for left- and right-handed circularly polarized light respectively and $\sigma = 0$ for linearly polarized light.

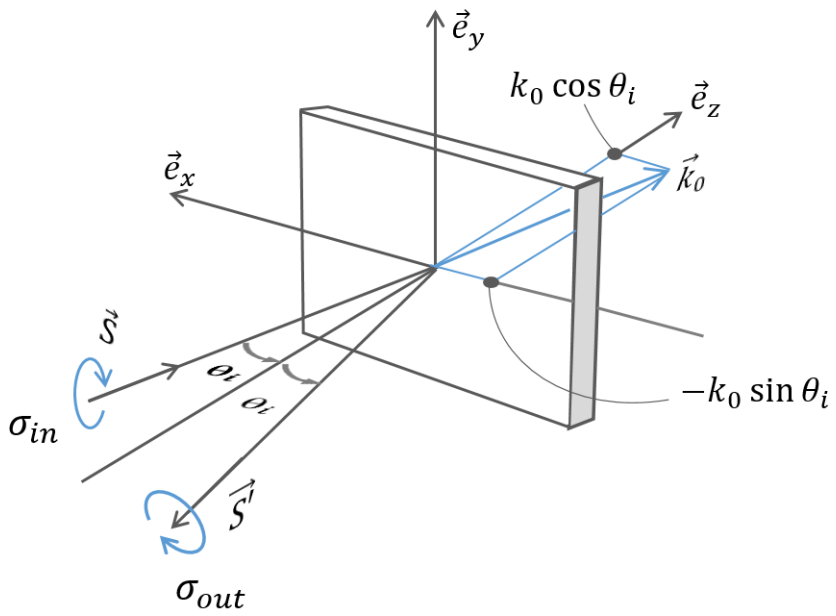

Figure 5.2: Schematic drawing of a circularly polarized plane wave reflected off an optical surface. The projection of its wavevector $\vec{k}_0$ on the basis $(\vec{e}_x, \vec{e}_y, \vec{e}_z)$ is $(-k_0 \sin\theta_i, 0, k_0 \cos\theta_i)$ where θ_i is the angle of incidence as explained in text. σ_{in} and σ_{out} are the polarization helicity state of the incoming and reflected plane wave, respectively.

When the plane wave is reflected off an optical interface, the z-component (normal to the surface) of the total angular momentum $\vec{J}$ between the incident and reflected wave is conserved assuming that the geometric configuration remains unchanged after rotating around the z-axis. The conservation law gives the following expression: $\vec{S}.\vec{e}_z = \vec{S}'.\vec{e}_z + \vec{L}_{ext}.\vec{e}_z$, where $\vec{L}_{ext} = \vec{r} \times \vec{p}$ is an orbital

angular momentum with $\vec{p} = \hbar\vec{k}_0$ and $\vec{r} = (\Delta x, \Delta y, \Delta z)$ an effective orbital radius to be determined.
The conservation equation can be written as $\hbar k_0 \sigma_{in} \cos\theta_i = -\hbar k_0 \sigma_{out} \cos\theta_i + \vec{L}_{ext}.\vec{e}_z$, where σ_{in} and σ_{out} are the polarization helicity state of the incoming and reflected plane wave, respectively. Here,

$$\vec{L}_{ext} = \hbar k_0 \begin{bmatrix} \Delta x \\ \Delta y \\ \Delta z \end{bmatrix} \times \begin{bmatrix} -\sin\theta_i \\ 0 \\ \cos\theta_i \end{bmatrix} \tag{5.1}$$

By calculating the cross product we can verify that

$$\vec{L}_{ext} = \hbar k_0 \begin{bmatrix} \Delta y \cos\theta_i \\ -\Delta x \cos\theta_i - \Delta z \sin\theta_i \\ \Delta y \sin\theta_i \end{bmatrix} \tag{5.2}$$

Setting up the total angular momentum conservation of the z-component:
$\hbar\ \sigma_{in} \cos\theta_i = -\hbar\ \sigma_{out} \cos\theta_i + \Delta y \sin\theta_i$, leads to an analytical expression for the displacement Δy in a direction perpendicular to the plane of reflection. In a compact form, we show that

$$\Delta y = \frac{\sigma_{in} + \sigma_{out}}{k_0\ \tan\theta_i} \tag{5.3}$$

This simple equation guides us towards the optimal strategy to perform an experiment providing the largest Δy. For an ideal metallic mirror with 100% reflectivity, $\sigma_{out} = -\sigma_{in}$. This is because a perfect mirror also mirrors the helicity of the polarization meaning that the sum of the spin cancels out $\sigma_{in} + \sigma_{out} = 0$ and there is no shift Δy above or below the plane of incidence. For a real mirror such as a silver mirror, the sum $\sigma_{in} + \sigma_{out}$ expresses the proportion of minority photons that are reflected with the same spin. It is a direct measurement of the circular depolarization. A distinctive feature of the shift Δy is the fact that it is independent of the material properties and beam size of the incident light attesting to the robustness of this effect. Because this displacement is perpendicular to the plane of reflectivity, it is also dubbed spin-Hall effect of light. Now the maximum value of Δy that can be reached is when $\sigma_{out} = -\sigma_{in}$, which is also $\sigma_{in} + \sigma_{out} = 2$. This situation can be experimentally realized by sorting out the majority photons that do not contribute to the maximum sum $\sigma_{in} + \sigma_{out}$ and keep the photon conserving the spin which maximizes the sum. Practically, we use a dark-field cross-polarization technique in a confocal arrangement where a circular analyzer placed on the reflected beam path just to allow the photons with the same helicity as the incoming beam to reach the detector as explained in section 5.3. In what follows, we evaluate that shift.

5.3 Confocal imaging of Imbert-Fedorov shift

5.3.1 Experimental setup with circularly polarized light

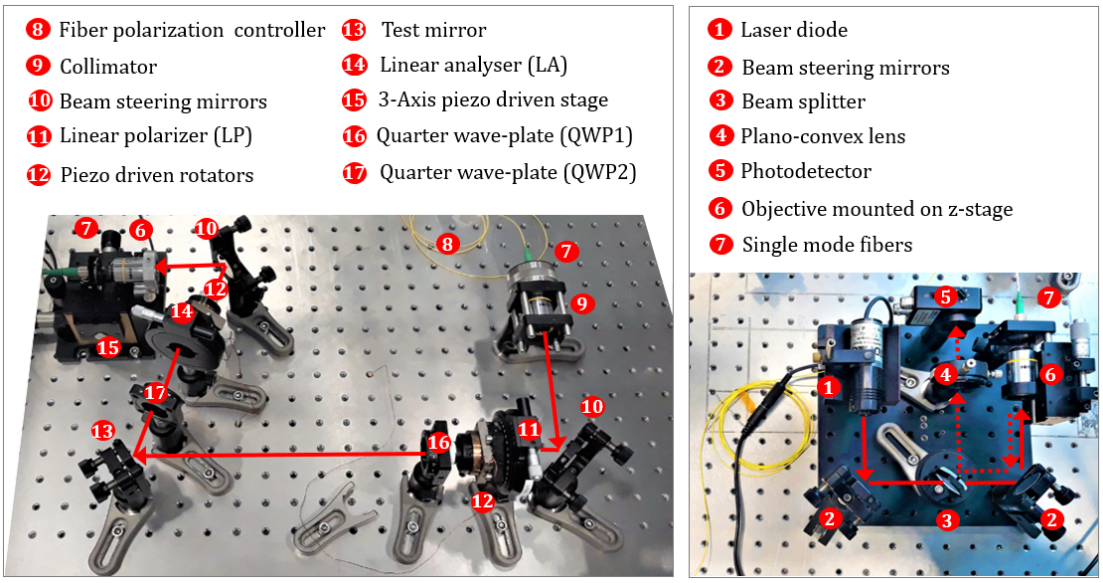

Figure 5.3: (Left) Experimental setup for measuring and observing the Imbert-Fedorov shift of a circularly polarized laser beam. (Right) Coupling of the laser source is done in a separate step. Red solid and dashed lines indicate the excitation and the reflection ray path respectively. See section 2.2.3 for details.

We used the already-introduced confocal arrangement (section 2.2) in order to emphasize the most relevant physics leading to the Imbert-Fedorov shift of a circularly polarized Gaussian beam reflected off a test mirror. The quarter-wave plates QWP1 and QWP2 allow and reciprocally for conversion of light from the linear to the circular or elliptical polarization (or vice versa). We choose a zero-order quartz retarders (Thorlabs WPQ05M) with a wavelength 915±35nm, because they offer a lower dependence on temperature and wavelength than multi-order wave plates. Each quarter wave-plate is mounted in a continuous rotation mount with adjustable zero (Thorlabs RSP1D) and an angular resolution of 5*arcmin* Vernier Scale ($\approx 0.083°$). In contrast to cross-polarization extinction measurement, high angular resolution is not a crucial requirement for detecting the Imbert-Fedorov shift. However, the circular polarizer and analyzer are important optical components for the experiment and the challenge here is to be able to generate circular light with sufficiently high-purity of polarization state. In order to provide a direct observation of the beam displacement upon reflection, we mapped the detected intensity by scanning the spatial position of the collecting fiber in the focal plane of the focusing objective. We performed same measurement for different angles of incidence by adjusting the position of the reflecting test surface (13) as depicted in Fig. 5.3(left). It is also indispensable to produce high-fidelity imaging of the confocal light and also high-precision measurements of the Imbert-Fedorov shift. In the next section (5.3.2), we ex-

plain our experimental procedure for generating the circular polarization and measuring the beam shift.

5.3.2 Experimental results with circularly polarized light

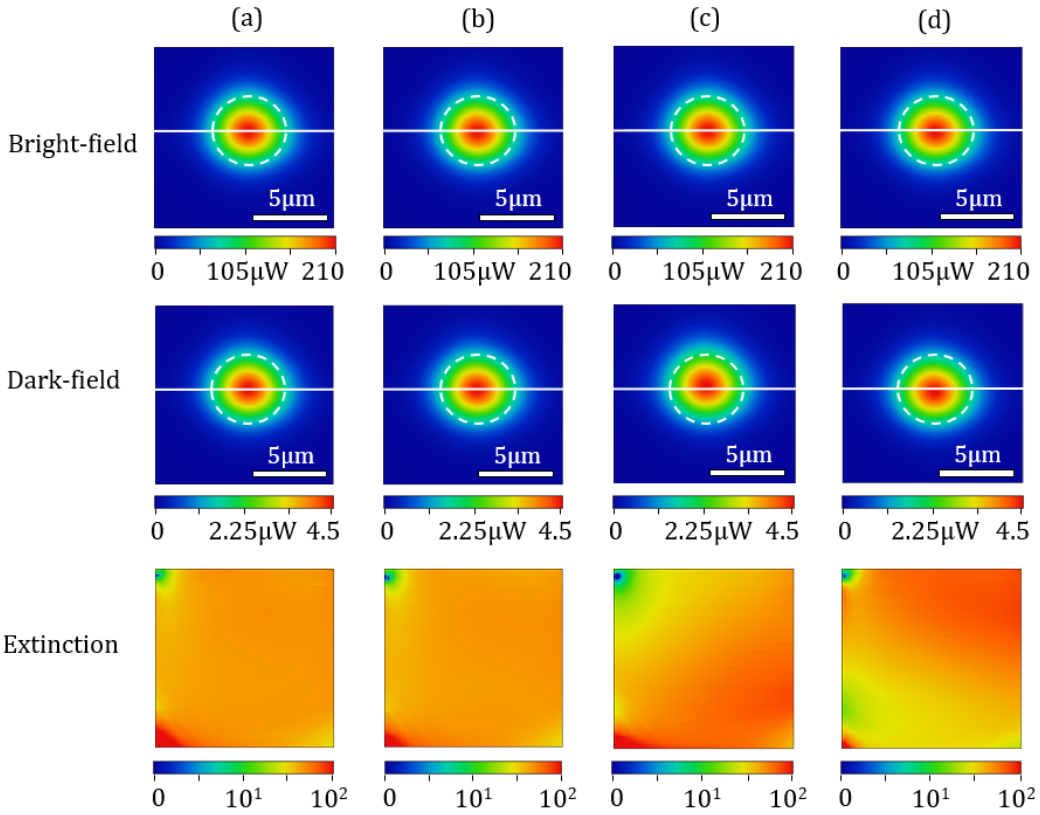

Figure 5.4: Confocal imaging of a (a) +45°, (b)−45°, σ_+ and σ_- polarized beam off a test mirror surface in a bright-field (first row) and dark-field (second row) arrangement. We plot the extinction ratio map in logarithmic scale by dividing, pixel per pixel, the bright-field with the dark-field data. In dark-field, a beam shift along $\vec{e}_y$ above and below the plane of incidence is observed both for the σ_+ and σ_- polarization. The dotted line circle is the $1/e$ intensity level of the Gaussian distribution resulting from the confocal convolution between the focused spot and the collecting fiber mode. The diameter of this circle gives also the non-convoluted focal spot waist diameter at $1/e^2$ focused on the collecting fiber end. The horizontal white bar represents 5μm.

In our experiment, we use a linear polarizer next to a quarter-wave plate to generate light of circular polarization. We start out by setting the linear polarizer angle β near 0 for p-polarization (Fig. 5.5(b)) and the linear analyzer angle α near cross-polarization at $\beta \pm \pi/2$ (Fig. 5.5(a)). This step is necessary for recognizing the p or s reference. The field vector along the p (or s) plane is written as: $(1,0)$ (or $(0,1)$). Once the maximum extinction is reached, the linear polarizer (LP) is rotated visually at +45° by reading the graduations on

the Thorlabs manual rotator. The analyzer angle must be then rotated by 90° to be set at −45° in order to maximize the collected confocal intensity at the detector i.e bright-field mode (Fig. 5.5(d)). The detected field for +45° linear polarization in a bright-field confocal arrangement is shown in Fig. 5.4(a)(first row). To operate in dark-field mode (Fig. 5.5(c)), β remains untouched and we set the analyzer at the same helicity i.e +45° because the mirror flips the sign of the chirality. The detected field in the dark-field mode is shown in Fig. 5.4(a)(second row). The measurements in Fig. 5.4(a)(b) show by a factor a pure TEM_{00} Gaussian mode field in bright-field arrangement attenuated by 46.79 and 46.83 for +45° and −45° linearly polarized beam, respectively. In terms of Imbert-Fedorov i.e spin-Hall experiment, we want to come to the mirror with a selected photon spin and measure after the mirror the number of photons that made it out to the detector with the exact same spin. For this case, we place a first quarter-wave plate (QWP1) after the linear polarizer (LP) at +45° and before the mirror. The QWP1 is mounted on a Thorlabs rotator in a way that its fast axis is along the p plane (i.e. horizontal in our setup). In this case, the linearly polarized light beam has an angle of +45° with the fast axis, the phase shift will be $\pi/2$ between polarization components and the out-going light beam is circularly polarized. When the linear polarization is parallel to the fast axis, there is no phase shift and no change in the polarization state. Next, the second quarter-wave plate (QWP2) is added after the mirror and before the linear analyzer (LA). Since the mirror flips the chirality of the beam, we use the combination {QWP2, LA +45°} and {QWP2, LA −45°} to switch between dark-field and bright-field modes as illustrated by Fig. 5.5(e) and (f) respectively, assuming a left-hand incident circular polarization σ_+ i.e {LP +45°, QWP1}. In the same way, we define the combination {QWP2, LA −45°} and {QWP2, LA +45°} to switch between dark-field and bright-field modes respectively in case of right-hand circular polarization σ_- i.e {−45° LP, QWP1}.

To get a feel of the measured Imbert-Fedorov shift for a circular polarization σ_+ and σ_- at an angle of incidence $\theta_i = 44°$, we measured and showed in Fig. 5.4(c)(d) the confocal light intensity in a bright-field and dark-field arrangement(Fig. 5.5(f)(e)). We observed that the reflected beam spot measured in dark-field arrangement is displaced perpendicularly to the plane of incidence. The peak-shift occurs along $\vec{e}_y$ and located above or below the reflectivity plane for σ_+ and σ_- polarization, respectively. The measured subwavelength shift showed in Fig. 5.6 is $y_{\sigma_+} = +330nm$ and $y_{\sigma_-} = -340nm$ when switching between circular polarization σ_+ and σ_-. Thus, the total displacement is $\Delta y = 670nm$. This is consistent with the value $2 \times (\lambda/\pi) cot\theta_i = 596nm$, calculated using the expression (5.3) for a simple plane wave reflected of a silver mirror at $\theta_i = 44°$ and $\lambda = 905nm$. In this dark-field configuration, we find an extinction ratio 47.59 and 47.86 for σ_+ and σ_- polarization, respectively. Here, it is worth to mention that the measured extinction ratio for σ_+ and σ_- have almost a value similar to the value for +45° and −45° linearly polarized beam, respectively. This reflects the fact that quarter-wave plates aligned along its fast or slow axis do not reduce the intensity of the incident ±45° incident light, as it passes through it.

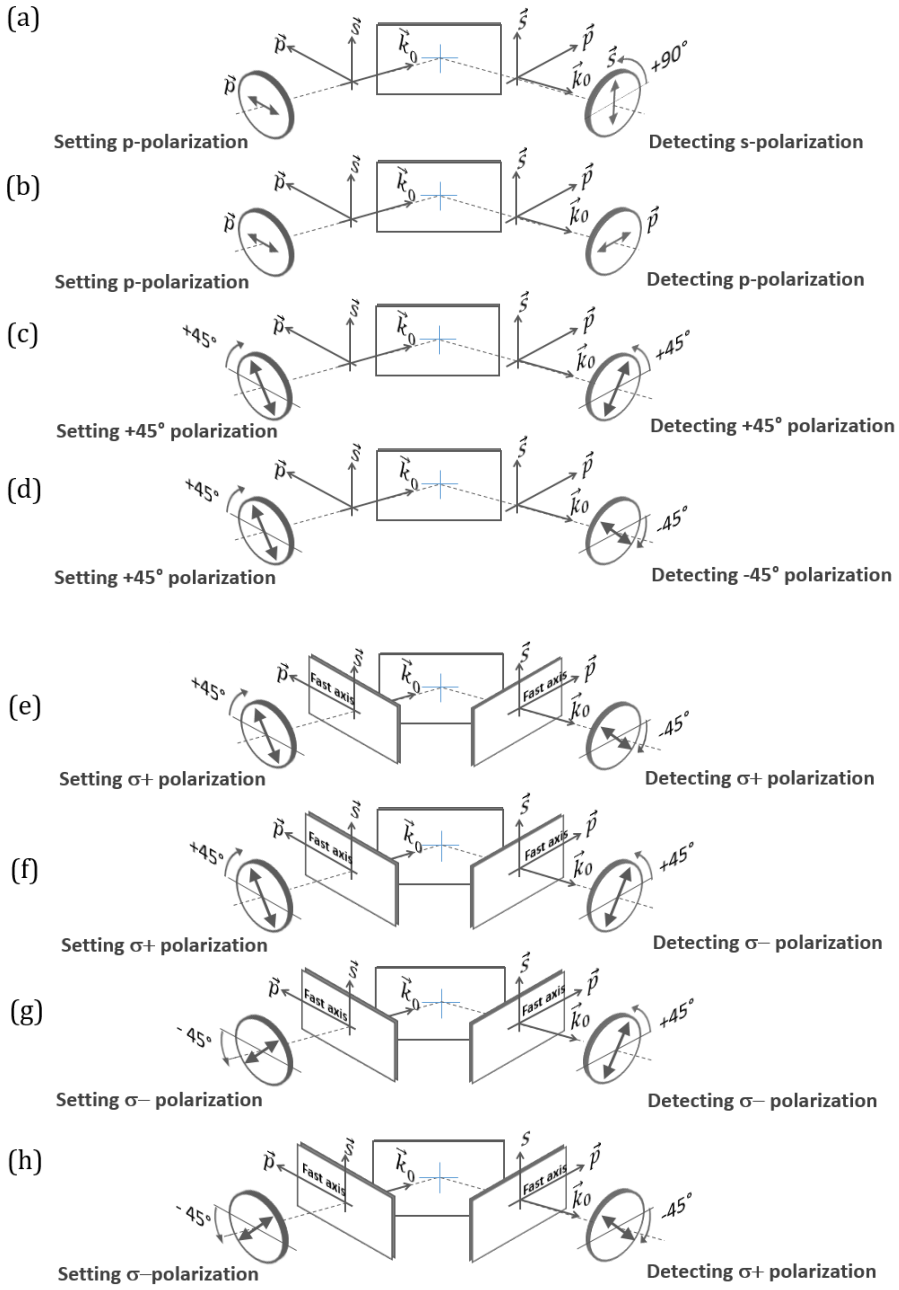

Figure 5.5: Measurement protocol for observation of the Imbert-Fedorov shift upon reflection. First we set a linear *p*-polarization in (b) co-and (a) cross-polarization scheme, respectively. Next, the linear polarizer is rotated at +45°. For the bright-field arrangement the linear polarizer (LP) and the lineare analyzer (LA) are set up in parallel (d) while for the dark-field arrangement they are rotated by 90°. Two quarter-wave plates QWP1 and QWP2 are then added directly before and after the mirror, respectively. The fast axis of both wave-plates is parallel to *p* plane. In this geometry, the dark-field and bright-field arrangement are shown in (e) and (f), respectively. To measure the shift in the opposite direction, the polarizer is rotated by 90° in a dark-field arrangement as shown in (g). Then, the analyzer is rotated also by 90° to switch to bright-field mode as illustrated in (h).

The first important condition for the success of our experiment is the stability of the maxima beam position during the confocal imaging process. Keeping this in mind, we present in Fig. 5.4(first row) the confocal imaging in a bright-field arrangement, where the location of the maxima of the beam lie exactly on the circle indicating the $1/e$ intensity level of the Gaussian distribution. This indicates that our setup is mechanically stable and not affected by any drift problem which leads to moving the beam maxima location. We have also experimentally verified the stability and the reproducibility of the shift on the reflected confocal spot under different incidence angles for instance $\theta_i = 30°, 21°, 13°$ attesting to the robustness of this effect. We observed similar behavior for all the mentioned angles of incidence, with the difference that the value shift is amplified while decreasing the incidence angle as already predicted from expression 5.3: $2 \times (\lambda/\pi) cot\theta_i$. Corresponding experimental results are shown and discussed in section 5.4. Here we show results for 29° as depicted in Fig. 5.6. In this case, the shift is $y_{\sigma_+} = +680 \pm 0.04nm$ and $y_{\sigma_-} = -680 \pm 0.04nm$ when switching between a polarization σ_+ and σ_-, respectively. These values are comparable to the calculated value using the plane wave model $(\lambda/\pi) cot\theta_i = 520nm$, with $\lambda = 905nm$. The difference could be possibly related to the purity of the polarization state of light.

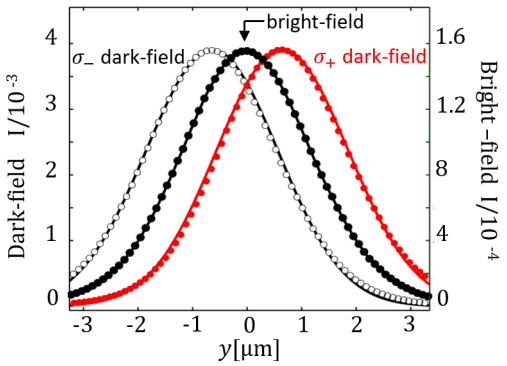

Figure 5.6: Measured and calculated circularly polarized laser beam reflected off a silver mirror in a dark-field confocal arrangement for $\theta_i = 29°$ incidence angle. The bright-field beam (black circles) is centered in the middle with maximum intensity $160\mu W$. The measured intensity profiles for σ_+ and σ_- polarization are shown using red and white circles, respectively. The measured shift is $y_{\sigma_+} = +680 \pm 0.04nm$ and $y_{\sigma_-} = -680 \pm 0.04nm$ when switching between circular polarization σ_+ and σ_-, respectively.

The challenge in this experiment towards proving the existence of such subwavelength shift is to check the purity of the generated circular polarization by combination of the linear polarizer and the quarter-wave plate (QWP1). A quarter-wave plate has two principal axes: fast and slow. Each axis has a different refractive index and, therefore, a different wave velocity. If the light after the linear polarizer is at ±45° and the quarter-wave plate is aligned at an angle other than the fast or slow axis, then the output will be elliptically polarized. Thus, the knowledge of the fast or slow axis of the quarter-wave plate is crucial for

manipulating the polarization state of light beams. It is worth to mention here that the output light from a quarter-wave plate aligned along the fast or slow axis is left or right-hand circular polarization. The commercial quarter-wave plates we used in this work had already the fast axis denoted by a line. Otherwise, it may be found out easily by verifying that the dark-field intensity on the detector decreases by 1/2 as compared to a p or s polarization. In fact, the normalized field intensity in the dark-field confocal arrangement for +45° linear polarization is given by equation (3.6) for $\beta = \pi/4$ and $\alpha = \pi/4$. This is expressed by: $I = |r_p + r_s|^2/4$. First thing to note from this formula is that the sum $r_p + r_s$ governs the dark-field detected field intensity. Later in the analysis (section 5.5) we will see that this sum appear as pre-factors in the description of circularly polarized reflected fields.

$ER_{measured}$	ER_{theory}	θ_i	$\Delta_{measured}$	$\Delta_{reference}$
47.73 ± 0.15	93.37	44°	$98.32° \pm 0.02°$	95.94°
$(2.53 \pm 0.03) \times 10^2$	4.96×10^2	30°	$93.60° \pm 0.02°$	92.57°
$(1.16 \pm 0.01) \times 10^3$	2.18×10^3	21°	$91.68° \pm 0.01°$	91.23°
$(1.02 \pm 0.04) \times 10^4$	1.52×10^4	13°	$90.57° \pm 0.02°$	90.46°

Table 5.1: Overview of the measured extinction ratio $ER_{measured}$ and phase difference $\Delta_{measured}$ for different incidence angles $\theta_i = 44°, 30°, 21°, 13°$. Reference values of $ER_{reference}$ and $\Delta_{reference}$ are determined from [28].

It is worth emphasizing that an ideal mirror i.e $r_p = 1$ and $r_s = -1$ reverses the chirality of the photon meaning that $r_p + r_s = 0$. For high reflectivity materials such as silver mirror, we have $r_p + r_s = 2cos\Delta$ where $\Delta = (\phi_p - \phi_s)/2$ is the phase difference (see section 3.2 for more details). The significant result from the formula of the detected field in dark-field arrangement is the fact that the extinction ratio $1/I = 4/|r_p + r_s|^2$ which is also $1/(\cos^2 \Delta)$, is a direct measurement of the purity of the generated circular polarization as reported in table 5.1. We have measured the extinction ratio in a dark-field configuration for different angles of incidence $\theta_i = 44°, 30°, 21°, 13°$. In particular, a good agreement between theoretical and experimental values is found, highlighting the highest purity of circular polarization. We have also determined the corresponding phase difference $\Delta_{measured}$ for each $\theta_i = 44°, 30°, 21°, 13°$. In fact the incidence angles are deduced from the measurement of the extinction ratio. In practical, we set a rough nominal incidence angle θ_i, then compare the measured (ER) to the reference value reported from literature [28] for silver and then we deduce

the exact value of θ_i. This technique used for measuring the phase difference $\Delta = (\phi_p - \phi_s)/2$ is a simple way for incidence angle calibration in a variety of high-precision measurement in polarimetry and micro-ellipsometry. In conclusion, the significant results in table 5.1 report on a robust method based on dark-field confocal arrangement to directly measure and check the purity of the polarization state of light taking advantage on the effect that light reflected by a metallic surface introduces a phase shift between the p and s components of the beam due to the Fresnel reflectivity coefficients r_p and r_s.

5.4 Measurements at different angles of incidence

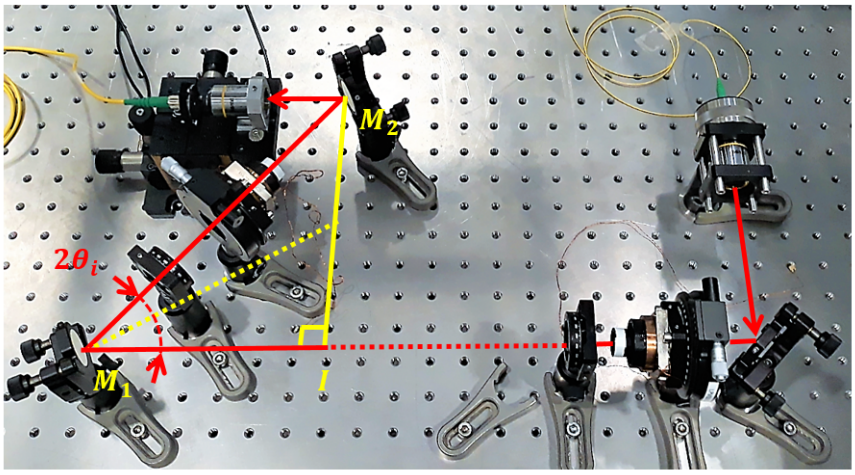

Figure 5.7: Rough way to set the incidence angle θ_i. It is measured using a tangent function $\tan 2\theta_i = IM_2/IM_1$ in the triangle (IM_1M_2). The distance IM_2 remains unchanged and only the distance IM_2 is adjusted by horizontal translation of the test mirror in order to vary the angle of incidence θ_i of the laser beam. An exact measurement of incidence angle θ_i is finalized through ER measurements as discussed in text.

Following equation 5.3 for plane wave the Imbert-Fedorov shift is expected to evolve as $cotg\theta_i$, in other words we are compelled to explore the smaller angles region. Here, we were interested in observing the shift at angles of incidence $\theta_i = 44°, 30°, 21°, 13°$. In practice, we have setup four different experiments given a specific θ_i angle setting. In particular, the test mirror is moved relative to the incident light beam to change the angle between the beam and the test surface mirror. The reflected beam travels off at an angle of reflection which is equal to the angle of incidence according to the law of reflection. The angle of incidence is predicted by a tangent function as depicted in Fig. 5.7.
For each incidence angle θ_i setting, we have mapped the confocal light intensity, for σ_+ and σ_- circular polarization, measured in a bright-field (Fig. 5.8) and dark-field (Fig. 5.9) arrangement, respectively. Only half beam is shown for each circular polarization for better illustration of the direct observation of the Imbert-Fedorov shift. In all cases, the bright-field intensity profile is essentially

a reminiscent of a TEM_{00} Gaussian beam for σ_+ and σ_- polarization, respectively. The location of the peak intensity is centered at 0, there is no maxima position technical spurious drift of the laser beam during the confocal scanning process which might be caused by poor mechanical mounting of the optomechanical parts or upon rotation of optical components such as the quarter-wave plate. These measurements (Fig. 5.8) are intended to evaluate the beam-positioning performance of our setup as well as examine the fidelity and long-term stability over 24 hours, of the Imbert-Fedorov shift measured in the dark-field confocal arrangement. We have experimentally verified the stability of the beam maxima position $\theta_i = 44°, 30°, 21°, 13°$ as depicted in Fig. 5.8(e)(f)(g)(h) attesting to the robustness of the experimental setup.

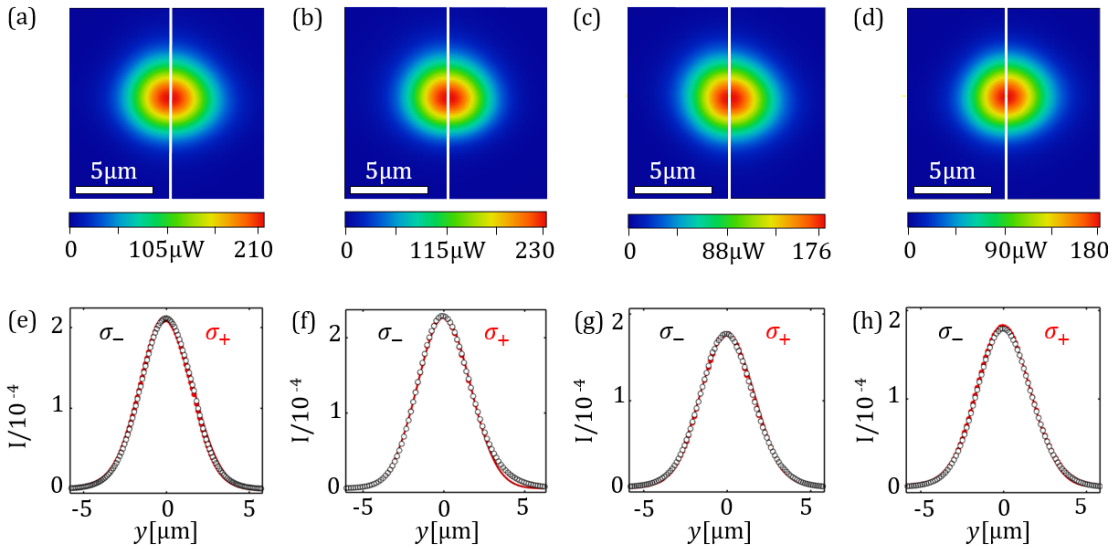

Figure 5.8: Bright-field measurements in a confocal arrangement for incidence angles $\theta_i = 44°(a)(e), 30°(b)(f), 21°(c)(g), 13°(d)(h)$ when using σ_+ and σ_- circular polarization. The measurements demonstrate that no technical spurious shifts affect our experimental setup in configurations for which no measurable shift is expected. Only half beam is shown for each circular σ_+ and σ_- polarization. The measured intensity profiles for σ_+ (red circles) and σ_- (white circles) polarization are shown in the lower row.

We now discuss the results in Fig. 5.9 where the confocal light intensity for σ_+ and σ_- circular polarization is measured in dark-field arrangement. The most striking result to emerge from the data Fig. 5.9(a)(b)(c)(d) is that the Imbert-Fedorov shift i.e spin-Hall effect is amplified as the angle of incidence θ_i decreases. This finding confirms the initial calculations of conservation of total angular momentum for a simple circularly polarized plane wave reflecting off a metallic mirror (section 5.2). In our measurement procedure of the shift, we use the least-squares method to fit a Gaussian model to our experimental data. The beam shift $y_{\sigma\pm}$ is measured with a fitting error between the experimental values and those given by the fitted curve. Our measurements of the Imbert-Fedorov shift for σ_+ and σ_- circular polarization are summarized in table 5.3.

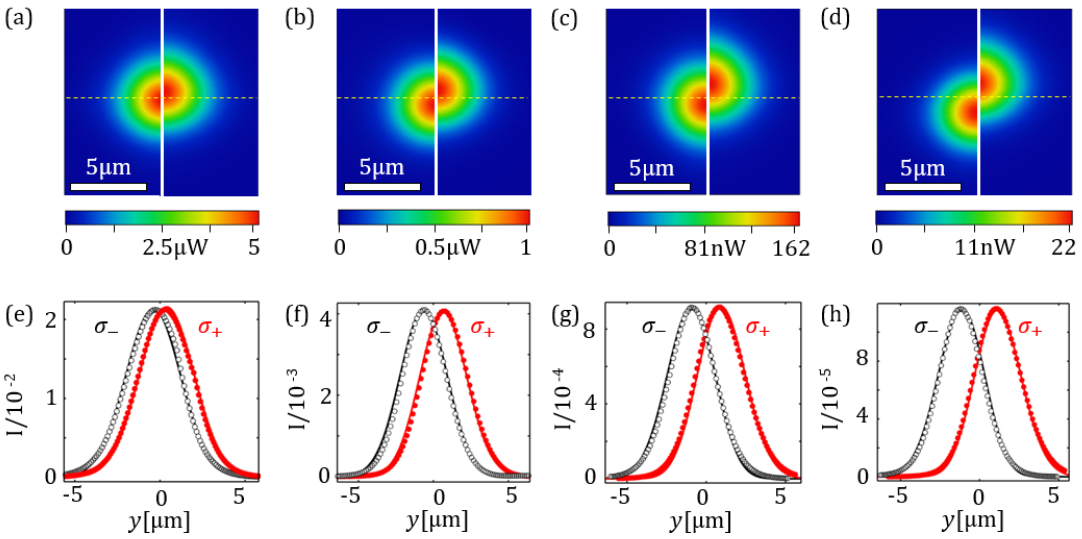

Figure 5.9: Analysis of the Imbert-Fedorov shift for σ_+ and σ_- polarization in a dark-field confocal arrangement for incidence angles settings $\theta_i = 44°(a)(e), 30°(b)(f), 21°(c)(g), 13°(d)(h)$. Only half beam is shown for each circular σ_+ and σ_- polarization. The measured intensity profiles for σ_+ (red circles) and σ_- (white circles) polarization are shown in the lower row.

There is no significant differences between the measured $\Delta y_{measured} = y_{\sigma+} - y_{\sigma-}$ and calculated $\Delta y_{planewave} = 2 \times (\lambda/\pi) cot\theta_i$ total displacement of the opposite shifts of the two circular polarizations in case of $\theta_i = 44°, 30°, 21°, 13°$ incidence angles. It is worth to mention here that the data at 13° is no longer explained by the simplistic model of plane wave. To the best of our knowledge, we are the first to now see the departure from the divergence given by the plane wave approximation for low angles of incidence. The agreement with Gaussian model is excellent as we will discuss later in this chapter.

At this point, we were able to directly observed the Imbert-Fedorov shift in case of metallic reflection through the use of dark-field confocal arrangement. Specifically, we used a powerful technique based on cross-polarization measurement to filter away photons that are not experiencing spin-orbit coupling upon reflectivity. So far, all the presented experimental results except for $\theta_i = 13°$ are in good agreement with the simple argument that for a plane wave the conservation of the projection of angular momentum along the mirror normal axis (i.e. mirror rotation invariance around that axis) the wave is displaced perpendicularly to the plane of incidence. This cannot be measured for a plane wave as it has an infinite extend and therefore its location cannot be defined. However for a finite sized beam, such a Gaussian beam, we have shown that this shift is clearly observable. In what follows we uncover the physics responsible for Imbert-Fedorov shift for a Gaussian beam and we will explain convincingly all the features of the measured results.

θ_i	$y_{\sigma-}$	$y_{\sigma+}$	$\Delta y_{measured}$	$\Delta y_{planewave}$
44°	$-340 \pm 0.03nm$	$+330 \pm 0.03nm$	$670nm$	$596nm$
30°	$-500 \pm 0.02nm$	$+520 \pm 0.03nm$	$1.02\mu m$	$997nm$
21°	$-710 \pm 0.01nm$	$+710 \pm 0.02nm$	$1.42\mu m$	$1.50\mu m$
13°	$-1050 \pm 0.02nm$	$+1040 \pm 0.02nm$	$2.09\mu m$	$2.49\mu m$

Table 5.2: Overview of the measured Imbert-Fedorov shift for different incidence angles $\theta_i = 44°, 30°, 21°, 13°$. For each θ_i angle setting, we measure the Imbert-Fedorov shift for σ_+ and σ_- circular polarization. $\Delta y_{measured} = y_{\sigma+} - y_{\sigma-}$ corresponds to the total displacement of the opposite shifts of the two circular polarizations. The theoretical value of $\Delta y_{planewave} = 2 \times (\lambda/\pi) cot\theta_i$ is determined for $\lambda = 905nm$ as explained in text (see section 5.2 for details).

5.5 Imbert-Fedorov shift for a circularly polarized Gaussian beam

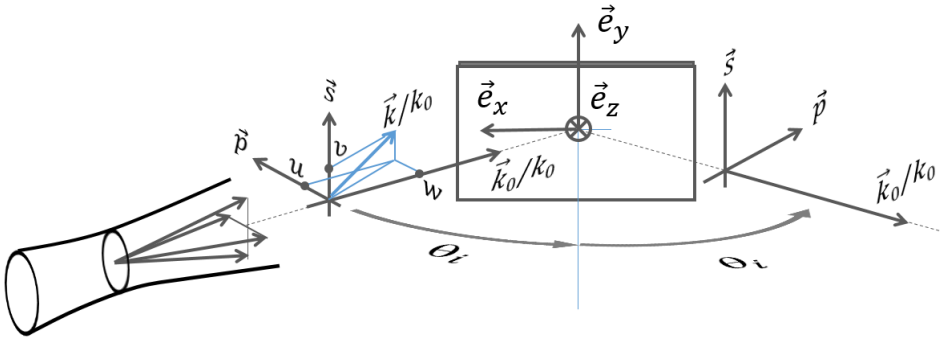

Figure 5.10: Geometry of beam reflection off a mirror. The incident beam has a Gaussian field distribution in the transverse plane. The transverse u, v and longitudinal w wavenumbers depend on the angle of incidence as explained in previous chapter.

We assume an incoming laser beam circularly polarized reflected off a metallic mirror (see Fig. 5.10). We express the result conveniently using the matrix formalism, already introduced in previous chapter. The resulting normalized

reflected field is expressed as follows:

$$\vec{E}_{Norm} = \exp\left(-\frac{x_0^2+y_0^2}{2\omega_f^2}\right)\bar{\bar{A}}_{\sigma_\pm}\bar{\bar{M}}_{Dx_0,y_0}\bar{\bar{P}}_{\sigma_\pm}\vec{E}_p \tag{5.4}$$

We recall that the mirror reflectivity matrix (including confocal Gaussian filtering) is given by equation (4.9):

$$\bar{\bar{M}}_{Dx_0,y_0} = \begin{bmatrix} r_p & 0 \\ 0 & r_s \end{bmatrix} + i\frac{x_0}{2l_f}\begin{bmatrix} r'_p & 0 \\ 0 & r'_s \end{bmatrix} + i\frac{y_0}{2l_f}\frac{r_p+r_s}{\tan\theta_i}\begin{bmatrix} 0 & -1 \\ 1 & 0 \end{bmatrix} \tag{5.5}$$

where $r'_{p/s} = \partial r_{p/s}/\partial\theta_i$ is the first order derivative of Fresnel coefficients with respect to the angle of incidence θ_i. The matrix of a circular polarizer/analyzer is given by (Appendix G):

$$\bar{\bar{P}}_{\sigma_\pm} = \bar{\bar{A}}_{\sigma_\pm} = \frac{1}{2}\begin{bmatrix} 1 & \mp i \\ \pm i & 1 \end{bmatrix} \tag{5.6}$$

Applying such a matrix on a linearly polarized field along $\vec{p}$ gives

$$\bar{\bar{P}}_{\sigma_\pm}\vec{E}_p = \frac{1}{\sqrt{2}}\frac{1}{\sqrt{2}}\begin{bmatrix} 1 & \mp i \\ \pm i & 1 \end{bmatrix}\begin{bmatrix} 1 \\ 0 \end{bmatrix} \tag{5.7}$$

which is also

$$\bar{\bar{P}}_{\sigma_\pm}\vec{E}_p = \frac{1}{\sqrt{2}}\frac{1}{\sqrt{2}}\begin{bmatrix} 1 \\ \pm i \end{bmatrix} \tag{5.8}$$

The matrix product above of linearly polarized field along $\vec{p}$ followed by a left or right circular polarizer produces $\vec{\sigma}_+$ or $\vec{\sigma}_-$ circularly polarized field. It is straightforward to verify that:

$$\vec{E}_{Norm} = \frac{1}{\sqrt{2}}\left(\frac{r_p+r_s}{\sqrt{2}} \pm \frac{y_0}{\sqrt{2}l_f}\frac{r_p+r_s}{\tan\theta_i} + i\frac{x_0}{\sqrt{2}l_f}\frac{(r_p+r_s)'}{2}\right)exp-\left(\frac{x_0^2+y_0^2}{2\omega_f^2}\right)\vec{\sigma}_\pm \tag{5.9}$$

where $r'_{p/s} = \partial r_{p/s}/\partial\theta_i$ is the first order derivative of Fresnel coefficients with respect to the angle of incidence θ_i. Therefore,

$$\vec{E}_{Norm} = \frac{r_p+r_s}{2}\left(1 \pm \frac{y_0}{l_f}\frac{1}{\tan\theta_i} + i\frac{x_0}{l_f}\frac{(r_p+r_s)'}{2(r_p+r_s)}\right)\exp\left(-\frac{x_0^2+y_0^2}{2\omega_f^2}\right)\vec{\sigma}_\pm \tag{5.10}$$

This is the detected field of a confocal scanning microscope in a circular polarization dark-field arrangement normalized to the bright-field value at confocal aperture placed at the origin. Equation (5.10) provides the general form of the confocal dark-field mapping of a Gaussian beam reflected off a material surface (dielectric or metallic). The assymetric modal distribution along y_0 is clearly affected by the chirality of the light polarization the focus of this chapter. The assymetric field distribution along x_0 is directly proportional to dispersion of

the reflectivity. We have not pushed the experimental investigation of this term in our work as we focused on metallic reflectivity for which this term is weak. In the case of the field distribution along the y-axis at $x_0 = 0$, the equation simplifies to

$$\vec{E}_{Norm,\sigma_\pm} = \frac{r_p + r_s}{2}\left(1 \pm \frac{y_0}{l_f}\frac{1}{\tan\theta_i}\right)\exp\left(-\frac{y_0^2}{2\omega_f^2}\right)\vec{\sigma}_\pm \tag{5.11}$$

or equivalently in terms of beam waist ω_f at focal plane of an objective of numerical aperture NA:

$$\vec{E}_{Norm,\sigma_\pm} = \frac{r_p + r_s}{2}\left(1 \pm \frac{y_0}{\omega_f}\frac{NA}{\tan\theta_i}\right)\exp\left(-\frac{y_0^2}{2\omega_f^2}\right)\vec{\sigma}_\pm \tag{5.12}$$

This field distribution expression now clearly process a spatial asymmetry along y_0, which flips with the sign of the polarization chirality. Equation (5.12) shows that the field has a destructive interference node at locations $y_{\sigma_\pm} = \mp tan\theta_i l_f$, which is also $\mp(\lambda tan\theta_i)/(\pi NA^2)$ assuming $\omega_f = \lambda/(\pi NA)$. This location is proportional to the Rayleigh length after confocal focusing of the spot. Practically for illustration at an incidence angle 45° and a waist radius about 3 times the wavelength, the location of field node will be at about 9 times the wavelength along y_0. Given the Gaussian nature of the beam, this node will be hardly visible in practical experimental conditions. However, already under condition of angles below 6° the location of the field node enters in the range of the beam waist. In such situation we expect to see significant departure from the fundamental Gaussian beam shapes. The detected intensity in a confocal scanning arrangement for circular polarization is:

$$I_{Norm,\sigma_\pm} = \frac{|\, r_p + r_s \,|^2}{4}\left(1 \pm \frac{y_0}{\omega_f}\frac{NA}{\tan\theta_i}\right)^2 \exp\left(-\frac{y_0^2}{\omega_f^2}\right) \tag{5.13}$$

For which we already see that beam center will displace above or below the plane of incidence depending on the helicity of the polarization. This equation can be expressed in reduced units on the out of plane axis $u_y = y_0/\omega_f$

$$I_{Norm,\sigma_\pm} = \frac{|\, r_p + r_s \,|^2}{4}\left(1 \pm \eta u_y\right)^2 \exp -u_y^2 \tag{5.14}$$

where the parameter $\eta = NA/\tan\theta_i$.
The maxima of the intensity are located at

$$\frac{y_{\sigma\pm}}{\omega_f} = \pm\frac{-1 \pm \sqrt{1 + 4\eta^2}}{2\eta} \tag{5.15}$$

for $\vec{\sigma}_+$ and $\vec{\sigma}_-$ circular polarization, respectively. In the limit of vanishing θ_i the maxima exhibits two lobes at locations independent from the chirality of

the circular polarization, namely at $\pm\omega_f$ independently of the sign of the polarization. In other words, the intensity has two maxima along a line perpendicular to the plane of incidence in a way identical to the case of p or s beam in cross-polarization. In the limit of $NA << tan\theta_i$, for instance for very wide Gaussian beam waist, the dominant maximum is located at $\pm NA/\tan\theta_i$ for the $\vec{\sigma}_+$ and $\vec{\sigma}_-$ circular polarization. We see therefore that the corresponding location $y_{\sigma_\pm} = \pm(\lambda/\pi)cot\theta_i$ as expected for a plane wave. In fact, in this limit of $NA << tan\theta_i$ this shift is independent from the Gaussian beam size. Thus, the expression $y_{\sigma_\pm} = \pm(\lambda/\pi)cot\theta_i$, which is also $\omega_f(NA/tan\theta_i)$ define the experimental condition for which the spin-orbit interaction of light can be made very clearly visible. The full measurements shown in Fig 5.11 are fitted using the formula of maxima of the intensity for a Gaussian beam (full line) and plane wave (dashed line) in units of beam waist radius ω_f. It shows first that the shift is always smaller than the beam waist. Nevertheless, it will still be many orders of magnitudes larger than in bright-field experiments without an analyzer. Worse still the bright-field experiment with a circular analyzer gives a 0 shift as expected from the conservation of angular momentum analysis. To illustrate the case, we consider $NA = 0.115$, taking an angle of incidence of 20° we will get a separation of beam position the order 63% of the beam radius when switching between a positive to a negative chirality of the circular polarization, as shown in Fig 5.11. Such a large visibility of the effect is unprecedented and is of text-book quality (see Fig 5.11).

θ_i	$y_{\sigma-}$	$y_{\sigma+}$	y/ω_f	$y_{planewave}$	$y_{Gaussian}$
44°	$-340 \pm 0.03nm$	$+330 \pm 0.03nm$	± 0.117	$\pm 298nm$	$\pm 294nm$
30°	$-500 \pm 0.02nm$	$+520 \pm 0.03nm$	± 0.191	$\pm 498nm$	$\pm 480nm$
21°	$-710 \pm 0.01nm$	$+710 \pm 0.02nm$	± 0.27	$\pm 750nm$	$\pm 693nm$
13°	$-1050 \pm 0.02nm$	$+1040 \pm 0.02nm$	± 0.413	$\pm 1.24\mu m$	$\pm 1.03\mu m$

Table 5.3: Overview of the measured Imbert-Fedorov shift for different incidence angles $\theta_i = 44°, 30°, 21°, 13°$. For each θ_i angle setting, we measure the Imbert-Fedorov shift for σ_+ and σ_- circular polarization. $\Delta y_{measured} = y_{\sigma+} - y_{\sigma-}$ corresponds to the total displacement of the opposite shifts of the two circular polarizations. The theoretical value of $\Delta y_{planewave} = 2 \times (\lambda/\pi)cot\theta_i$ is determined for $\lambda = 905nm$ as explained in text (see section 5.2 for details).

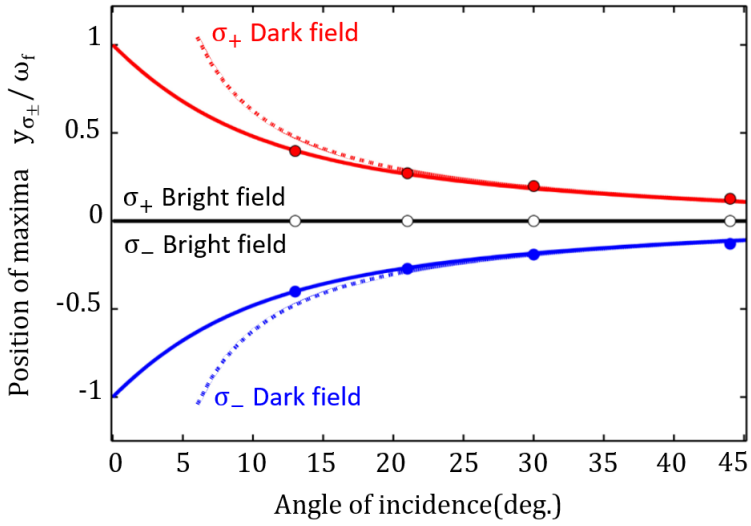

Figure 5.11: Measured Imbert-Fedorov shift for $\sigma_\pm$ circular polarization in unit of beam waist radius ω_f in case of silver mirror and for a laser wavelength $\lambda = 905nm$. We plot the position of intensity maxima for a plane wave (dashed line) and Gaussian beam (full line) reflected off a silver mirror as a function of polarization excitation and detection. $\sigma_\pm$ Dark-field and $\sigma_\pm$ Bright-field denote the dark-field ($\sigma_\pm M \sigma_\pm$) and bright-field ($\sigma_\pm M \sigma_\mp$) configurations respectively, when the mirror (M) is sandwiched between two circular polarizers. The data measured at $\theta_i = 13°$ shows clearly the departure from the plane wave approximation divergence (dashed line) for low angles of incidence. The Gaussian beam model is in a very good agreement (full line).

5.6 Imbert-Fedorov shift without the use of polarization analyzer

The "original" Imbert-Fedorov shift, namely circularly polarized reflected Gaussian beam without the use of polarization analyzer configuration the field distribution in a confocal arrangement is given by removing the analyzer function in equation (4.10)

$$\vec{E}_{Norm}(x_0, y_0) = \bar{\bar{M}}_{Dx_0,y_0} \bar{\bar{P}}_{\sigma_\pm} \vec{E}_p \tag{5.16}$$

where $\bar{\bar{P}}_{\sigma_\pm}$ is the Jones matrix of a circular polarizer (see Appendix G). We recall that the mirror reflectivity matrix (including confocal Gaussian filtering) is given by equation (4.9):

$$\bar{\bar{M}}_{Dx_0,y_0} = \begin{bmatrix} r_p & 0 \\ 0 & r_s \end{bmatrix} + i\frac{x_0}{2l_f}\begin{bmatrix} r'_p & 0 \\ 0 & r'_s \end{bmatrix} + i\frac{y_0}{2l_f}\frac{r_p + r_s}{\tan\theta_i}\begin{bmatrix} 0 & -1 \\ 1 & 0 \end{bmatrix} \tag{5.17}$$

The job to be done in this configuration is to evaluate the $\bar{\bar{M}}_1\ \bar{\bar{P}}_{\sigma_\pm}\vec{E}_p$, $\bar{\bar{M}}_2\ \bar{\bar{P}}_{\sigma_\pm}\vec{E}_p$ and $\bar{\bar{M}}_3\ \bar{\bar{P}}_{\sigma_\pm}\vec{E}_p$. Where

$$\bar{\bar{M}}_1 \bar{\bar{P}}_{\sigma_\pm} \vec{E}_p = \frac{1}{\sqrt{2}} \frac{1}{\sqrt{2}} \begin{bmatrix} r_p & 0 \\ 0 & r_s \end{bmatrix} \begin{bmatrix} 1 & \mp i \\ \pm i & 1 \end{bmatrix} \begin{bmatrix} 1 \\ 0 \end{bmatrix} \tag{5.18}$$

this

$$\bar{\bar{M}}_1 \bar{\bar{P}}_{\sigma_\pm} \vec{E}_p = \frac{1}{\sqrt{2}} \frac{1}{\sqrt{2}} \begin{bmatrix} r_p \\ \pm i r_s \end{bmatrix} \tag{5.19}$$

Moving to the next term gives a very similar calculation

$$\bar{\bar{M}}_2 \bar{\bar{P}}_{\sigma_\pm} \vec{E}_p = i \frac{x_0}{2 l_f} \frac{1}{\sqrt{2}} \frac{1}{\sqrt{2}} \frac{\partial}{\partial \theta_i} \begin{bmatrix} r_p \\ \pm i r_s \end{bmatrix} \tag{5.20}$$

The last term involves an anti-diagonal matrix

$$\bar{\bar{M}}_3 \bar{\bar{P}}_{\sigma_\pm} \vec{E}_p = i \frac{y_0}{2 l_f} \frac{r_p + r_s}{\tan \theta_i} \frac{1}{\sqrt{2}} \frac{1}{\sqrt{2}} \begin{bmatrix} 0 & -1 \\ 1 & 0 \end{bmatrix} \begin{bmatrix} 1 & \mp i \\ \pm i & 1 \end{bmatrix} \begin{bmatrix} 1 \\ 0 \end{bmatrix} \tag{5.21}$$

this

$$\bar{\bar{M}}_3 \bar{\bar{P}}_{\sigma_\pm} \vec{E}_p = i \frac{y_0}{2 l_f} \frac{r_p + r_s}{\tan \theta_i} \frac{1}{\sqrt{2}} \frac{1}{\sqrt{2}} \begin{bmatrix} 0 & -1 \\ 1 & 0 \end{bmatrix} \begin{bmatrix} 1 \\ \pm i \end{bmatrix} \tag{5.22}$$

The next term is

$$\bar{\bar{M}}_3 \bar{\bar{P}}_{\sigma_\pm} \vec{E}_p = i \frac{y_0}{2 l_f} \frac{r_p + r_s}{\tan \theta_i} \frac{1}{\sqrt{2}} \frac{1}{\sqrt{2}} \begin{bmatrix} \mp i \\ 1 \end{bmatrix} \tag{5.23}$$

Giving

$$\bar{\bar{M}}_3 \bar{\bar{P}}_{\sigma_\pm} \vec{E}_p = \pm \frac{y_0}{2 l_f} \frac{r_p + r_s}{\tan \theta_i} \frac{1}{\sqrt{2}} \frac{1}{\sqrt{2}} \begin{bmatrix} 1 \\ \pm i \end{bmatrix} \tag{5.24}$$

Now putting all terms together, we get

$$\vec{E}_{Norm} = \frac{1}{2} \exp\left(- \frac{x_0^2 + y_0^2}{2 \omega_f^2} \right) \begin{bmatrix} r_p + i \frac{x_0}{2 l_f} \frac{\partial r_p}{\partial \theta_i} \pm \frac{y_0}{2 l_f} \frac{r_p + r_s}{\tan \theta_i} \\ \pm i \left(r_s + i \frac{x_0}{2 l_f} \frac{\partial r_s}{\partial \theta_i} \pm \frac{y_0}{2 l_f} \frac{r_p + r_s}{\tan \theta_i} \right) \end{bmatrix} \tag{5.25}$$

Case $x_0 = 0$

$$\vec{E}_{Norm} = \frac{1}{2} \exp\left(- \frac{x_0^2 + y_0^2}{2 \omega_f^2} \right) \begin{bmatrix} r_p \pm \frac{y_0}{2 l_f} \frac{r_p + r_s}{\tan \theta_i} \\ \pm i \left(r_s \pm \frac{y_0}{2 l_f} \frac{r_p + r_s}{\tan \theta_i} \right) \end{bmatrix} \tag{5.26}$$

The corresponding intensity is

$$I_{Norm} = \frac{1}{4}\exp\Big(-\frac{y_0^2}{\omega_f^2}\Big)\Big(\mid r_p \mid^2 + \mid r_s \mid^2 + 2\Big|\frac{y_0}{2l_f}\frac{r_p + r_s}{\tan\theta_i}\Big|^2 + 2\frac{y_0}{2l_f}\frac{|r_p + r_s|^2}{\tan\theta_i}\Big) \tag{5.27}$$

Compare this to the case with a circular analyzer in dark-field (see equation (5.10))

$$I_{Norm,\sigma_\pm} = \frac{\mid r_p + r_s \mid^2}{4}\exp\Big(-\frac{y_0^2}{\omega_f^2}\Big)\Big(1 \pm \frac{y_0}{l_f}\frac{1}{\tan\theta_i}\Big)^2 \tag{5.28}$$

which is also

$$I_{Norm,\sigma_\pm} = \frac{\mid r_p + r_s \mid^2}{4}\exp\Big(-\frac{y_0^2}{\omega_f^2}\Big)\Big(1 + |\frac{y_0}{l_f}\frac{1}{\tan\theta_i}|^2 \pm 2\frac{y_0}{l_f}\frac{1}{\tan\theta_i}\Big) \tag{5.29}$$

Both equations for the case with and without an analyzer show a similar analytical expression. This said, clearly, the weight of the polarization chirality dependent terms (i.e linear in y_0) in the measurement without analyzer is reduced by a factor $|r_p + r_s|^2/4$. So in limit in which the quadratic term in y_0 does not dominate the line shape (i.e away from vanishing angle of incidence), we can directly deduce the Imbert-Fedorov shift from our previous calculation for the dark-field case (see section 5.5) for the positive and the negative circular polarization.
We see therefore that the corresponding locations are given by:

$$y_{max\pm} \approx \pm\frac{\mid r_p + r_s \mid^2}{4}\frac{\lambda}{\pi\tan\theta_i} \tag{5.30}$$

Very much like in the dark-field confocal configuration (section 5.5), the shift is independent from the size of the beam. The notable difference is that now the shift depends on the material optical properties through $|r_p + r_s|^2$. For silver the calculated pure Imbert-Fedorov shift is shown in the table 5.4. This is to be compared to the dark-field measurement in circular polarization.

Note the connection to the extinction ratio $|r_p + r_s|^2/4 = 1/(ER)$ which shows that in the dark-field configuration the Imbert-Fedorov shift is amplified by ER. The question remains to demonstrate formally whether or not this "amplification" of the shift obtained by sorting out the photons not experiencing spin-orbit interaction is the same as the one found from the general frame work of the weak-measurement technique [42]. The fact that the amplification factor is directly given by the extinction ratio is a strong indication that the principle of weak measurement is not applying to this case. This said, the special situation of dark-field measurement for the very particular case of circular polarization

θ_i	$y_{max\pm}$ without analyzer	$y_{\sigma\pm}$ in dark-field
44°	$3.20nm$	$335nm$
30°	$1.01nm$	$510nm$
21°	$0.035nm$	$710nm$
13°	$0.08nm$	$1.045nm$

Table 5.4: Overview of the Imbert-Fedorov shift for different incidence angles $\theta_i = 44°, 30°, 21°, 13°$ without analyzer and in dark-field configuration. For each θ_i incidence, the shift is calculated for σ_+ and σ_- circular polarization at $\lambda = 905nm$ as explained in text.

(and away from the low angle limit) is that the Imbert-Fedorov shift does not depend on the material property but solely on the photon polarization chirality properties, its wavelength and its angle of incidence. This is not the case for any other polarization state. It is very interesting to note that for this very pure circular polarization configuration, the shift is free from the arbitrariness inherent to the weak measurement technique, namely that the amplification factor can be in principle set to any arbitrary value. We verified indeed that away from a pure circular polarization state of the polarizer and analyzer we could measure a massive amplification that we could simply set by choosing the degree of ellipticity of our polarization.

5.7 Remark

Literature about spin-Hall effect of light has tended to confirm that a simple mirror reflectivity splits a linearly polarized Gaussian beam into left and right circularly polarized beams [42]. Such unjustified postulation can lead to serious questions regarding the nature of the polarization state of the Imbert-Fedorov modes observed previously in this work for a linearly polarized beam. In this context, we now assume that we manage to make an experiment that bring the fields $\vec{E}_{Norm,\sigma_\pm}$ (section 5.5) to add or substract interferometrically. This experiment requires splitting the incoming beam in two parallel fields of two opposing circular polarization, each beam then is reflected and passes two individual circular polarization analyzers of same chirality of the corresponding impinging beam. Finally both beams need to be combined on a detector. A rather complex procedure but let us see what would be the result. In this case we make use of the linear combination of fields

$$\vec{p} = \frac{(\vec{\sigma}_+ + \vec{\sigma}_-)}{\sqrt{2}} \tag{5.31}$$

$$\vec{s} = -i\frac{(\vec{\sigma}_+ - \vec{\sigma}_-)}{\sqrt{2}} \tag{5.32}$$

We recall that:

$$\vec{E}_{Norm,\sigma_\pm} = \frac{r_p + r_s}{\sqrt{2}}\left(1 \pm \frac{y_0}{l_f}\frac{1}{\tan\theta_i}\right)\exp -\left(\frac{y_0^2}{2\omega_f^2}\right)\vec{\sigma}_\pm \tag{5.33}$$

We see that if we just added or subtracted the fields

$$\frac{\vec{E}_{Norm,\sigma_+} + \vec{E}_{Norm,\sigma_-}}{\sqrt{2}} = \frac{r_p + r_s}{2}\exp\left(-\frac{x_0^2 + y_0^2}{2\omega_f^2}\right)\left(\frac{\vec{\sigma}_+ + \vec{\sigma}_-}{\sqrt{2}} + \frac{y_0}{l_f}\frac{1}{\tan\theta_i}\frac{\vec{\sigma}_+ - \vec{\sigma}_-}{\sqrt{2}}\right) \tag{5.34}$$

Like wise

$$\frac{\vec{E}_{Norm,\sigma_+} - \vec{E}_{Norm,\sigma_-}}{\sqrt{2}} = \frac{r_p + r_s}{2}\exp\left(-\frac{x_0^2 + y_0^2}{2\omega_f^2}\right)\left(\frac{\vec{\sigma}_+ - \vec{\sigma}_-}{\sqrt{2}} + \frac{y_0}{l_f}\frac{1}{\tan\theta_i}\frac{\vec{\sigma}_+ + \vec{\sigma}_-}{\sqrt{2}}\right) \tag{5.35}$$

Now we conveniently express both fields in terms of $\vec{p}$ and $\vec{s}$

$$\frac{\vec{E}_{Norm,\sigma_+} + \vec{E}_{Norm,\sigma_-}}{\sqrt{2}} = \frac{r_p + r_s}{2}\exp\left(-\frac{x_0^2 + y_0^2}{2\omega_f^2}\right)\left(\vec{p} + i\frac{y_0}{l_f}\frac{1}{\tan\theta_i}\vec{s}\right) \tag{5.36}$$

and

$$\frac{\vec{E}_{Norm,\sigma_+} - \vec{E}_{Norm,\sigma_-}}{\sqrt{2}} = \frac{r_p + r_s}{2}\exp\left(-\frac{x_0^2 + y_0^2}{2\omega_f^2}\right)\left(i\vec{s} + \frac{y_0}{l_f}\frac{1}{\tan\theta_i}\vec{p}\right) \tag{5.37}$$

We see clearly that any linear combination of this form will not allow to have a cancellation of intensity on axis at $y_0 = 0$. More generally, any linear combination $a\vec{E}_{Norm,\sigma_+} + b\vec{E}_{Norm,\sigma_-}$ adding the fields (even with complex coefficients) terms will not lead to a cancellation of the intensity at $y_0 = 0$. To get a cancellation of the field at $y_0 = 0$, we need instead to pass the combined fields through a linear crossed polarizers that ends up keeping just the terms in y_0. In this very complicated configuration, we recover the results obtained simply using a pair of linear polarizer and analyzer. The message here is to tell that summing up the fields do not lead to a pure linearly polarized beam.

5.8 Conclusion

In conclusion we presented a novel method to measure and map the Imbert-Fedorov shift based on a dark-field cross-polarization technique in a confocal arrangement. In our proposed dark-field configuration under circular polarization, the majority photons reflected off a surface that are not contributing to the shift are filtered-out. The minority photons possess the proper chirality for spin-orbit coupling of light enabling this way the magnification of the Imbert-Fedorov shift by several orders of magnitudes. We verified that the out of plane of incidence shift measured this way is a direct consequence of the conservation of total angular momentum. Building on our detailed model for Gaussian laser beams derived for the first part of this work we have verified quantitatively experimentally that the shift increases significantly when decreasing the angle of incidence, this, to the best of our knowledge, is a novel regime that was not explored previously. The analytical model show an excellent agreement with our measurements performed on a silver mirror. In particular, the model reveals clearly a regime of lower angle of incidence below which the simplistic approach of quasi plane wave would lead to an unphysical divergence of the shift at vanishing angles. In such a low angle regime, our model eliminates this shift divergence and predicts instead a modal transformation of the reflected minority photons to the next higher Hermite-Gaussian modes in a way very similar to that explored in the first part of this work. First data indicate the transition into such a regime.

Chapter 6

Summary and perspectives

Our study provides a robust toolbox for a new way to do fluorescence spectroscopy and polarimetry experiments using confocal microscopy. We have exposed a systematic experimental method based on a confocal microscopy arrangement to obtain a giant enhancement in dark-field cross-polarization extinction and this by up to 3 orders of magnitudes and possibly beyond. We found that the effect exploits the material properties of a surface or interface under condition of total internal reflectivity in particular. In more general terms, the effect was found to be fully governed by the phase difference, such as induced by beam-splitter cubes and Bragg mirrors, between the reflectivity of light components polarized in and out of plane of incidence. Now that the basic principle of cancellation of polarization leakage is established, there are options for improving the experimental detection limit of the cross-polarization extinction ratio. First it is possible to improve the signal-to-noise ratio. Generally, it is helpful to increase the optical input power by better alignment. However, this depends primarily on the application. In some cases, noisy lasers can't be stabilized and a suitable type and model of photo-detector can (and cannot) improve the signal-to-noise ratio. Second possibility is to amplify the rotation-angle precision. It is demonstrated in chapter 4 that a positioning resolution of 10^{-6} degrees allows measuring an extinction ratio value in the level of 10^{11} and beyond. It is practically possible to obtain a sub-step-size rotation resolution with selected attocube controllers. An already existing solution is the bearing based rotator ECR4040/Al/NUM/RT with an integrated 1/2" aperture, suitable for optical experiments. It is designed for ambient conditions with a fine angular position of $0.04m°$.

Furthermore, we have also presented the theoretical modal analysis of beam reflectivity. In fact, modeling this effect led us to simulate and map in minute details the transformation of Gaussian beams near cross-polarization into Imbert-Fedorov higher modes, a physics governed essentially by the finite divergence of a Gaussian beam reflecting off a surface. Results so far have been very promising up to first order transformation in x and y. One potential promising application of our approach would be to simulate and map the transformation of Gaussian beams at higher order modes. So far we did not observe any trace of the mode

TEM_{11} signal. There is no doubt however that this mode is present as measured in [43], this is why we believe that our model is not complete yet. Future work should also concentrate on enhancing the quality of the extinction ratio in a real-world confocal device made of several mirrors and beam-splitter cubes in different and complex geometries. We are confident that our model will serve as a base for setting up the basic building block of any future optical spectroscopy system. The present model is based on a pure Maxwell plane wave expansion approach. The next step is to include the connection between the Imbert-Fedorov effect and geometric phases. This is absolutely essential in the conception and design of modern spin-based optical devices.

In chapter 5, we have presented a direct observation of the Imbert-Fedorov shift i.e spin-Hall effect for spin up and down of light (circular polarization). This was never seen clearly in a text book. We have demonstrated that the Imbert-Fedorov like it is said in text books that (i) a laser beam shifts out of the plane of specular incidence when the light is impinging in a circular polarization and detected in the same circular polarization. (ii) The sign of the shift is given by the chirality. This is a new finding in microscopy and can lead to some measurement issues or opportunities for researcher doing measurements under circular polarization. We showed both theoretically and experimentally, that the effect is a consequence of conservation of total angular momentum between the incident and reflected beam. To be convincing, we have also verified the maxima beam position stability of our setup. The idealized situation of a circular polarized plane wave light and a highly reflective perfect mirror is perfectly predictive, namely it predicts a displacement shift typically dependent on the co-tangent of incidence angle $cot\theta_i$. This beautiful result comes from a very simple calculation that consider the conservation of angular momentum of light projected on the z-axis perpendicular to the mirror. In this work and in real-life microscopy experiments we ask ourselves how does that apply to a Gaussian focused beam in a confocal configuration. To answer this we have made our model calculations first in the limit of smaller NA and found the exact same result for the shift of location of the maximum of the beam intensity. So we now have a regime for which a Gaussian mode appear to act like a plane wave. We verify our theory by experimental measurements at difference incidence angles. Our experimental approach has a number of similarities with the weak measurement technique, the main difference is that we measure at exact cross-polarization condition. Further experimental investigations are needed to understand the origin of the weak measurement amplification of the shift already reported in literature [42, 48]. This is an important matter for future research.

This work opens the way to methodical design of sensitive laser resonant fluorescence microscopes with extreme background extinction, for a broad range of applications in quantum optics and solid-state physics. The new methods developed for this work can also be applied for measuring material optical properties and polarimetry applications.

Appendix A

Supplementary information to chapter 3 "The physical origins of cancellation of polarization leakage"

The purpose of this section is to derive an expression for the cross-polarization extinction amplification in a confocal arrangement. For this purpose, we assume an incoming laser field $\vec{E}_p$ initially p-polarized that we rotate at an angle β aligning it with the polarizer such $\vec{E}(\beta) = \bar{\bar{R}}(\beta)\vec{E}_p$. This field first traverses the leaky polarizer also rotated at β such $\bar{\bar{P}}(\beta) = \bar{\bar{R}}(\beta)\ \bar{\bar{L}}\bar{\bar{P}}_{p_0}\ \bar{\bar{R}}(-\beta)$ followed by the mirror matrix $\bar{\bar{M}}$ and by the analyzer matrix rotated at an angle α namely $\bar{\bar{A}}(\alpha) = \bar{\bar{R}}(\alpha)\ \bar{\bar{L}}\bar{\bar{A}}_{p_0}\ \bar{\bar{R}}(-\alpha)$ so the field $\vec{E}$ just after the analyzer writes

$$\vec{E} = \bar{\bar{A}}(\alpha)\bar{\bar{M}}\bar{\bar{P}}(\beta)\bar{\bar{R}}(\beta)\vec{E}_p \tag{A.1}$$

A.1 Jones calculus

To calculate equation (A.1), we start first by performing a simple matrix multiplication of the Jones matrix of the input laser field together with the polarizer at an angle β. We find that

$$\bar{\bar{P}}(\beta)\bar{\bar{R}}(\beta)\vec{E}_p = \bar{\bar{R}}(\beta)\ \bar{\bar{L}}\bar{\bar{P}}_{p_0}\ \bar{\bar{R}}(-\beta)\bar{\bar{R}}(\beta)\vec{E}_p \tag{A.2}$$

Here the product $\bar{\bar{R}}(-\beta)\bar{\bar{R}}(\beta)$ is equal to identity matrix. Thus, we can write

$$\Leftrightarrow \bar{\bar{P}}(\beta)\bar{\bar{R}}(\beta)\vec{E}_p = \bar{\bar{R}}(\beta)\ \bar{\bar{L}}\bar{\bar{P}}_{p_0}\ \vec{E}_p$$

We recall that the incoming laser field $\vec{E}_p$ is initially p-polarized i.e $\vec{E}_p = \begin{bmatrix} 1 \\ 0 \end{bmatrix}$, $\bar{\bar{L}}\bar{\bar{P}}_{p_0} = \begin{bmatrix} a & 0 \\ -ib & 0 \end{bmatrix}$ and $\bar{\bar{R}}(\beta) = \begin{bmatrix} \cos\beta & -\sin\beta \\ \sin\beta & \cos\beta \end{bmatrix}$. Therefore,

$$\Leftrightarrow \bar{\bar{P}}(\beta)\bar{\bar{R}}(\beta)\vec{E}_p = \begin{bmatrix} \cos\beta & -\sin\beta \\ \sin\beta & \cos\beta \end{bmatrix} \begin{bmatrix} a & 0 \\ -ib & 0 \end{bmatrix} \begin{bmatrix} 1 \\ 0 \end{bmatrix}$$

Now we calculate the matrix product

$$\Leftrightarrow \bar{\bar{P}}(\beta)\bar{\bar{R}}(\beta)\vec{E}_p = \begin{bmatrix} \cos\beta & -\sin\beta \\ \sin\beta & \cos\beta \end{bmatrix} \begin{bmatrix} a \\ -ib \end{bmatrix}$$

which is also

$$\Leftrightarrow \bar{\bar{P}}(\beta)\bar{\bar{R}}(\beta)\vec{E}_p = \begin{bmatrix} a\cos\beta + ib\sin\beta \\ a\sin\beta - ib\cos\beta \end{bmatrix} \tag{A.3}$$

For a high quality commercially available polarizers $a^2 >> b^2$. Thus $a^2 \approx 1$ and the leakage b^2 is in the range of 10^5 and 10^6 in best cases. A practical check for p- polarized light, namely $\beta = 0$ leads to the expected field vector $[1, ib]$ at the output of a leaky polarizer along $\vec{p}$.
Now, let's calculate the matrix of a leaky analyzer rotated at α defined as:

$$\bar{\bar{A}}(\alpha) = \bar{\bar{R}}(\alpha)\ \bar{\bar{L}}\bar{\bar{A}}_{p_0}\ \bar{\bar{R}}(-\alpha) \tag{A.4}$$

Using $\bar{\bar{L}}\bar{\bar{A}}_{p_0} = \bar{\bar{L}}\bar{\bar{P}}_{p_0} = \begin{bmatrix} a & 0 \\ -ib & 0 \end{bmatrix}$ and $\bar{\bar{R}}(\alpha) = \begin{bmatrix} \cos\alpha & -\sin\alpha \\ \sin\alpha & \cos\alpha \end{bmatrix}$, we can write that

$$\bar{\bar{A}}(\alpha) = \begin{bmatrix} \cos\alpha & -\sin\alpha \\ \sin\alpha & \cos\alpha \end{bmatrix} \begin{bmatrix} a & 0 \\ -ib & 0 \end{bmatrix} \begin{bmatrix} \cos\alpha & \sin\alpha \\ -\sin\alpha & \cos\alpha \end{bmatrix} \tag{A.5}$$

Here, the matrix product calculation leads to

$$\Leftrightarrow \bar{\bar{A}}(\alpha) = \begin{bmatrix} \cos\alpha & -\sin\alpha \\ \sin\alpha & \cos\alpha \end{bmatrix} \begin{bmatrix} a\cos\alpha & a\sin\alpha \\ -ib\cos\alpha & -ib\sin\alpha \end{bmatrix}$$

So after simplifying, this expression becomes:

$$\Leftrightarrow \bar{\bar{A}}(\alpha) = \begin{bmatrix} a\cos^2\alpha + ib\cos\alpha\sin\alpha & a\cos\alpha\sin\alpha + ib\sin^2\alpha \\ a\cos\alpha\sin\alpha - ib\cos^2\alpha & a\sin^2\alpha - ib\cos\alpha\sin\alpha \end{bmatrix} \tag{A.6}$$

which can be also written as:

$$\Leftrightarrow \bar{\bar{A}}(\alpha) = \begin{bmatrix} a & ib \\ -ib & a \end{bmatrix} \begin{bmatrix} \cos^2\alpha & \cos\alpha\sin\alpha \\ \cos\alpha\sin\alpha & \sin^2\alpha \end{bmatrix} \tag{A.7}$$

From equation (A.7), we note that the matrix of a real physical linear analyzer is none than a combination of an ideal linear polarizer at an angle α and the leakage Jones matrix $\bar{\bar{L}}$.

A.2 Expression of the electric field after the analyzer (equation (3.4))

We introduce Eq. (A.3) and Eq. (A.7) into Eq. (A.1) , the electric field after the analyzer can be therefore written as

$$\vec{E} = \bar{\bar{A}}(\alpha)\bar{\bar{M}}\bar{\bar{P}}(\beta)\bar{\bar{R}}(\beta)\vec{E}_p \tag{A.8}$$

By inserting equation (A.7) and equation (A.3) into equation (A.8), we obtain

$$\vec{E} = \begin{bmatrix} a & ib \\ -ib & a \end{bmatrix}\begin{bmatrix} \cos^2\alpha & \cos\alpha\sin\alpha \\ \cos\alpha\sin\alpha & \sin^2\alpha \end{bmatrix}\begin{bmatrix} r_p & 0 \\ 0 & r_s \end{bmatrix}\begin{bmatrix} a\cos\beta + ib\sin\beta \\ a\sin\beta - ib\cos\beta \end{bmatrix}$$

The matrix product calculation leads to

$$\vec{E} = \begin{bmatrix} a & ib \\ -ib & a \end{bmatrix}\begin{bmatrix} \cos^2\alpha & \cos\alpha\sin\alpha \\ \cos\alpha\sin\alpha & \sin^2\alpha \end{bmatrix}\begin{bmatrix} r_p(a\cos\beta + ib\sin\beta) \\ r_s(a\sin\beta - ib\cos\beta) \end{bmatrix}$$

which is also

$$\vec{E} = \begin{bmatrix} a & ib \\ -ib & a \end{bmatrix}\begin{bmatrix} r_p(a\cos\beta + ib\sin\beta)\cos^2\alpha + r_s(a\sin\beta - ib\cos\beta)\cos\alpha\sin\alpha \\ r_p(a\cos\beta + ib\sin\beta)\cos\alpha\sin\alpha + r_s(a\sin\beta - ib\cos\beta)\sin^2\alpha \end{bmatrix}$$

So after simplifying, this expression becomes:

$$\vec{E} = \left\{r_p(a\cos\beta + ib\sin\beta)\cos\alpha + r_s(a\sin\beta - ib\cos\beta)\sin\alpha\right\}\begin{bmatrix} a & ib \\ -ib & a \end{bmatrix}\begin{bmatrix} \cos\alpha \\ \sin\alpha \end{bmatrix}$$

Finally,

$$\vec{E} = \left\{r_p(a\cos\beta + ib\sin\beta)\cos\alpha + r_s(a\sin\beta - ib\cos\beta)\sin\alpha\right\}\begin{bmatrix} a\cos\alpha + ib\sin\alpha \\ -ib\cos\alpha + a\sin\alpha \end{bmatrix} \tag{A.9}$$

A.3 Expression of the light intensity after the analyzer (equation (3.6))

The corresponding intensity is determined by $I = |\vec{E}|^2$, which is also

$$I = \left|r_p(a\cos\beta + ib\sin\beta)\cos\alpha + r_s(a\sin\beta - ib\cos\beta)\sin\alpha\right|^2 \tag{A.10}$$

with $|a\cos\alpha + ib\sin\alpha|^2 + |-ib\cos\alpha + a\sin\alpha|^2 = a^2 + b^2 = 1$. Equation (A.10) reads

$$I = \left|ar_p\cos\beta\cos\alpha + ar_s\sin\beta\sin\alpha + ibr_p\sin\beta\cos\alpha - ibr_s\cos\beta\sin\alpha\right|^2 \tag{A.11}$$

We calculate the product of the electric field after the analyzer and its complex conjugate, we obtain

$$I = a^2 \mid r_p \cos\beta\cos\alpha + r_s \sin\beta\sin\alpha \mid^2 + b^2 \mid r_p \sin\beta\cos\alpha - r_s \cos\beta\sin\alpha \mid^2 + K_1 + K_2$$

where

$$K_1 = \Big(ar_p \cos\beta\cos\alpha + ar_s \sin\beta\sin\alpha\Big)\Big(ibr_p \sin\beta\cos\alpha - ibr_s \cos\beta\sin\alpha\Big)^*$$

or

$$K_1 = -iabr_p r_p^* \cos\beta\sin\beta\cos^2\alpha - iabr_s r_p^* \sin^2\beta\sin\alpha\cos\alpha + iabr_p r_s^* \cos^2\beta\sin\alpha\cos\alpha + iabr_s r_s^* \cos^2\beta\sin^2\alpha$$

and

$$K_2 = \Big(ar_p \cos\beta\cos\alpha + ar_s \sin\beta\sin\alpha\Big)^*\Big(ibr_p \sin\beta\cos\alpha - ibr_s \cos\beta\sin\alpha\Big)$$

or

$$K_2 = iabr_p r_p^* \cos^2\beta\cos^2\alpha + iabr_s^* r_p \sin^2\beta\sin\alpha\cos\alpha - iabr_p^* r_s \cos^2\beta\sin\alpha\cos\alpha - iabr_s r_s^* \cos^2\beta\sin^2\alpha$$

We calculate the sum $K_1 + K_2$, we obtain

$$K_1 + K_2 = iabr_p r_s^* \cos\alpha\sin\alpha - iabr_s r_p^* \cos\alpha\sin\alpha = iab\cos\alpha\sin\alpha(r_p r_s^* - r_s r_p^*)$$

which is also

$$K_1 + K_2 = -2abIm(r_p r_s^*)\cos\alpha\sin\alpha \tag{A.12}$$

Inserting K_1 and K_2 into equation (A.11) leads to

$$I = a^2 \mid r_p \cos\beta\cos\alpha + r_s \sin\beta\sin\alpha \mid^2 + b^2 \mid r_p \sin\beta\cos\alpha - r_s \cos\beta\sin\alpha \mid^2 - 2abIm(r_p r_s^*)\cos\alpha\sin\alpha \tag{A.13}$$

A.4 Angular shift as a function of Fresnel reflection coefficients

To get a better feel for the relevant parameters in canceling almost perfectly the polarization leakage we use the form $r_p = \rho_p\ exp(i\varphi_p)$ and $r_s = \rho_s\ exp(i\varphi_s)$ that can be conveniently symmetrized using $\rho_s = \rho + \delta\rho/2$, $\rho_p = \rho - \delta\rho/2$ for the reflectivity and $\Delta = (\varphi_p - \varphi_s)/2$ the phase difference. This way we obtain

$$\bar{\bar{M}} = \begin{bmatrix} r_p & 0 \\ 0 & r_s \end{bmatrix} = e^{-i\Delta}\begin{bmatrix} (\rho - \delta\rho/2)e^{i\Delta} & 0 \\ 0 & (\rho + \delta\rho/2)e^{-i\Delta} \end{bmatrix} \tag{A.14}$$

For high reflectivity mirrors $\rho_p \approx \rho_s \approx 1$ and $\delta\rho = 0$

$$\bar{\bar{M}} \approx \begin{bmatrix} e^{i\Delta} & 0 \\ 0 & e^{-i\Delta} \end{bmatrix} \tag{A.15}$$

Thus, the Fresnel reflection coefficients can be approximated by $r_p \approx e^{i\Delta}$ and $r_s \approx e^{-i\Delta}$.
We recall that the light intensity just after the analyzer is given by equation (A.10):

$$I = \mid r_p(a\cos\beta + ib\sin\beta)\cos\alpha + r_s(a\sin\beta - ib\cos\beta)\sin\alpha \mid^2$$

Inserting r_p and r_s into the expression of the intensity

$$I = \mid e^{i\Delta}(a\cos\beta + ib\sin\beta)\cos\alpha + e^{-i\Delta}(a\sin\beta - ib\cos\beta)\sin\alpha \mid^2 \tag{A.16}$$

In case of a perfect leakage cancellation, i.e $I = 0$

$$I = 0 \Leftrightarrow \mid e^{i\Delta}(a\cos\beta + ib\sin\beta)\cos\alpha + e^{-i\Delta}(a\sin\beta - ib\cos\beta)\sin\alpha \mid^2 = 0$$

This means that the real and the imaginary parts of I are both equal to 0 and we obtain a set of two equations

$$\begin{cases} a\cos\beta\cos\alpha\cos\Delta - b\sin\beta\cos\alpha\sin\Delta + a\sin\beta\sin\alpha\cos\Delta - b\cos\beta\sin\alpha\sin\Delta = 0 \\ a\cos\beta\cos\alpha\sin\Delta + b\sin\beta\cos\alpha\cos\Delta - a\sin\beta\sin\alpha\sin\Delta - b\cos\beta\sin\alpha\cos\Delta = 0 \end{cases} \tag{A.17}$$

Using the identities $\cos(\alpha \mp \beta) = \cos\alpha\cos\beta \pm \sin\alpha\sin\beta$ and $\sin(\alpha \mp \beta) = \sin\alpha\cos\beta \mp \cos\alpha\sin\beta$, we can rewrite equation (A.17)

$$\begin{cases} a\cos\Delta\cos(\alpha - \beta) = b\sin\Delta\sin(\alpha + \beta) \\ a\sin\Delta\cos(\alpha + \beta) = b\cos\Delta\sin(\alpha - \beta) \end{cases} \tag{A.18}$$

If we divide the first equation of the system (A.18) by $a\cos\Delta$ and second one by $b\cos\Delta$, we get

$$\begin{cases} \cos(\alpha - \beta) = \frac{b}{a}\tan\Delta\sin(\alpha + \beta) \\ \sin(\alpha - \beta) = \frac{a}{b}\tan\Delta\cos(\alpha + \beta) \end{cases} \tag{A.19}$$

To solve this system of two equations, both equations are multiplied by the factor ab and we define the sum of their squares as

$$a^2b^2(\cos^2(\alpha - \beta) + \sin^2(\alpha - \beta)) = \tan^2\Delta(b^4\sin^2(\alpha + \beta) + a^4\cos^2(\alpha + \beta)) \tag{A.20}$$

Using $\cos^2(\alpha - \beta) + \sin^2(\alpha - \beta) = 1$ and $a^2 + b^2 = 1$, we get

$$a^2b^2 = \tan^2\Delta(b^4\sin^2(\alpha + \beta) + (1 - b^2)(1 - b^2)\cos^2(\alpha + \beta))$$

which is also

$$\Leftrightarrow a^2b^2 = \tan^2\Delta(b^4\sin^2(\alpha+\beta) + (1+b^4-2b^2)\cos^2(\alpha+\beta))$$

After simplification, we get

$$\Leftrightarrow a^2b^2 = \tan^2\Delta(b^4\sin^2(\alpha+\beta) + b^4\cos^2(\alpha+\beta) + (1-2b^2)\cos^2(\alpha+\beta))$$

From $\cos^2(\alpha+\beta)+\sin^2(\alpha+\beta)=1$, we obtain

$$\Leftrightarrow a^2b^2 = \tan^2\Delta(b^4 + (1-2b^2)\cos^2(\alpha+\beta)) \tag{A.21}$$

Using equation (A.21), we express $\cos(\alpha+\beta)$ as

$$\cos(\alpha+\beta) = \frac{1}{\tan\Delta}\frac{b}{\sqrt{1-2b^2}}\sqrt{a^2-b^2\tan^2\Delta} \tag{A.22}$$

In our case $a=1$ and $b<<1$, therefore $\sqrt{1-2b^2}\approx 1$, $\sqrt{a^2-b^2\tan^2\Delta}\approx\sqrt{a^2}=a=1$ and

$$\cos(\alpha+\beta) = \frac{b}{\tan\Delta} \tag{A.23}$$

Therefore,

$$\sin(\alpha+\beta) = \sqrt{1-\frac{b^2}{\tan^2\Delta}} \tag{A.24}$$

Inserting Eq. (A.23) and Eq. (A.24) into the system of equation (A.19), we get

$$\begin{cases}\cos(\alpha-\beta) = \frac{b}{a}\tan\Delta\sin(\alpha+\beta)\\ \sin(\alpha-\beta) = \frac{a}{b}\tan\Delta\cos(\alpha+\beta)\end{cases}$$

which is also

$$\Leftrightarrow \begin{cases}\cos(\alpha-\beta) = \frac{b}{a}\tan\Delta\sqrt{1-\frac{b^2}{\tan^2\Delta}}\\ \sin(\alpha-\beta) = a\end{cases}$$

Finally, the solution of the system of equation (A.19) is given by

$$\begin{cases}\cos(\alpha-\beta) = b\tan\Delta\\ \sin(\alpha-\beta) = 1\end{cases} \tag{A.25}$$

Now, we want to extract the values of α and β from equation (A.25). For this reason, we use the definition of the analyzer angle $\alpha = \frac{\pi}{2}+\epsilon$ in case of mirror measurement at cross-polarization :

$$\cos(\alpha-\beta) = b\tan\Delta \Leftrightarrow \cos\left(\frac{\pi}{2}+\epsilon-\beta\right) = b\tan\Delta$$

Using the identity $\cos(A+B) = \cos A \cos B - \sin A \sin B$, we obtain

$$\Leftrightarrow \cos\left(\frac{\pi}{2}\right)\cos(\epsilon-\beta) - \sin\left(\frac{\pi}{2}\right)\sin(\epsilon-\beta) = b\tan\Delta$$

Thus

$$\Leftrightarrow -\sin(\epsilon-\beta) = b\tan\Delta$$

In the approximation of small angles $\sin(\epsilon-\beta) = (\epsilon-\beta)$:

$$\Leftrightarrow -(\epsilon-\beta) = b\tan\Delta$$

We recall that $\alpha = \frac{\pi}{2} + \epsilon$, therefore

$$\Leftrightarrow \beta + \frac{\pi}{2} - \alpha = b\tan\Delta \tag{A.26}$$

In case of no mirror measurement, the analyzer angle α_0 is related to the polarizer angle β by the following expression: $\alpha_0 - \beta = \frac{\pi}{2}$. Moreover, we define a system of equation for mirror/no mirror measurement as:

$$\begin{cases} \alpha - \beta = \frac{\pi}{2} \mp b\tan\Delta \\ \alpha_0 - \beta = \frac{\pi}{2} \end{cases}$$

which reduces to

$$\boxed{\Leftrightarrow \alpha - \alpha_0 = \mp b\tan\Delta} \tag{A.27}$$

with α and α_0 are the analyzer angle for mirror/no mirror measurement at cross-polarization for a given polarizer angle β.

A.5 Maximum acceptable limit of polarization leakage

In this part, we would like to get an accurate value of the polarization leakage b^2. We recall equation (A.21): $a^2b^2 = \tan^2\Delta(b^4 + (1-2b^2)\cos^2(\alpha+\beta))$.
Using $a^2 + b^2 = 1$, we obtain

$$b^2 - b^4 = \tan^2\Delta(b^4 + (1-2b^2)\cos^2(\alpha+\beta)) \tag{A.28}$$

For the sake of simplification, we consider $A = \tan^2\Delta$ usually $A >> 1$ and $x = \cos^2(\alpha+\beta)$. Therefore,

$$b^2 - b^4 = A(b^4 + (1-2b^2)x) \tag{A.29}$$

We write the equation (A.29) in form of a polynomial function in b,

$$\Leftrightarrow b^4(1+A) - b^2(1+2Ax) + Ax = 0 \tag{A.30}$$

We divide equation (A.30) by the factor $1+A$ and we get:

$$\Leftrightarrow b^4 - b^2\frac{1+2Ax}{1+A} + \frac{Ax}{1+A} = 0 \tag{A.31}$$

Now, let us study the possible solutions for this equation. One could show that:

$$b^2 = \frac{1}{2}\left\{\frac{1+2Ax}{1+A} \pm \sqrt{\frac{(1+2Ax)^2}{(1+A)^2} - \frac{4Ax}{1+A}}\right\}$$

which is also

$$\Leftrightarrow b^2 = \frac{1}{2}\frac{1+2Ax}{1+A}\left\{1 \pm \sqrt{1 - \frac{4Ax(1+A)}{(1+2Ax)^2}}\right\} \tag{A.32}$$

There are no solutions for b when the term under the square root is < 0, so we must have

$$1 - \frac{4Ax(1+A)}{(1+2Ax)^2} > 0 \tag{A.33}$$

We multiply the equation (A.33) by the factor $(1+2Ax)^2$

$$\Leftrightarrow (1+2Ax)^2 > 4Ax(1+A)$$

This defines the range of x_{max} which can be determined by the solving the following equation

$$\Leftrightarrow (1+2Ax)^2 - 4Ax(1+A) = 0 \tag{A.34}$$

Using the identity $(u+v)^2 = u^2 + 2uv + v^2$, we get

$$\Leftrightarrow 1 + 4A^2x^2 + 4Ax - 4Ax(1+A) = 0 \tag{A.35}$$

We write the equation (A.35) in form of a polynomial function in x,

$$\Leftrightarrow 4A^2x^2 + (4A - 4A - 4A^2)x + 1 = 0 \tag{A.36}$$

We divide equation (A.38) by the factor $4A^2$ and we obtain:

$$\Leftrightarrow x^2 + \frac{-4A^2}{4A^2}x + \frac{1}{4A^2} = 0$$

which is also

$$\Leftrightarrow x^2 - x + \frac{1}{4A^2} = 0 \tag{A.37}$$

The two possible solutions of equation (A.37) are

$$\begin{cases} x_{max+} = \frac{1}{2}\left\{1 + \sqrt{1 - \frac{1}{A^2}}\right\} \\ x_{max-} = \frac{1}{2}\left\{1 - \sqrt{1 - \frac{1}{A^2}}\right\} \end{cases} \tag{A.38}$$

When $(1+2Ax)^2 - 4Ax(1+A) = 0$, equation (A.32) becomes

$$\Leftrightarrow b^2 = \frac{1}{2}\frac{1+2Ax}{1+A} \tag{A.39}$$

Therefore, the possible values of b^2 are given by:

$$\begin{cases} b^2_{max+} = \frac{1}{2}\frac{1+2Ax_{max+}}{1+A} \\ b^2_{max-} = \frac{1}{2}\frac{1+2Ax_{max-}}{1+A} \end{cases} \tag{A.40}$$

Inserting equation (A.37) into equation (A.40) we get

$$\begin{cases} b^2_{max+} = \frac{1}{2}\left(1+\sqrt{\frac{A-1}{A+1}}\right) \\ b^2_{max-} = \frac{1}{2}\left(1-\sqrt{\frac{A-1}{A+1}}\right) \end{cases} \tag{A.41}$$

Recalling that $A = \tan^2\Delta$, finally

$$\begin{cases} b^2_{max+} = \frac{1}{2}\left(1+\sqrt{\frac{\tan^2\Delta-1}{\tan^2\Delta+1}}\right) \\ b^2_{max-} = \frac{1}{2}\left(1-\sqrt{\frac{\tan^2\Delta-1}{\tan^2\Delta+1}}\right) \end{cases} \tag{A.42}$$

Appendix B

Supplementary information to chapter 4 "Modal transformation of a reflected polarized Gaussian beam"

B.1 Reflection matrix as a function of (u, v) (equation (4.3))

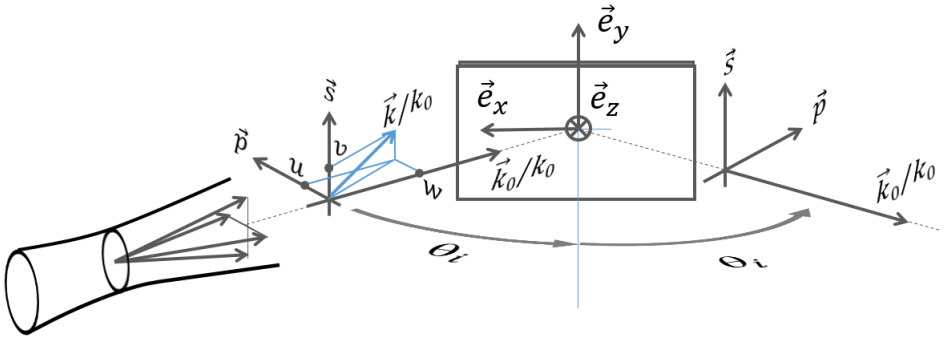

Figure B.1: Geometry of beam reflection off a mirror. The incident beam has a Gaussian field distribution in the transverse plane. The transverse u, v and longitudinal w wavenumbers depends on the angle of incidence as explained in previous chapter.

Here we use the general wave propagation convention $\exp(ikr - i\omega t)$. We consider that the finite size beam before the mirror results from a Gaussian weighted superposition of plane waves propagating along an angular distribution $\vec{k}/k_0 = u\vec{p} + v\vec{s} + w\vec{k}_0/k_0$ narrowly centered around $\vec{k}_0$ with $k_0 = 2\pi/\lambda$ where u, v and w are angular variables along $\vec{p}$, $\vec{s}$ and $\vec{k}_0/k_0$ respectively. For each plane wave component, we choose a coordinate system $\vec{e}_p$, $\vec{e}_s$, $\vec{k}/k_0$ that defines a local incidence plane for that wave. The longitudinal basis vector is $\vec{k}/k_0$ and the

transverse ones are $\vec{e_s} = \vec{k}/k_0 \times \vec{e_z}$ and $\vec{e_p} = (\vec{k}/k_0 \times \vec{e_z}) \times (\vec{k}/k_0)$ in the s and p planes respectively. We now express these vectors in the coordinate system $\vec{p}$, $\vec{s}$, $\vec{k}_0/k_0$ as depicted below

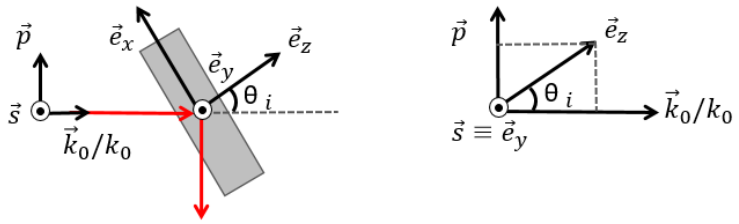

Figure B.2: Schematic illustration of reflection geometry. $\vec{k}/k_0 = u\vec{p} + v\vec{s} + w\vec{k}_0/k_0$ is the wavenumber vector with $\vec{k}_0$ with $k_0 = 2\pi/\lambda$ and u, v and w are angular variables along $\vec{p}$, $\vec{s}$ and $\vec{k}_0/k_0$ respectively.

Therefore,

$$\overrightarrow{e_s} = \vec{k}/k_0 \times \vec{e_z} = \begin{bmatrix} u \\ v \\ w \end{bmatrix} \times \begin{bmatrix} \sin\theta_i \\ 0 \\ \cos\theta_i \end{bmatrix} = \begin{bmatrix} v\cos\theta_i \\ -u\cos\theta_i + w\sin\theta_i \\ -v\sin\theta_i \end{bmatrix} \tag{B.1}$$

and

$$\overrightarrow{e_p} = (\vec{k}/k_0 \times \vec{e_z}) \times (\vec{k}/k_0) = \begin{bmatrix} v\cos\theta_i \\ -u\cos\theta_i + w\sin\theta_i \\ -v\sin\theta_i \end{bmatrix} \times \begin{bmatrix} u \\ v \\ w \end{bmatrix}$$

we calculate the cross product of the two vectors

$$= \begin{bmatrix} w(-u\cos\theta_i + w\sin\theta_i) - v^2\sin\theta_i \\ -vw\cos\theta_i - uv\sin\theta_i \\ (u^2+v^2)\cos\theta_i - uw\sin\theta_i \end{bmatrix} \tag{B.2}$$

In the paraxial limit $u, v << \theta_i$, we can write

$$\overrightarrow{e_s} = \sin\theta_i \begin{bmatrix} v\cot\theta_i \\ -u\cot\theta_i + w \\ -v \end{bmatrix} \approx \begin{bmatrix} v\cot\theta_i \\ 1 \\ -v \end{bmatrix} \tag{B.3}$$

and

$$\overrightarrow{e_p} = \sin\theta_i \begin{bmatrix} -u\cot\theta_i + w^2 - v^2 \\ -vw\cot\theta_i - uv \\ (u^2+v^2)\cot\theta_i - uw \end{bmatrix} \approx \begin{bmatrix} 1 \\ -v\cot\theta_i \\ -u \end{bmatrix} \tag{B.4}$$

To obtain the reflectivity of the mirror for each plane wave, we determine first the weights of p- and s- field-components, given by the weighted projections $r_{p,uv}(\vec{e_p} \cdot \vec{E}_{0uv})$ and $r_{s,uv}(\vec{e_s} \cdot \vec{E}_{0uv})$. We determine then the resulting reflected field

transverse field along the corresponding reflected basis $\vec{e}_{s,R} = \vec{k}_R/k_0 \times \vec{e}_z$ and $\vec{e}_{p,R} = (\vec{k}_R/k_0 \times \vec{e}_z) \times (\vec{k}_R/k_0)$ such $\vec{E}_{uv} = r_{p,uv}(\vec{e}_p \cdot \vec{E}_{0uv})\vec{e}_{p,R} + r_{s,uv}(\vec{e}_s \cdot \vec{E}_{0uv})\vec{e}_{s,R}$. Here $\vec{k}_R$ is the mirrored wave vector after reflection. In the paraxial limit, for a beam impinging, the Fresnel coefficients are developed to the first order in u around θ_i and v around 0, giving: $r_{p,uv} = r_p + u\ \partial r_p/\partial\theta_i$ and $r_{s,uv} = r_s + u\ \partial r_s/\partial\theta_i$. The first order derivatives $\partial r_{p/s\ uv}/\partial v$ in the s-plane vanish both for r_p and r_s leaving just derivative $r_p^{'} = \partial r_p/\partial\theta_i$ and $r_s^{'} = \partial r_s/\partial\theta_i$. We calculate the components of the reflected basis vectors $\vec{e}_{p,R}$, $\vec{e}_{s,R}$, $\vec{k}_R$ in the paraxial limit $u, v << \theta_i$.
Therefore, we obtain

$$\vec{e}_{p,R} = \overrightarrow{e_p}(-u, v, \pi - \theta_i) \approx \begin{bmatrix} 1 \\ v\cot\theta_i \\ u \end{bmatrix} \tag{B.5}$$

and similarly we get

$$\vec{e}_{s,R} = \overrightarrow{e_s}(-u, v, \pi - \theta_i) \approx \begin{bmatrix} -v\cot\theta_i \\ 1 \\ -v \end{bmatrix} \tag{B.6}$$

Inserting equation (B.3), (B.4), (B.5) and (B.6) into $\vec{E}_{uv}$ we obtain

$$\vec{E}_{uv} = r_{p,uv}(\vec{e}_p \cdot \vec{E}_{0uv})\vec{e}_{p,R} + r_{s,uv}(\vec{e}_s \cdot \vec{E}_{0uv})\vec{e}_{s,R} \tag{B.7}$$

For simplicity, we only calculate the components along $\vec{p}$ and $\vec{s}$ of equation (B.7)

$$\vec{E}_{uv} = r_{p,uv}\left(\begin{bmatrix} 1 \\ -v\cot\theta_i \end{bmatrix} \cdot \begin{bmatrix} E_p \\ E_s \end{bmatrix}\right)\begin{bmatrix} 1 \\ v\cot\theta_i \end{bmatrix} + r_{s,uv}\left(\begin{bmatrix} v\cot\theta_i \\ 1 \end{bmatrix} \cdot \begin{bmatrix} E_p \\ E_s \end{bmatrix}\right)\begin{bmatrix} -v\cot\theta_i \\ 1 \end{bmatrix} \tag{B.8}$$

Calculating first the scalar product terms $(\vec{e}_p \cdot \vec{E}_{0uv})$ and $(\vec{e}_s \cdot \vec{E}_{0uv})$,

$$\vec{E}_{uv} = r_{p,uv}(E_p - v\cot\theta_i E_s)\begin{bmatrix} 1 \\ v\cot\theta_i \end{bmatrix} + r_{s,uv}(v\cot\theta_i E_s + E_p)\begin{bmatrix} -v\cot\theta_i \\ 1 \end{bmatrix} \tag{B.9}$$

then we have

$$\vec{E}_{uv} = \begin{bmatrix} r_{p,uv}(E_p - v\cot\theta_i E_s) \\ v\cot\theta_i r_{p,uv}(E_p - v\cot\theta_i E_s) \end{bmatrix} + \begin{bmatrix} -v\cot\theta_i r_{s,uv}(v\cot\theta_i E_s + E_p) \\ r_{s,uv}(v\cot\theta_i E_s + E_p) \end{bmatrix} \tag{B.10}$$

which is also

$$\vec{E}_{uv} = \begin{bmatrix} r_{p,uv}(E_p - v\cot\theta_i E_s) - v\cot\theta_i r_{s,uv}(v\cot\theta_i E_s + E_p) \\ v\cot\theta_i r_{p,uv}(E_p - v\cot\theta_i E_s) + r_{s,uv}(v\cot\theta_i E_s + E_p) \end{bmatrix} \tag{B.11}$$

Inserting $r_{p,uv} = r_p + u\ \partial r_p/\partial\theta_i$ and $r_{s,uv} = r_s + u\ \partial r_s/\partial\theta_i$ into equation (B.11), we get

$$\vec{E}_{uv} = \begin{bmatrix} (r_p + u\ \partial r_p/\partial\theta_i)(E_p - v\cot\theta_i E_s) - v\cot\theta_i(r_s + u\ \partial r_s/\partial\theta_i)(v\cot\theta_i E_s + E_p) \\ v\cot\theta_i(r_p + u\ \partial r_p/\partial\theta_i)(E_p - v\cot\theta_i E_s) + (r_s + u\ \partial r_s/\partial\theta_i)(v\cot\theta_i E_s + E_p) \end{bmatrix}$$

Up to the first order in u and v, the reflected field vector is then given by:

$$\vec{E}_{uv} = \begin{bmatrix} r_p E_p + u E_p \ \partial r_p/\partial\theta_i - E_s r_p v \cot\theta_i - E_s r_s v \cot\theta_i \\ E_p r_p v \cot\theta_i + E_p r_s v \cot\theta_i + r_s E_s + u E_s \ \partial r_s/\partial\theta_i \end{bmatrix} \tag{B.12}$$

After simplification, we can write

$$\vec{E}_{uv} = \begin{bmatrix} r_p E_p + u E_p \ \partial r_p/\partial\theta_i - E_s (r_p + r_s) v \cot\theta_i \\ r_s E_s + u E_s \ \partial r_s/\partial\theta_i + E_p (r_p + r_s) v \cot\theta_i \end{bmatrix} \tag{B.13}$$

Using $r'_{p/s} = \partial r_{p/s}/\partial\theta_i$ in equation (B.13) , we obtain

$$\vec{E}_{uv} = \begin{bmatrix} r_p E_p + u E_p \ r'_p - E_s (r_p + r_s) v \cot\theta_i \\ r_s E_s + u E_s \ r'_s + E_p (r_p + r_s) v \cot\theta_i \end{bmatrix} \tag{B.14}$$

We express the result in terms of matrix notation in the standard $\vec{p}, \vec{s}$ basis such that

$$\vec{E}_{uv} = \bar{\bar{M}}_{u,v} \ \vec{E}_{0uv}$$

where

$$\vec{E}_{uv} = \begin{bmatrix} r_p + u r'_p & -v \cot\theta_i (r_p + r_s) \\ v \cot\theta_i (r_p + r_s) & r_s + u r'_s \end{bmatrix} \begin{bmatrix} E_p \\ E_s \end{bmatrix} \tag{B.15}$$

One can conclude that

$$\bar{\bar{M}}_{u,v} = \begin{bmatrix} r_p + u r'_p & -v \cot\theta_i (r_p + r_s) \\ v \cot\theta_i (r_p + r_s) & r_s + u r'_s \end{bmatrix} \tag{B.16}$$

It is convenient to write separately the components of equation (B.16) depending on u and v variables in order to discuss the modal transformation of the incident beam. Thus,

$$\bar{\bar{M}}_{u,v} = \begin{bmatrix} r_p & 0 \\ 0 & r_s \end{bmatrix} + u \begin{bmatrix} r'_p & 0 \\ 0 & r'_s \end{bmatrix} + v \frac{r_p + r_s}{\tan\theta_i} \begin{bmatrix} 0 & -1 \\ 1 & 0 \end{bmatrix} \tag{B.17}$$

B.2 Reflected field distribution in the (x, y) domain (equation (4.4))

To calculate the expression of the reflected beam detected after the lens, we need to derive the field distribution that result when we focus a particular far-field onto an image plane. To get a better feeling we assume the lens is illuminated by a plane wave field $\vec{E}(u, v)$ traveling along $\vec{k}$ at an angle u, v off a given optical axis of a lens as depicted below. A surface element of a focusing lens such $dS = dxdy$ cause a field density at location (x', y'). This field is caused by the plane wave at

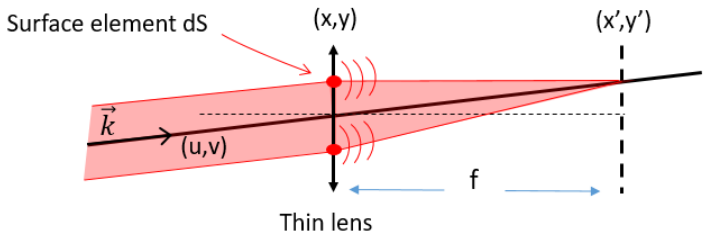

Figure B.3: Focusing of a plane wave into a point as explained in text. f is the focal length. $\vec{k}$ wavevector at an angle u, v. $dS = dxdy$ a surface element of a focusing lens

angle u, v so it will be indexed such as: $E_{u,v}(x', y')$. Here we use the general wave propagation convention $\exp(ikr - i\omega t)$. Fresnel-Huygens principle dictate that each point of the surface element dS emit coherently as a single point emitter.

The total field caused at (x', y') due to the plane wave $E(u, v)$ field density over the area dS is therefore:

$$\iint_{-\infty}^{+\infty} E_{u,v}(x', y')\, dx'\, dy' = \alpha \iint_{-\infty}^{+\infty} E(u, v)\, \frac{\exp + i\vec{k} \cdot \vec{r}}{|\vec{r}|}\, dx\, dy \tag{B.18}$$

where α is a normalization constant to be calculated. Fresnel-Huygens principle can be easily treated in a paraxial approximation here for which the largest contribution of the field at (x, y) causing a field at (x', y') are due to the location of the surface such $x << f$, $y << f$. So we can expand

$$r^2 = f^2 + x^2 + y^2 = f^2(1 + \frac{x^2 + y^2}{f^2}) \tag{B.19}$$

In the paraxial approximation $x << f$ and $y << f$ we can show that:

$$|\vec{r}| \approx f + \frac{x^2 + y^2}{2f} \tag{B.20}$$

replacing $|\vec{r}|$ in we get

$$\iint_{-\infty}^{+\infty} E_{u,v}(x', y')\, dx'\, dy' = \alpha E(u, v) \frac{\exp(ikf)}{f} \iint_{-\infty}^{+\infty} \exp + ik \frac{x^2 + y^2}{2f}\, dx\, dy \tag{B.21}$$

here $E(u, v)$ being a plane wave field density does not depend on (x, y). Also in our approximation we have taken the denominator $|\vec{r}| \approx f$. Now physically the full field at (x', y') namely $\iint_{-\infty}^{+\infty} E_{u,v}(x', y')\, dx'\, dy'$ is caused by the full field $E(u, v)$ of the plane wave. So we have

$$|\vec{r}| \approx f + \frac{x^2+y^2}{2f} \tag{B.22}$$

replacing $|\vec{r}|$ in we get

$$\iint_{-\infty}^{+\infty} E_{u,v}(x',y')\,dx'\,dy' = \alpha E(u,v)\frac{\exp(ikf)}{f} \tag{B.23}$$

making use of equation (B.23) in (B.21) we get

$$1 = \frac{\alpha}{f}\iint_{-\infty}^{+\infty} \exp{+ik\frac{x^2+y^2}{2f}}\,dx\,dy \tag{B.24}$$

using a first identification $R^2 = x^2 + y^2$, the integral becomes

$$1 = \frac{\alpha}{f}\int_0^{2\pi}\int_0^{+\infty} \exp{+ik\frac{R^2}{2f}}R\,dR\,d\psi \tag{B.25}$$

which is also

$$1 = 2\pi\alpha\int_0^{+\infty} \exp{+ik\frac{R^2}{2f}}\frac{2RdR}{2f} \tag{B.26}$$

making second identification $-W = ikR^2/2f$, we get

$$-\frac{dW}{ik} = \frac{2RdR}{2f} \tag{B.27}$$

which is also

$$i\frac{dW}{k} = \frac{2RdR}{2f} \tag{B.28}$$

Using the above formula in the integral we get

$$1 = \frac{2\pi\alpha i}{k}\int_0^{+\infty} (\exp -W)dW \tag{B.29}$$

which is also

$$1 = \frac{2\pi\alpha i}{k} \tag{B.30}$$

since $k = 2\pi/\lambda$, we finally get $1 \approx \alpha i\lambda$. Thus, $\alpha = -i/\lambda$.

In our case, we consider the propagation of a Gaussian field angular distribution (source plane) indicated by the coordinate variables u and v. At the source plane, the area $dS = dudv$ defines the extent of the beam. The field distribution in the source plane is given by $E_{u,v}(u,v)$ and the field $\vec{\mathcal{E}}_{fx,y}(x,y)$ in the observation plane. Now back to equation B.18, in the paraxial approximation we have:

$$\vec{\mathcal{E}}_{fx,y}(x,y) = \frac{-i}{\lambda}\iint_{-\infty}^{+\infty} E_{u,v}(u,v)\ \frac{exp + i\vec{k}\cdot\vec{r}}{|\vec{r}|}\,du\,dv \tag{B.31}$$

Here $\vec{k}/k_0 = u\vec{p} + v\vec{s} + w\vec{k}_0/k_0$ narrowly centered around $\vec{k}_0$ with $k_0 = 2\pi/\lambda$ and $\vec{r} = x\vec{p} + y\vec{s}$ is the distance between a position on the source plane and a position in the observation plane. Thus, we obtain:

$$\vec{\mathcal{E}}_{fx,y}(x,y) = \frac{-i}{\lambda f}\exp(+ik_0 f)\iint_{-\infty}^{+\infty} E_{u,v}(u,v)\ \exp[+ik_0(xu+yv)]\,du\,dv \tag{B.32}$$

In what follows, we will drop the phase term $\exp +ik_0 f$ as we are interested to express the field in the focal region.

B.2.1 p-polarization

In our case a p-polarized light is obtained at $\beta = 0$ and its corresponding cross-polarization is reached when $\alpha = \pi/2$. For simplicity, we calculate the reflectivity of a p-polarized beam at cross-polarization in case of $a = 1$ and $b = 0$. We recall that the reflected field distribution after the mirror for each angle u, v

$$\vec{E}_{uv} = \bar{\bar{A}}(\alpha)\bar{\bar{M}}_{u,v}\bar{\bar{P}}(\beta)\vec{E}_{0uv} \tag{B.33}$$

where

$$\bar{\bar{M}}_{u,v} = \begin{bmatrix} r_p & 0 \\ 0 & r_s \end{bmatrix} + u\begin{bmatrix} r'_p & 0 \\ 0 & r'_s \end{bmatrix} + v\frac{r_p + r_s}{\tan\theta_i}\begin{bmatrix} 0 & -1 \\ 1 & 0 \end{bmatrix} \tag{B.34}$$

and

$$\vec{E}_{0uv} = \frac{E_0}{\pi\theta_0^2}\ \exp\left(-\frac{u^2+v^2}{\theta_0^2}\right)\begin{bmatrix}\cos\beta \\ \sin\beta\end{bmatrix} \tag{B.35}$$

When $\beta = 0$ and $\alpha = \pi/2$, $\bar{\bar{A}}(\alpha) = \begin{bmatrix} 0 & 0 \\ 0 & 1 \end{bmatrix}$ and $\bar{\bar{P}}(\beta) = \begin{bmatrix} 1 & 0 \\ 0 & 0 \end{bmatrix}$. Therefore, we find that

$$\vec{E}_{uv} = \frac{E_0}{\pi\theta_0^2}\ \exp\left(-\frac{u^2+v^2}{\theta_0^2}\right)\begin{bmatrix} 0 & 0 \\ 0 & 1 \end{bmatrix}\begin{bmatrix} r_p + ur'_p & -v\cot\theta_i(r_p+r_s) \\ v\cot\theta_i(r_p+r_s) & r_s + ur'_s \end{bmatrix}\begin{bmatrix} 1 & 0 \\ 0 & 0 \end{bmatrix}\begin{bmatrix} 1 \\ 0 \end{bmatrix} \tag{B.36}$$

We simplify the expression of equation (B.36) by performing the matrix multiplication,

$$\vec{E}_{uv} = \frac{E_0}{\pi\theta_0^2}\exp\left(-\frac{u^2+v^2}{\theta_0^2}\right)\begin{bmatrix}0 & 0\\ 0 & 1\end{bmatrix}\begin{bmatrix}r_p + ur_p' & -v\cot\theta_i(r_p+r_s)\\ v\cot\theta_i(r_p+r_s) & r_s+ur_s'\end{bmatrix}\begin{bmatrix}1\\0\end{bmatrix} \tag{B.37}$$

After calculation, we can write

$$\Leftrightarrow \vec{E}_{uv} = \frac{E_0}{\pi\theta_0^2}\exp\left(-\frac{u^2+v^2}{\theta_0^2}\right)\begin{bmatrix}0 & 0\\ 0 & 1\end{bmatrix}\begin{bmatrix}r_p + ur_p'\\ v\cot\theta_i(r_p+r_s)\end{bmatrix} \tag{B.38}$$

which is also

$$\Leftrightarrow \vec{E}_{uv} = \frac{E_0}{\pi\theta_0^2}\exp\left(-\frac{u^2+v^2}{\theta_0^2}\right)\begin{bmatrix}0\\ v\cot\theta_i(r_p+r_s)\end{bmatrix} \tag{B.39}$$

Finally, the reflected field distribution in the (u,v) domain for p-polarized beam is given by:

$$\vec{E}_{uv} = \frac{E_0}{\pi\theta_0^2} v\cot\theta_i(r_p+r_s)\exp\left(-\frac{u^2+v^2}{\theta_0^2}\right)\vec{e}_y \tag{B.40}$$

From equation (B.40), we can recognize that the field depends only on the angular variable v when the polarizer and analyzer are considered perfect i.e without polarization leakage. Now we want to calculate the expression of the reflected beam at the focal plane. For this purpose, we recall the Fourier transform property of a lens as defined previously in Appendix B.2:

$$\vec{\mathcal{E}}_{fx,y} = \frac{-i}{\lambda f}\exp\left(+ik_0 f\right)\iint_{-\infty}^{+\infty}\vec{E}_{u,v}\exp[+ik_0(xu+yv)]\,du\,dv \tag{B.41}$$

In what follows we will drop the propagation phase term $\exp+ik_0 f$ as we from now on just concern with establishing the field at focal plane only. Thus, the cross-polarized reflected beam at the focal plane $\mathcal{E}_{f\perp}$ is given by:

$$\mathcal{E}_{f\perp} = \frac{-i}{\lambda f}\frac{E_0}{\pi\theta_0^2}\iint_{-\infty}^{+\infty} v\cot\theta_i(r_p+r_s)\exp\left(-\frac{u^2+v^2}{\theta_0^2}\right)\exp[ik_0(xu+yv)]\,du\,dv \tag{B.42}$$

We keep only terms depending on u and v in the integral

$$\mathcal{E}_{f\perp} = \frac{-i}{\lambda f}\frac{E_0}{\pi\theta_0^2}\iint_{-\infty}^{+\infty} v\exp\left(-\frac{u^2+v^2}{\theta_0^2}\right)\exp[ik_0(xu+yv)]\,du\,dv \tag{B.43}$$

For the sake of simplicity, we calculate each integral separately

$$\mathcal{E}_{f\perp} = \frac{-i}{\lambda f}\frac{E_0}{\pi\theta_0^2}\int_{-\infty}^{+\infty}\exp\left\{\frac{-u^2}{\theta_0^2}+iuk_0x\right\}du\int_{-\infty}^{+\infty} v\exp\left\{\frac{-v^2}{\theta_0^2}+ivk_0y\right\}dv \tag{B.44}$$

which is also

$$\mathcal{E}_{f\perp} = \frac{-i}{\lambda f}\frac{E_0}{\pi\theta_0^2}\int_{-\infty}^{+\infty}\exp\left\{\frac{-1}{\theta_0^2}\left(u - iuk_0x\theta_0^2\right)\right\}du\int_{-\infty}^{+\infty}v\exp\left\{\frac{-1}{\theta_0^2}\left(v - ivk_0y\theta_0^2\right)\right\}dv$$

In order to calculate both integrals, we write the exponent terms in form of a polynomial in u and v respectively

$$\mathcal{E}_{f\perp} = \frac{-i}{\lambda f}\frac{E_0}{\pi\theta_0^2}\int_{-\infty}^{+\infty}\exp\left\{\frac{-1}{\theta_0^2}\left(u - i\frac{\theta_0^2k_0x}{2}\right)^2 - \frac{\theta_0^2k_0^2x^2}{4}\right\}du$$
$$\int_{-\infty}^{+\infty}v\exp\left\{\frac{-1}{\theta_0^2}\left(v - i\frac{\theta_0^2k_0y}{2}\right)^2 - \frac{\theta_0^2k_0^2y^2}{4}\right\}dv$$

The terms independent of u and v can be moved outside the integrals

$$\mathcal{E}_{f\perp} = \frac{-i}{\lambda f}\frac{E_0}{\pi\theta_0^2}\exp\left\{-\frac{\theta_0^2k_0^2x^2 + \theta_0^2k_0^2y^2}{4}\right\}$$
$$\int_{-\infty}^{+\infty}\exp\left\{\frac{-1}{\theta_0^2}\left(u - i\frac{\theta_0^2k_0x}{2}\right)^2\right\}du\int_{-\infty}^{+\infty}v\frac{-1}{\theta_0^2}\left(v - i\frac{\theta_0^2k_0y}{2}\right)^2dv$$

Using $\int_{-\infty}^{+\infty}x\exp -a(x-b)^2\,dx = b\sqrt{\pi/a},\ a>0$, we find that

$$\mathcal{E}_{f\perp} = \frac{-i}{\lambda f}\frac{E_0}{\pi\theta_0^2}\exp\left\{-\frac{\theta_0^2k_0^2x^2 + \theta_0^2k_0^2y^2}{4}\right\}i\frac{\theta_0^2k_0y}{2}\sqrt{\pi\theta_0^2}\sqrt{\pi\theta_0^2}$$

which is also

$$\mathcal{E}_{f\perp} = \frac{-i}{\lambda f}\frac{E_0}{\pi\theta_0^2}\pi\theta_0^2i\frac{\theta_0^2k_0y}{2}\exp\left\{-\frac{\theta_0^2k_0^2x^2 + \theta_0^2k_0^2y^2}{4}\right\} \tag{B.45}$$

The angular mode divergence is given by $\theta_0 = \omega_0/f$ which is also $\lambda/(\pi\omega_f)$ with $\omega_0 = \lambda f/(\pi\omega_f)$. Using $\theta_0^2k_0^2/4 = 1/\omega_f^2$ and $\theta_0^2k_0/2 = 2/k_0\omega_f^2 = 1/l_f$, we find that the reflected field distribution in the (x,y) domain for p beam is expressed as:

$$\mathcal{E}_{f\perp} = \frac{E_0}{\pi\omega_f^2}\frac{y}{l_f}\exp -\frac{x^2+y^2}{\omega_f^2} \tag{B.46}$$

B.2.2 *s*-polarization

The following example use the same calculation method as in section B.2.1. We start our analysis by considering an s-polarized beam reflected off a mirror i.e

$\beta = \pi/2$ and $\alpha = 0$. The reflected field distribution after the mirror for each angle u, v is given by

$$\vec{E}_{uv} = \bar{\bar{A}}(\alpha)\bar{\bar{M}}_{u,v}\bar{\bar{P}}(\beta)\vec{E}_{0uv} \tag{B.47}$$

When $\beta = \pi/2$ and $\alpha = 0$, $\bar{\bar{A}}(\alpha) = \begin{bmatrix} 1 & 0 \\ 0 & 0 \end{bmatrix}$ and $\bar{\bar{P}}(\beta) = \begin{bmatrix} 0 & 0 \\ 0 & 1 \end{bmatrix}$. Therefore, we obtain

$$\vec{E}_{uv} = \frac{E_0}{\pi\theta_0^2}\exp\left(-\frac{u^2+v^2}{\theta_0^2}\right)\begin{bmatrix} 1 & 0 \\ 0 & 0 \end{bmatrix}\begin{bmatrix} r_p + ur'_p & -v\cot\theta_i(r_p+r_s) \\ v\cot\theta_i(r_p+r_s) & r_s + ur'_s \end{bmatrix}\begin{bmatrix} 0 & 0 \\ 0 & 1 \end{bmatrix}\begin{bmatrix} 0 \\ 1 \end{bmatrix} \tag{B.48}$$

We simplify the expression of equation (B.48) by performing the matrix multiplication,

$$\vec{E}_{uv} = \frac{E_0}{\pi\theta_0^2}\exp\left(-\frac{u^2+v^2}{\theta_0^2}\right)\begin{bmatrix} 1 & 0 \\ 0 & 0 \end{bmatrix}\begin{bmatrix} r_p + ur'_p & -v\cot\theta_i(r_p+r_s) \\ v\cot\theta_i(r_p+r_s) & r_s + ur'_s \end{bmatrix}\begin{bmatrix} 0 \\ 1 \end{bmatrix} \tag{B.49}$$

After calculation we get

$$\Leftrightarrow \vec{E}_{uv} = \frac{E_0}{\pi\theta_0^2}\exp\left(-\frac{u^2+v^2}{\theta_0^2}\right)\begin{bmatrix} 1 & 0 \\ 0 & 0 \end{bmatrix}\begin{bmatrix} -v\cot\theta_i(r_p+r_s) \\ r_s + ur'_s \end{bmatrix} \tag{B.50}$$

which is also

$$\Leftrightarrow \vec{E}_{uv} = \frac{E_0}{\pi\theta_0^2}\exp\left(-\frac{u^2+v^2}{\theta_0^2}\right)\begin{bmatrix} -v\cot\theta_i(r_p+r_s) \\ 0 \end{bmatrix} \tag{B.51}$$

Finally, the reflected field distribution in the (u, v) domain for s-polarized beam is given by:

$$\vec{E}_{uv} = -\frac{E_0}{\pi\theta_0^2}v\cot\theta_i(r_p+r_s)\exp\left(-\frac{u^2+v^2}{\theta_0^2}\right)\vec{e}_y \tag{B.52}$$

We can recognize that there is a sign change in the expression of the field as compared to the case of p beam equation (B.40). The reflected field distribution in the (x, y) domain for s beam is therefore:

$$\mathcal{E}_{f\perp} = \frac{-E_0}{\pi\omega_f^2}\frac{y}{l_f}\exp\left(-\frac{x^2+y^2}{\omega_f^2}\right) \tag{B.53}$$

B.3 Reflection matrix as a function of (x, y) (equation (4.6))

We preliminary determine the expression of the reflected beam for specific case of p and s beam. Furthermore, this study can be generalized to and across other

cases of incident polarization states. For this purpose, we aim here to express the reflection matrix at focal plane as a function of (x,y) using the same lens transformation (Appendix E.2):

$$\bar{\bar{M}}_{x,y} = \frac{-i}{\lambda f}\iint_{-\infty}^{+\infty} \bar{\bar{M}}_{u,v}\ \exp[ik_0(xu+yv)]\,du\,dv \tag{B.54}$$

which can be also written as

$$\bar{\bar{M}}_{x,y} = I_1\begin{bmatrix} r_p & 0 \\ 0 & r_s \end{bmatrix} + I_2\begin{bmatrix} r'_p & 0 \\ 0 & r'_s \end{bmatrix} + I_3\frac{r_p+r_s}{\tan\theta_i}\begin{bmatrix} 0 & -1 \\ 1 & 0 \end{bmatrix} \tag{B.55}$$

where

$$I_1 = \frac{1}{\pi\theta_0^2}\iint_{-\infty}^{+\infty} \exp\left(-\frac{u^2+v^2}{\theta_0^2}\right)\exp[ik_0(xu+yv)]\,du\,dv \tag{B.56}$$

$$I_2 = \frac{1}{\pi\theta_0^2}\iint_{-\infty}^{+\infty} u\exp\left(-\frac{u^2+v^2}{\theta_0^2}\right)\exp[ik_0(xu+yv)]\,du\,dv \tag{B.57}$$

$$I_3 = \frac{1}{\pi\theta_0^2}\iint_{-\infty}^{+\infty} v\exp\left(-\frac{u^2+v^2}{\theta_0^2}\right)\exp[ik_0(xu+yv)]\,du\,dv \tag{B.58}$$

First we calculate

$$I_1 = \frac{1}{\pi\theta_0^2}\iint_{-\infty}^{+\infty} \exp\left(-\frac{u^2+v^2}{\theta_0^2}\right)\exp[ik_0(xu+yv)]\,du\,dv \tag{B.59}$$

For the sake of simplicity, we calculate each integral separately

$$\Leftrightarrow I_1 = \frac{1}{\pi\theta_0^2}\int_{-\infty}^{+\infty} \exp\left(\frac{-u^2}{\theta_0^2}+iuk_0x\right)du\int_{-\infty}^{+\infty} \exp\left(\frac{-v^2}{\theta_0^2}+ivk_0y\right)dv$$

In order to calculate both integrals, we write the exponent terms in form of a polynomial in u and v respectively

$$\Leftrightarrow I_1 = \frac{1}{\pi\theta_0^2}\int_{-\infty}^{+\infty} \exp\left\{\frac{-1}{\theta_0^2}\left(u-i\frac{\theta_0^2k_0x}{2}\right)^2-\frac{\theta_0^2k_0^2x^2}{4}\right\}du$$
$$\int_{-\infty}^{+\infty} \exp\left\{\frac{-1}{\theta_0^2}\left(v-i\frac{\theta_0^2k_0y}{2}\right)^2-\frac{\theta_0^2k_0^2y^2}{4}\right\}dv$$

The terms independent of u and v can be moved outside the integrals

$$\Leftrightarrow I_1 = \frac{1}{\pi\theta_0^2}\exp\left\{-\frac{\theta_0^2k_0^2x^2+\theta_0^2k_0^2y^2}{4}\right\} \int_{-\infty}^{+\infty}\exp\left\{\frac{-1}{\theta_0^2}\left(u-i\frac{\theta_0^2k_0x}{2}\right)^2\right\}du\int_{-\infty}^{+\infty}\frac{-1}{\theta_0^2}\left(v-i\frac{\theta_0^2k_0y}{2}\right)^2dv$$

Using $\int_{-\infty}^{+\infty} exp - ax^2\,dx = \sqrt{\pi/a},\ a>0$, we obtain

$$\Leftrightarrow I_1 = \frac{1}{\pi\theta_0^2}\exp\left\{-\frac{\theta_0^2k_0^2x^2+\theta_0^2k_0^2y^2}{4}\right\}\sqrt{\pi\theta_0^2}\sqrt{\pi\theta_0^2} \tag{B.60}$$

which is also

$$\Leftrightarrow I_1 = \exp\left\{-\frac{\theta_0^2k_0^2x^2+\theta_0^2k_0^2y^2}{4}\right\} \tag{B.61}$$

The angular mode divergence is given by $\theta_0 = \omega_0/f$ which is also $\lambda/(\pi\omega_f)$ with $\omega_0 = \lambda f/(\pi\omega_f)$. Using $\theta_0^2k_0^2/4 = 1/\omega_f^2$, we get

$$\Leftrightarrow I_1 = \exp\left\{-\frac{x^2+y^2}{\omega_f^2}\right\} \tag{B.62}$$

Similarly, we calculate I_2

$$I_2 = \frac{1}{\pi\theta_0^2}\iint_{-\infty}^{+\infty} u\exp\left(-\frac{u^2+v^2}{\theta_0^2}\right)\exp[ik_0(xu+yv)]\,du\,dv \tag{B.63}$$

We use method of separation of variables

$$I_2 = \frac{1}{\pi\theta_0^2}\int_{-\infty}^{+\infty} u\exp\left(\frac{-u^2}{\theta_0^2}+iuk_0x\right)du\int_{-\infty}^{+\infty}\exp\left(\frac{-v^2}{\theta_0^2}+ivk_0y\right)dv \tag{B.64}$$

After simplification

$$\Leftrightarrow I_2 = \frac{1}{\pi\theta_0^2}\int_{-\infty}^{+\infty} u\exp\left\{\frac{-1}{\theta_0^2}\left(u-i\frac{\theta_0^2k_0x}{2}\right)^2-\frac{\theta_0^2k_0^2x^2}{4}\right\}du \int_{-\infty}^{+\infty}\exp\left\{\frac{-1}{\theta_0^2}\left(v-i\frac{\theta_0^2k_0y}{2}\right)^2-\frac{\theta_0^2k_0^2y^2}{4}\right\}dv$$

which is also

$$\Leftrightarrow I_2 = \frac{1}{\pi\theta_0^2}\exp\left\{-\frac{\theta_0^2k_0^2x^2+\theta_0^2k_0^2y^2}{4}\right\} \int_{-\infty}^{+\infty} u\exp\left\{\frac{-1}{\theta_0^2}\left(u-i\frac{\theta_0^2k_0x}{2}\right)^2\right\}du \int_{-\infty}^{+\infty}\frac{-1}{\theta_0^2}\left(v-i\frac{\theta_0^2k_0y}{2}\right)^2 dv$$

Using $\int_{-\infty}^{+\infty} xexp-a(x-b)^2\,dx = b\sqrt{\pi/a}, a>0$

$$\Leftrightarrow I_2 = \frac{1}{\pi\theta_0^2}\exp\left\{-\frac{\theta_0^2k_0^2x^2+\theta_0^2k_0^2y^2}{4}\right\} i\frac{\theta_0^2k_0x}{2}\sqrt{\pi\theta_0^2}\sqrt{\pi\theta_0^2} \tag{B.65}$$

So we have

$$I_2 = i\frac{\theta_0^2k_0x}{2}\exp\left\{-\frac{\theta_0^2k_0^2x^2+\theta_0^2k_0^2y^2}{4}\right\} \tag{B.66}$$

The angular mode divergence is given by $\theta_0 = \omega_0/f$ which is also $\lambda/(\pi\omega_f)$ with $\omega_0 = \lambda f/(\pi\omega_f)$. Using $\theta_0^2k_0^2/4 = 1/\omega_f^2$ and $\theta_0^2k_0/2 = 2/k_0\omega_f^2 = 1/l_f$, we obtain

$$I_2 = \frac{ix}{l_f}\exp\left\{-\frac{x^2+y^2}{\omega_f^2}\right\} \tag{B.67}$$

We recall that

$$I_3 = \frac{1}{\pi\theta_0^2}\iint_{-\infty}^{+\infty} v\exp-\frac{u^2+v^2}{\theta_0^2}\exp ik_0(xu+yv)\,du\,dv = \frac{iy}{l_f}\exp\left\{-\frac{x^2+y^2}{\omega_f^2}\right\} \tag{B.68}$$

Using I_1, I_2 and I_3, the reflectivity Jones matrix is therefore given by

$$\bar{\bar{M}}_{x,y} = \begin{bmatrix} r_p & 0 \\ 0 & r_s \end{bmatrix} + i\frac{x}{l_f}\begin{bmatrix} r_p' & 0 \\ 0 & r_s' \end{bmatrix} + i\frac{y}{l_f}\frac{r_p+r_s}{\tan\theta_i}\begin{bmatrix} 0 & -1 \\ 1 & 0 \end{bmatrix} \tag{B.69}$$

Appendix C

Supplementary information to chapter 4 "Effect of confocal spatial filtering"

C.1 Spatial filtering with a single mode fiber (equation (4.8))

To illustrate the effect of confocal spatial filtering, we consider an input Gaussian beam $E_{0x,y}$ propagating through a single mode fiber which transmits only the fundamental mode TEM_{00}. The fiber filter function centered at $(x_0, y_0) = (0, 0)$ (the optical axis of the objective and that the fiber is displaced around) is a Gaussian distribution $E_{filter}(x - x_0, y - y_0) = exp - \frac{(x-x_0)^2+(y-y_0)^2}{w_f^2}$ of identical beam size ω_f as the input beam. In practice, the detected beam at the fiber front-end is the convolution output beam $E_{D0,0}$ with the guidance mode of the single mode fiber and is given by:

$$E_{D0,0}(x_0, y_0) = \iint_{-\infty}^{+\infty} E_{0x,y}(x, y) E_{filter}(x - x_0, y - y_0)\, dx\, dy \tag{C.1}$$

with $E_{0x,y} = \frac{-iE_0}{\pi\omega_f^2} \exp\left(-\frac{x^2+y^2}{\omega_f^2}\right)$. Therefore,

$$E_{D0,0}(x_0, y_0) = \frac{-iE_0}{\pi\omega_f^2} \iint_{-\infty}^{+\infty} \exp\left(-\frac{x^2 + y^2}{\omega_f^2}\right) \exp - \frac{(x - x_0)^2 + (y - y_0)^2}{w_f^2}\, dx\, dy \tag{C.2}$$

We start by writing the integral in simplified form by expanding expressions with exponents like the following

$$E_{D0,0}(x_0, y_0) = \frac{-iE_0}{\pi\omega_f^2} \iint_{-\infty}^{+\infty} \exp\left(-\frac{x^2 + y^2}{\omega_f^2}\right) \exp - \frac{(x^2 - 2x_0x + x_0^2) + (y^2 - 2yy_0 + y_0^2)}{w_f^2}\, dx\, dy \tag{C.3}$$

The terms independent of x and y can be moved outside the integrals

$$E_{D0,0}(x_0, y_0) = \frac{-iE_0}{\pi\omega_f^2} \exp\Big(-\frac{x_0^2 + y_0^2}{\omega_f^2}\Big) \iint_{-\infty}^{+\infty} \exp -\frac{2x^2 - 2x_0x - 2yy_0 + 2y^2}{w_f^2}\, dx\, dy \tag{C.4}$$

which is also

$$E_{D0,0}(x_0, y_0) = \frac{-iE_0}{\pi\omega_f^2} \exp\Big(-\frac{x_0^2 + y_0^2}{\omega_f^2}\Big) \iint_{-\infty}^{+\infty} \exp -2\frac{x^2 - x_0x - yy_0 + y^2}{w_f^2}\, dx\, dy \tag{C.5}$$

Now, we express the exponent as a form of a polynomial in x and y respectively

$$E_{D0,0}(x_0, y_0) = \frac{-iE_0}{\pi\omega_f^2} \exp\Big(-\frac{x_0^2 + y_0^2}{\omega_f^2}\Big) \iint_{-\infty}^{+\infty} \exp -2\frac{(x - x_0/2)^2 + (y - y_0/2)^2 - x_0^2/4 - y_0^2/4}{w_f^2}\, dx\, dy$$

Again, the constant factors can be taken outside the integral

$$E_{D0,0}(x_0, y_0) = \frac{-iE_0}{\pi\omega_f^2} \exp\Big(-\frac{x_0^2 + y_0^2}{\omega_f^2}\Big) \exp\Big(\frac{x_0^2 + y_0^2}{2\omega_f^2}\Big) \iint_{-\infty}^{+\infty} \exp -2\frac{(x - x_0/2)^2 + (y - y_0/2)^2}{w_f^2}\, dx\, dy$$

Therefore,

$$E_{D0,0}(x_0, y_0) = \frac{-iE_0}{\pi\omega_f^2} \exp\Big(-\frac{x_0^2 + y_0^2}{2\omega_f^2}\Big) \iint_{-\infty}^{+\infty} \exp -2\frac{(x - x_0/2)^2 + (y - y_0/2)^2}{w_f^2}\, dx\, dy \tag{C.6}$$

Using $\int_{-\infty}^{+\infty} exp - a(x-b)^2\, dx = \sqrt{\pi/a}, a > 0$, we obtain

$$E_{D0,0}(x_0, y_0) = \frac{-iE_0}{\pi\omega_f^2} \sqrt{\frac{\pi\omega_f^2}{2}} \sqrt{\frac{\pi\omega_f^2}{2}} \exp\Big(-\frac{x_0^2 + y_0^2}{2\omega_f^2}\Big) \tag{C.7}$$

After simplification

$$E_{D0,0}(x_0, y_0) = \frac{-iE_0}{\pi\omega_f^2} \frac{\pi\omega_f^2}{2} \exp -\Big(\frac{x_0^2 + y_0^2}{2\omega_f^2}\Big) \tag{C.8}$$

Finally, the convolution between the spatial field distribution at focal plane and the fiber Gaussian mode is given by:

$$E_{D0,0}(x_0, y_0) = \frac{-iE_0}{2} \exp\left(-\frac{x_0^2 + y_0^2}{2\omega_f^2}\right) \tag{C.9}$$

We conclude that the confocal filtering by convolution with a Gaussian mode leads to a broadening of the beam waist by a factor $\sqrt{2}$ and divide the field distribution by a factor 2.

C.2 Reflection matrix including confocal filtering (equation (4.9))

Here, we are interested in studying the effect of confocal spatial filtering on the reflection matrix. We recall that the reflectivity Jones matrix as a function of (x, y) is expressed as:

$$\bar{\bar{M}}_{x,y} = \begin{bmatrix} r_p & 0 \\ 0 & r_s \end{bmatrix} + i\frac{x}{l_f}\begin{bmatrix} r'_p & 0 \\ 0 & r'_s \end{bmatrix} + i\frac{y}{l_f}\frac{r_p + r_s}{\tan\theta_i}\begin{bmatrix} 0 & -1 \\ 1 & 0 \end{bmatrix} \tag{C.10}$$

For the sake of notation simplicity, we call GH and IF the terms responsible for the Goos-Hänchen and Imbert-Fedorov modes. We start our analysis by calculating the convolution of the GH term with the mode of the fiber:

$$GH = \iint_{-\infty}^{+\infty} i\frac{x}{l_f} \exp\left(-\frac{x^2 + y^2}{\omega_f^2}\right) \exp -\frac{(x - x_0)^2 + (y - y_0)^2}{w_f^2}\, dx\, dy \tag{C.11}$$

We use same calculation method as in equation (C.3), (C.4) and (C.5) in Appendix C.1

$$GH = \iint_{-\infty}^{+\infty} i\frac{x}{l_f} \exp\left(-\frac{x^2 + y^2}{\omega_f^2}\right) \exp -\frac{(x^2 - 2x_0x + x_0^2) + (y^2 - 2yy_0 + y_0^2)}{w_f^2}\, dx\, dy \tag{C.12}$$

The terms independent of x and y can be moved outside the integrals

$$\Leftrightarrow GH = \exp\left(-\frac{x_0^2 + y_0^2}{\omega_f^2}\right) \iint_{-\infty}^{+\infty} i\frac{x}{l_f} \exp -\frac{2x^2 - 2x_0x - 2yy_0 + 2y^2}{w_f^2}\, dx\, dy \tag{C.13}$$

which is also

$$\Leftrightarrow GH = \exp\left(-\frac{x_0^2 + y_0^2}{\omega_f^2}\right) \iint_{-\infty}^{+\infty} i\frac{x}{l_f} \exp -2\frac{x^2 - x_0x - yy_0 + y^2}{w_f^2}\, dx\, dy \tag{C.14}$$

Now, we express the exponent as a form of a polynomial in x and y respectively

$$\Leftrightarrow GH = \exp\Big(-\frac{x_0^2+y_0^2}{\omega_f^2}\Big)\iint_{-\infty}^{+\infty} i\frac{x}{l_f}\exp -2\frac{(x-x_0/2)^2+(y-y_0/2)^2-x_0^2/4-y_0^2/4}{w_f^2}\,dx\,dy \tag{C.15}$$

Again, the constant factors can be taken outside the integral

$$\Leftrightarrow GH = \exp\Big(-\frac{x_0^2+y_0^2}{\omega_f^2}\Big)\exp\frac{x_0^2+y_0^2}{2\omega_f^2}\iint_{-\infty}^{+\infty} i\frac{x}{l_f}\exp -2\frac{(x-x_0/2)^2+(y-y_0/2)^2}{w_f^2}\,dx\,dy \tag{C.16}$$

After simplification, we get

$$\Leftrightarrow GH = \exp\Big(-\frac{x_0^2+y_0^2}{2\omega_f^2}\Big)\iint_{-\infty}^{+\infty} i\frac{x}{l_f}\exp -2\frac{(x-x_0/2)^2+(y-y_0/2)^2}{w_f^2}\,dx\,dy \tag{C.17}$$

Using $\int_{-\infty}^{+\infty} xexp-a(x-b)^2\,dx = b\sqrt{\pi/a}, a>0$, we get

$$\Leftrightarrow GH = i\frac{x_0}{2l_f}\sqrt{\frac{\pi\omega_f^2}{2}}\sqrt{\frac{\pi\omega_f^2}{2}}\exp\Big(-\frac{x_0^2+y_0^2}{2\omega_f^2}\Big) \tag{C.18}$$

Finally,

$$GH = i\frac{x_0}{2l_f}\frac{\pi\omega_f^2}{2}\exp\Big(-\frac{x_0^2+y_0^2}{2\omega_f^2}\Big) \tag{C.19}$$

Similarly, the convolution of the Imbert-Fedorov term (IF) with the mode of the fiber is given by:

$$IF = \iint_{-\infty}^{+\infty} i\frac{y}{l_f}\exp\Big(-\frac{x^2+y^2}{\omega_f^2}\Big)\exp -\frac{(x-x_0)^2+(y-y_0)^2}{w_f^2}\,dx\,dy \tag{C.20}$$

After calculation, we can write

$$\Leftrightarrow IF = \iint_{-\infty}^{+\infty} i\frac{y}{l_f}\exp\Big(-\frac{x^2+y^2}{\omega_f^2}\Big)\exp -\frac{(x^2-2x_0x+x_0^2)+(y^2-2yy_0+y_0^2)}{w_f^2}\,dx\,dy \tag{C.21}$$

The terms independent of x and y can be moved outside the integrals

$$\Leftrightarrow IF = \exp\Big(-\frac{x_0^2+y_0^2}{\omega_f^2}\Big)\iint_{-\infty}^{+\infty} i\frac{y}{l_f}\exp -\frac{2x^2-2x_0x-2yy_0+2y^2}{w_f^2}\,dx\,dy \tag{C.22}$$

which is also

$$\Leftrightarrow IF = \exp\Big(-\frac{x_0^2+y_0^2}{\omega_f^2}\Big)\iint_{-\infty}^{+\infty} i\frac{y}{l_f}\exp -2\frac{x^2-x_0x-yy_0+y^2}{w_f^2}\,dx\,dy \tag{C.23}$$

We express the exponent as a form of a polynomial in x and y respectively

$$\Leftrightarrow IF = \exp\Big(-\frac{x_0^2+y_0^2}{\omega_f^2}\Big)\iint_{-\infty}^{+\infty} i\frac{y}{l_f}\exp -2\frac{(x-x_0/2)^2+(y-y_0/2)^2-x_0^2/4-y_0^2/4}{w_f^2}\,dx\,dy$$

Again, the constant factors can be taken outside the integral

$$\Leftrightarrow IF = \exp\Big(-\frac{x_0^2+y_0^2}{\omega_f^2}\Big)\exp\Big(\frac{x_0^2+y_0^2}{2\omega_f^2}\Big)\iint_{-\infty}^{+\infty} i\frac{y}{l_f}\exp -2\frac{(x-x_0/2)^2+(y-y_0/2)^2}{w_f^2}\,dx\,dy \tag{C.24}$$

After simplification, we can write

$$\Leftrightarrow IF = \exp\Big(-\frac{x_0^2+y_0^2}{2\omega_f^2}\Big)\iint_{-\infty}^{+\infty} i\frac{y}{l_f}\exp -2\frac{(x-x_0/2)^2+(y-y_0/2)^2}{w_f^2}\,dx\,dy \tag{C.25}$$

Using $\int_{-\infty}^{+\infty} x\exp -a(x-b)^2\,dx = b\sqrt{\pi/a}, a>0$

$$\Leftrightarrow IF = i\frac{y_0}{2l_f}\sqrt{\frac{\pi\omega_f^2}{2}}\sqrt{\frac{\pi\omega_f^2}{2}}\exp\Big(-\frac{x_0^2+y_0^2}{2\omega_f^2}\Big) \tag{C.26}$$

Finally,

$$IF = i\frac{y_0}{2l_f}\frac{\pi\omega_f^2}{2}\exp\Big(-\frac{x_0^2+y_0^2}{2\omega_f^2}\Big) \tag{C.27}$$

We conclude that the matrix of reflection including confocal spatial filtering is given by:

$$\bar{\bar{M}}_{Dx_0,y_0} = \begin{bmatrix} r_p & 0 \\ 0 & r_s \end{bmatrix} + i\frac{x_0}{2l_f}\begin{bmatrix} r_p' & 0 \\ 0 & r_s' \end{bmatrix} + i\frac{y_0}{2l_f}\frac{r_p+r_s}{\tan\theta_i}\begin{bmatrix} 0 & -1 \\ 1 & 0 \end{bmatrix} \tag{C.28}$$

C.3 Reflected field distribution for p (or s) polarized beam

C.3.1 Expression of the electric field after the fiber

We have shown previously that the reflected field distribution for p or s beam is given by:

$$\mathcal{E}_{f\perp} = \pm\frac{E_0}{\pi\omega_f^2}\frac{y}{l_f}\exp\left(-\frac{x^2+y^2}{\omega_f^2}\right) \tag{C.29}$$

After propagation in the optical spatial filter, we obtain

$$\mathcal{E}_D(x_0,y_0) = \pm\frac{E_0}{\pi\omega_f^2}\frac{y}{2l_f}\exp\left(-\frac{x_0^2+y_0^2}{2\omega_f^2}\right) \tag{C.30}$$

C.3.2 Intensity of the lobe maxima at cross-polarization (equation (4.12))

The cross-polarized intensity for the p (or s) incident light

$$I = |\,E_D(0,y_0)\,|^2 = \frac{|\,r_p + r_s\,|^2}{\tan^2\theta_i}\frac{y_0^2}{4l_f^2}\exp\left(-\frac{y_0^2}{\omega_f^2}\right) \tag{C.31}$$

To calculate the lobe maxima at cross-polarization, we use the first derivative method. Therefore,

$$\frac{dI}{dy_0} = 0 \Leftrightarrow \frac{y_0^2}{4l_f^2}\frac{-2y_0}{\omega_f^2}\exp\left(-\frac{y_0^2}{\omega_f^2}\right) + \frac{2y_0}{4l_f^2}\exp\left(-\frac{y_0^2}{\omega_f^2}\right) = 0 \tag{C.32}$$

The exponent term can be eliminated in equation (C.32)

$$\Leftrightarrow \frac{y_0^2}{4l_f^2}\frac{-2y_0}{\omega_f^2} + \frac{2y_0}{4l_f^2} = 0 \tag{C.33}$$

After factorization we get

$$\Leftrightarrow \frac{2y_0}{4l_f^2}\left(-\frac{y_0^2}{\omega_f^2}+1\right) = 0 \tag{C.34}$$

The common factor can be eliminated

$$\Leftrightarrow -\frac{y_0^2}{\omega_f^2} + 1 = 0 \tag{C.35}$$

The possible solutions for equation (C.35) are $y_0 = \pm\omega_f$. Therefore, the intensity of the reflected beam at cross-polarization reaches a maximum at the locations $y_0 = \pm\omega_f$, and is given by:

$$|\,E_D(0,y_0=\omega_f)\,|^2 = \frac{|\,r_p + r_s\,|^2}{\tan^2\theta_i}\frac{\omega_f^2}{4l_f^2}\exp\left(-\frac{\omega_f^2}{\omega_f^2}\right) \tag{C.36}$$

After simplification, we obtain

$$| E_D(0, y_0 = \omega_f) |^2 = \frac{1}{e} \frac{| r_p + r_s |^2}{\tan^2 \theta_i} \frac{\omega_f^2}{4 l_f^2} \tag{C.37}$$

which is also

$$| E_D(0, y_0 = \omega_f) |^2 = \frac{1}{4e} \frac{| r_p + r_s |^2}{\tan^2 \theta_i} \frac{\omega_f^2}{l_f^2} \tag{C.38}$$

Appendix D

Supplementary information to chapter 4 "Integrated intensity without confocal filtering (equation (4.11))"

Here, we aim to study the expected extinction ratio without confocal filtering. For simplification the effect of polarization leakage in polarizers is ignored. We start our analysis by defining the total integrated intensity at cross-polarization detected in wide field imaging or using a wide core multimode fiber,

$$P_F = \iint_{-\infty}^{+\infty} |\, \mathcal{E}_{0\ xy} \,|^2 \; dx\, dy \tag{D.1}$$

To illustrate what this means, let's consider an incident Gaussian beam of the type

$$\mathcal{E}_{0xy} = \frac{E_0}{\pi \omega_f^2} \; \exp\Big(- \frac{x^2 + y^2}{\omega_f^2} \Big) \tag{D.2}$$

The total integrated intensity is therefore given by:

$$\iint_{-\infty}^{+\infty} |\, \mathcal{E}_{0x,y} \,|^2 \; dxdy = \iint_{-\infty}^{+\infty} \frac{E_0^2}{\pi^2 \omega_f^4} \exp\Big(- 2\frac{x^2 + y^2}{\omega_f^2} \Big) dx\, dy \tag{D.3}$$

We separate the variables by moving all the y terms to one side and all the x terms to the other side

$$\Leftrightarrow \iint_{-\infty}^{+\infty} |\, \mathcal{E}_{0x,y} \,|^2 \; dxdy = \frac{E_0^2}{\pi^2 \omega_f^4} \int_{-\infty}^{+\infty} \exp\Big(- 2\frac{x^2}{\omega_f^2} \Big) dx \int_{-\infty}^{+\infty} \exp\Big(- 2\frac{y^2}{\omega_f^2} \Big) dy \tag{D.4}$$

Using $\int_{-\infty}^{+\infty} \exp -ax^2 \, dx = \sqrt{\pi/a}, a > 0$, we find that

$$\Leftrightarrow \iint_{-\infty}^{+\infty} |\, \mathcal{E}_{0x,y} \,|^2 \; dxdy = \frac{E_0^2}{\pi^2 \omega_f^4} \sqrt{\frac{\pi\ \omega_f^2}{2}} \sqrt{\frac{\pi\ \omega_f^2}{2}} = \frac{E_0^2}{\pi^2 \omega_f^4} \frac{\pi\ \omega_f^2}{2} = \frac{E_0^2}{2\pi \omega_f^2} \tag{D.5}$$

We consider now the cross-polarized reflected beam of the p/s beam:

$$\mathcal{E}_{f\perp} = \frac{\pm E_0}{\pi\omega_f^2}\frac{r_p + r_s}{\tan\theta_i}\frac{y}{l_f}\ \exp\left(-\frac{x^2+y^2}{\omega_f^2}\right) \tag{D.6}$$

Thus,

$$\iint_{-\infty}^{+\infty} |\,\mathcal{E}_{f\perp}\,|^2\,dxdy = \frac{E_0^2}{\pi^2\omega_f^4}\frac{|\,r_p + r_s\,|^2}{\tan^2\theta_i}\iint_{-\infty}^{+\infty}\frac{y^2}{l_f^2}\ \exp\left(-4\frac{x^2+y^2}{\omega_f^2}\right)dx\,dy \tag{D.7}$$

We simplify the expression of the integral by separation of variables

$$\iint_{-\infty}^{+\infty} |\,\mathcal{E}_{f\perp}\,|^2\,dxdy = \frac{E_0^2}{\pi^2\omega_f^4}\frac{|\,r_p + r_s\,|^2}{\tan^2\theta_i}\int_{-\infty}^{+\infty}\frac{y^2}{l_f^2}\ \exp\left(-2\frac{y^2}{\omega_f^2}\right)dy\int_{-\infty}^{+\infty}\exp\left(-2\frac{x^2}{\omega_f^2}\right)dx$$

Using $\int_{-\infty}^{+\infty}\exp -ax^2\,dx = \sqrt{\pi/a}$, and $\int_{-\infty}^{+\infty}x^2\exp -ax^2\,dx = 1/2\sqrt{\pi/a^3}, a>0$

$$\Leftrightarrow \iint_{-\infty}^{+\infty} |\,\mathcal{E}_{f\perp}\,|^2\,dxdy = \frac{E_0^2}{\pi^2\omega_f^4}\frac{|\,r_p + r_s\,|^2}{\tan^2\theta_i}\frac{1}{l_f^2}\frac{1}{2}\sqrt{\frac{\pi\ (\omega_f^2)^3}{2^3}}\sqrt{\frac{\pi\ \omega_f^2}{2}} \tag{D.8}$$

After simplification

$$\Leftrightarrow \iint_{-\infty}^{+\infty} |\,\mathcal{E}_{f\perp}\,|^2\,dxdy = \frac{E_0^2}{\pi^2\omega_f^4}\frac{|\,r_p + r_s\,|^2}{\tan^2\theta_i}\frac{1}{l_f^2}\frac{1}{2}\sqrt{\frac{(\omega_f^2)^2}{2^2}}\frac{\pi\ \omega_f^2}{2} \tag{D.9}$$

which is also

$$\Leftrightarrow \iint_{-\infty}^{+\infty} |\,\mathcal{E}_{f\perp}\,|^2\,dxdy = E_0^2\frac{|\,r_p + r_s\,|^2}{\tan^2\theta_i}\frac{1}{\pi^2\omega_f^4 l_f^2}\frac{1}{2}\frac{\omega_f^2}{2}\frac{\pi\ \omega_f^2}{2} \tag{D.10}$$

The total integrated intensity of the reflected beam at cross-polarization is therefore given by:

$$\iint |\,\mathcal{E}_{f\perp}\,|^2\,dxdy = \frac{E_0^2}{8\pi l_f^2}\frac{|\,r_p + r_s\,|^2}{\tan^2\theta_i} \tag{D.11}$$

After normalization, the maximum signal to expect from the cross-polarization without confocal configuration is:

$$\frac{\iint |\,\mathcal{E}_{f\perp}\,|^2\,dxdy}{\iint |\,\mathcal{E}_{0x,y}\,|^2\,dxdy} = \frac{1}{4}\left(\frac{\omega_f}{l_f}\right)^2\frac{|\,r_p + r_s\,|^2}{\tan^2\theta_i} \tag{D.12}$$

or

$$\frac{\iint |\,\mathcal{E}_{f\perp}\,|^2\,dxdy}{\iint |\,\mathcal{E}_{0x,y}\,|^2\,dxdy} = \frac{1}{2}\left(\frac{\omega_f}{l_f}\right)^2\frac{1+\cos\left(\varphi_p - \varphi_s\right)}{\tan^2\theta_i} \tag{D.13}$$

Appendix E

Supplementary information to chapter 4 "Polarization structure of higher-order Hermite-Gaussian laser beams"

E.1 Focusing of a Gaussian beam: solution as a function of u and v

Here, we use the same approach as in Appendix B.1 to calculate higher-order modal transformation of a polarized Gaussian propagating through a focusing lens. Here we want to show that under high NA condition, the electric field vectors get tilted in the focal region enabling the generation of a cross-polarization component and a longitudinal field component. The component along x corresponds to the dominant polarization. The y component i.s cross-polarization has a four lobes pattern separated by dark lines x and y. These findings was theoretically predicted in 1993 by W.L. Erikson [43]. He was actually able to provide the first experimental proof of the cross-polarization component. In his calculations, he solved the Maxwell equations for a paraxial Gaussian laser beam with a dominant polarization direction along x-axis. In our case, we assume that the incident beam propagates through a focusing lens, and is a Gaussian weighted superposition of plane waves propagating along an angular distribution $\vec{k}/k_0 = u\vec{x} + v\vec{y} + w\vec{k}_0/k_0$ narrowly centered around $\vec{k}_0$ with $k_0 = 2\pi/\lambda$. Each plane wave component is attached to a local incidence plane $(\vec{e}_x, \vec{e}_y, \vec{k}/k_0)$ such as that:

$$\overrightarrow{e_y} = \vec{k}/k_0 \times \vec{e}_z = \frac{1}{\sqrt{u^2+v^2}} \begin{bmatrix} u \\ v \\ w \end{bmatrix} \times \begin{bmatrix} 0 \\ 0 \\ 1 \end{bmatrix} = \frac{1}{\sqrt{u^2+v^2}} \begin{bmatrix} v \\ -u \\ 0 \end{bmatrix} \tag{E.1}$$

and

$$\overrightarrow{e_y} = (\vec{k}/k_0 \times \vec{e}_z) \times (\vec{k}/k_0) = \frac{1}{\sqrt{u^2+v^2}} \begin{bmatrix} v \\ -u \\ 0 \end{bmatrix} \times \begin{bmatrix} u \\ v \\ w \end{bmatrix}$$

we calculate the cross product of the two vectors

$$\overrightarrow{e_x} = \frac{1}{\sqrt{u^2+v^2}} \begin{bmatrix} -uw \\ -vw \\ u^2+v^2 \end{bmatrix} \tag{E.2}$$

To calculate the propagation of each plane wave through the focusing lens, we determine first the weights of x- and y- field-components, given by the weighted projections $(\vec{e}_x \cdot \vec{E}_{0uv})$ and $(\vec{e}_y \cdot \vec{E}_{0uv})$. We determine then the resulting field transverse field as:

$$\vec{E}_{uv} = (\vec{e}_x \cdot \vec{E}_{0uv})\vec{e}_x + (\vec{e}_y \cdot \vec{E}_{0uv})\vec{e}_y \tag{E.3}$$

Inserting Eq. (E.3) and into

$$\vec{E}_{uv} = \frac{1}{u^2+v^2}\left(\begin{bmatrix} -uw \\ -vw \end{bmatrix} \cdot \begin{bmatrix} E_x \\ E_y \end{bmatrix}\right)\begin{bmatrix} -uw \\ -vw \end{bmatrix} + \left(\begin{bmatrix} v \\ -u \end{bmatrix} \cdot \begin{bmatrix} E_x \\ E_y \end{bmatrix}\right)\begin{bmatrix} v \\ -u \end{bmatrix} \tag{E.4}$$

Calculating first the scalar product terms $(\vec{e}_x \cdot \vec{E}_{0uv})$ and $(\vec{e}_y \cdot \vec{E}_{0uv})$,

$$\vec{E}_{uv} = \frac{1}{u^2+v^2}(-uwE_x - vwE_y)\begin{bmatrix} -uw \\ -vw \end{bmatrix} + (vE_y - uE_x)\begin{bmatrix} v \\ -u \end{bmatrix} \tag{E.5}$$

which is also

$$\vec{E}_{uv} = \frac{1}{u^2+v^2}\begin{bmatrix} -uw(-uwE_x - vwE_y) + v(vE_x - uE_y) \\ -vw(-uwE_x - vwE_y) - u(vE_x - uE_y) \end{bmatrix} \tag{E.6}$$

After simplification, we get

$$\vec{E}_{uv} = \frac{1}{u^2+v^2}\begin{bmatrix} u^2w^2E_y + uvw^2E_y + v^2E_x - uvE_y \\ uvw^2E_x + v^2w^2E_y - uvE_x + u^2E_y \end{bmatrix} \tag{E.7}$$

Using $w^2 = 1 - u^2 - v^2$:

$$\vec{E}_{uv} = \frac{1}{u^2+v^2}\begin{bmatrix} (u^2E_x + uvE_y)(1-u^2-v^2) + v^2E_x - uvE_y \\ (uvE_x + v^2E_y)(1-u^2-v^2) - uvE_x + u^2E_y \end{bmatrix} \tag{E.8}$$

After calculation, we obtain

$$\Leftrightarrow \vec{E}_{uv} = \frac{1}{u^2+v^2}\begin{bmatrix} -(u^2E_x + uvE_y)(u^2+v^2) + u^2E_x + v^2E_x \\ -(uvE_x + v^2E_y)(u^2+v^2) + v^2E_y + u^2E_y \end{bmatrix} \tag{E.9}$$

Finally, the expression of a focused Gaussian beam in k-space is given by:

$$\vec{E}_{uv} = \begin{bmatrix} E_x(1-u^2) - uvE_y \\ E_y(1-v^2) - uvE_x \end{bmatrix} \tag{E.10}$$

E.2 Focusing of a Gaussian beam: solution as a function of x and y

Now, we want to express the result in x-space, for this reason we consider an incident Gaussian beam of the type

$$\frac{E_0}{\pi\theta_0^2}\exp\Big(-\frac{u^2+v^2}{\theta_0^2}\Big) \tag{E.11}$$

as defined in previous sections.Thus, the expression of the field in the focal region of a focused Gaussian beam $\vec{\mathcal{E}}_{fxy}$ is given by (Appendix ()):

$$\vec{\mathcal{E}}_{fxy} = \frac{-i}{\lambda f}\frac{E_0}{\pi\theta_0^2}\iint_{-\infty}^{+\infty}\vec{E}_{uv}\ \exp\Big(-\frac{u^2+v^2}{\theta_0^2}\Big)\exp[ik_0(xu+yv)]\,du\,dv \tag{E.12}$$

For the sake of simplicity, we calculate separately terms depending on u^2, v^2 and uv in the integral. Therefore, we define K_1, K_2 and K_3 as:

$$K_1 = \frac{E_0}{\pi\theta_0^2}\iint_{-\infty}^{+\infty}u^2\exp\Big(-\frac{u^2+v^2}{\theta_0^2}\Big)\exp[ik_0(xu+yv)]\,du\,dv \tag{E.13}$$

$$K_2 = \frac{E_0}{\pi\theta_0^2}\iint_{-\infty}^{+\infty}v^2\exp\Big(-\frac{u^2+v^2}{\theta_0^2}\Big)\exp[ik_0(xu+yv)]\,du\,dv \tag{E.14}$$

$$K_3 = \frac{E_0}{\pi\theta_0^2}\iint_{-\infty}^{+\infty}uv\exp\Big(-\frac{u^2+v^2}{\theta_0^2}\Big)\exp[ik_0(xu+yv)]\,du\,dv \tag{E.15}$$

We start by calculating K_1

$$K_1 = \frac{E_0}{\pi\theta_0^2}\iint_{-\infty}^{+\infty}u^2\exp\Big(-\frac{u^2+v^2}{\theta_0^2}\Big)\exp[ik_0(xu+yv)]\,du\,dv \tag{E.16}$$

For simplicity, we calculate each integral separately

$$K_1 = \frac{E_0}{\pi\theta_0^2}\int_{-\infty}^{+\infty}u^2\exp\Big(\frac{-u^2}{\theta_0^2}+iuk_0x\Big)du\int_{-\infty}^{+\infty}\exp\Big(\frac{-v^2}{\theta_0^2}+ivk_0y\Big)dv$$

which is also

$$\Leftrightarrow K_1 = \frac{E_0}{\pi\theta_0^2}\int_{-\infty}^{+\infty}u^2\exp\left\{\frac{-1}{\theta_0^2}\Big(u-i\frac{\theta_0^2k_0x}{2}\Big)^2-\frac{\theta_0^2k_0^2x^2}{4}\right\}du$$
$$\int_{-\infty}^{+\infty}\exp\left\{\frac{-1}{\theta_0^2}\Big(v-i\frac{\theta_0^2k_0y}{2}\Big)^2-\frac{\theta_0^2k_0^2y^2}{4}\right\}dv$$

The terms independent of u and v can be moved outside the integrals

$$\Leftrightarrow K_1 = \frac{E_0}{\pi\theta_0^2}\exp\left\{-\frac{\theta_0^2k_0^2x^2+\theta_0^2k_0^2y^2}{4}\right\} \int_{-\infty}^{+\infty} u^2\exp\left\{\frac{-1}{\theta_0^2}\left(u-i\frac{\theta_0^2k_0x}{2}\right)^2\right\}du \int_{-\infty}^{+\infty}\frac{-1}{\theta_0^2}\left(v-i\frac{\theta_0^2k_0y}{2}\right)^2 dv$$

Using $\int_{-\infty}^{+\infty} x^2 exp - a(x-b)^2\,dx = 1/2\sqrt{\pi/a^3} + b^2\sqrt{\pi/a}$ and $\int_{-\infty}^{+\infty} exp - a(x-b)^2\,dx = \sqrt{\pi/a}, a > 0$

$$\Leftrightarrow K_1 = \frac{E_0}{\pi\theta_0^2}\exp\left\{-\frac{\theta_0^2k_0^2x^2+\theta_0^2k_0^2y^2}{4}\right\}\sqrt{\pi\theta_0^2}(\frac{\theta_0^2}{2}-\frac{\theta_0^4k_0^2x^2}{4})\sqrt{\pi\theta_0^2} \tag{E.18}$$

which is also

$$K_1 = E_0(\frac{\theta_0^2}{2}-\frac{\theta_0^4k_0^2x^2}{4})\exp\left\{-\frac{\theta_0^2k_0^2x^2+\theta_0^2k_0^2y^2}{4}\right\} \tag{E.19}$$

The angular mode divergence is given by $\theta_0 = \omega_0/f$ which is also $\lambda/(\pi\omega_f)$ with $\omega_0 = \lambda f/(\pi\omega_f)$. Using $\theta_0^2k_0^2/4 = 1/\omega_f^2$ and $\theta_0^2k_0/2 = 2/k_0\omega_f^2 = 1/l_f$, we get

$$K_1 = E_0(\frac{1}{k_0l_f}-\frac{x^2}{l_f^2})\exp\left\{-\frac{x^2+y^2}{\omega_f^2}\right\} \tag{E.20}$$

Similarly we show that

$$K_2 = E_0(\frac{1}{k_0l_f}-\frac{y^2}{l_f^2})\exp\left\{-\frac{x^2+y^2}{\omega_f^2}\right\} \tag{E.21}$$

Now, let's calculate K_3

$$K_3 = \frac{E_0}{\pi\theta_0^2}\iint_{-\infty}^{+\infty} uv\exp\left(-\frac{u^2+v^2}{\theta_0^2}\right)\exp[ik_0(xu+yv)]\,du\,dv \tag{E.22}$$

We use the method of separation of variables

$$K_3 = \frac{E_0}{\pi\theta_0^2}\int_{-\infty}^{+\infty} u\exp\left(\frac{-u^2}{\theta_0^2}+iuk_0x\right)du \int_{-\infty}^{+\infty} v\exp\left(\frac{-v^2}{\theta_0^2}+ivk_0y\right)dv \tag{E.23}$$

which is also

$$\Leftrightarrow K_3 = \frac{E_0}{\pi\theta_0^2}\int_{-\infty}^{+\infty} u\exp\left\{\frac{-1}{\theta_0^2}\left(u-i\frac{\theta_0^2k_0x}{2}\right)^2-\frac{\theta_0^2k_0^2x^2}{4}\right\}du \int_{-\infty}^{+\infty} v\exp\left\{\frac{-1}{\theta_0^2}\left(v-i\frac{\theta_0^2k_0y}{2}\right)^2-\frac{\theta_0^2k_0^2y^2}{4}\right\}dv$$

The terms independent of u and v can be moved outside the integrals

$$\Leftrightarrow K_3 = \frac{E_0}{\pi\theta_0^2}\exp\left\{-\frac{\theta_0^2k_0^2x^2+\theta_0^2k_0^2y^2}{4}\right\} \int_{-\infty}^{+\infty} u\exp\left\{\frac{-1}{\theta_0^2}\left(u-i\frac{\theta_0^2k_0x}{2}\right)^2\right\}du \int_{-\infty}^{+\infty} v\frac{-1}{\theta_0^2}\left(v-i\frac{\theta_0^2k_0y}{2}\right)^2 dv$$

Using $\int_{-\infty}^{+\infty} x\exp -a(x-b)^2\,dx = b\sqrt{\pi/a}$

$$\Leftrightarrow K_3 = \frac{E_0}{\pi\theta_0^2}\exp\left\{-\frac{\theta_0^2k_0^2x^2+\theta_0^2k_0^2y^2}{4}\right\}\sqrt{\pi\theta_0^2}\sqrt{\pi\theta_0^2}\left(i\frac{\theta_0^2k_0x}{2}\right)\left(i\frac{\theta_0^2k_0y}{2}\right) \tag{E.24}$$

After simplification, we get

$$K_3 = -\left(\frac{\theta_0^2k_0xE_0}{2}\right)\left(\frac{\theta_0^2k_0y}{2}\right)\exp\left\{-\frac{\theta_0^2k_0^2x^2+\theta_0^2k_0^2y^2}{4}\right\} \tag{E.25}$$

The angular mode divergence is given by $\theta_0 = \omega_0/f$ which is also $\lambda/(\pi\omega_f)$ with $\omega_0 = \lambda f/(\pi\omega_f)$. Using $\theta_0^2k_0^2/4 = 1/\omega_f^2$ and $\theta_0^2k_0/2 = 2/k_0\omega_f^2 = 1/l_f$, we obtain

$$K_3 = -E_0\frac{x}{l_f}\frac{y}{l_f}\exp\left\{-\frac{x^2+y^2}{\omega_f^2}\right\} \tag{E.26}$$

Finally, the normalized expression of a focused Gaussian beam in x-space is given by:

$$\vec{\mathcal{E}}_{fxy} = \frac{-iE_0}{\pi\omega_f^2}\begin{bmatrix} E_x(1-\frac{1}{k_0l_f}+\frac{x^2}{l_f^2})+\frac{x}{l_f}\frac{y}{l_f}E_y \\ E_y(1-\frac{1}{k_0l_f}+\frac{y^2}{l_f^2})+\frac{x}{l_f}\frac{y}{l_f}E_x \end{bmatrix}\exp\left\{-\frac{x^2+y^2}{\omega_f^2}\right\} \tag{E.27}$$

and with convolution

$$\vec{\mathcal{E}}_D(x_0,y_0) = \frac{-iE_0}{\pi\omega_f^2}\begin{bmatrix} E_x(1-\frac{1}{k_0l_f}+\frac{x_0^2}{4l_f^2})+\frac{x_0}{2l_f}\frac{y_0}{2l_f}E_y \\ E_y(1-\frac{1}{k_0l_f}+\frac{y_0^2}{4l_f^2})+\frac{x_0}{2l_f}\frac{y_0}{2l_f}E_x \end{bmatrix}\exp\left\{-\frac{x_0^2+y_0^2}{2\omega_f^2}\right\} \tag{E.28}$$

There seems to be a discrepancy i.e factor 2 between our calculated cross-polarization component and Erikson formula [43].

E.3 Application to p- polarization (equation (4.13))

To illustrate the meaning of equation Eq. (E.28), let's consider the example of propagation of a p-polarized Gaussian beam through a lens i.e $E_x = 1$ and $E_y = 0$. Therefore,

$$\vec{\mathcal{E}}_D(x_0, y_0) = \frac{-iE_0}{\pi\omega_f^2}\begin{bmatrix}(1 - \frac{1}{k_0 l_f} + \frac{x_0^2}{4l_f^2})\\ \frac{x_0}{2l_f}\frac{y_0}{2l_f}\end{bmatrix} \tag{E.29}$$

Equation (E.29) show that under high NA condition, the electric field vectors get tilted in the focal region enabling the generation of a depolarization term along the y-axis.The component along the x-axis corresponds to the dominant polarization. At cross-polarization the field has a four lobes pattern separated by a dark lines x- and y-axes:

$$\mathcal{E}_D(x_0, y_0) = \frac{-iE_0}{\pi\omega_f^2}\frac{x_0}{2l_f}\frac{y_0}{2l_f}\exp\left\{-\frac{x_0^2 + y_0^2}{2\omega_f^2}\right\} \tag{E.30}$$

Furthermore, the intensity of the cross-polarized beam reaches a maximum at the locations $(x_0, y_0) = (\pm\omega_f, \pm\omega_f)$, and is given by:

$$|\, E_D(\pm\omega_f, \pm\omega_f)\,|^2 = \frac{\omega_f^2}{4l_f^2}\frac{\omega_f^2}{4l_f^2}\, exp - \frac{2\omega_f^2}{\omega_f^2} \tag{E.31}$$

Note that this expression is normalized to the maximum intensity I_0 of the dominant mode TEM_{00}, with $I_0 = E_0^2/(\pi\omega_f^2)^2$. After simplification, we obtain

$$|\, E_D(\pm\omega_f, \pm\omega_f)\,|^2 = \frac{1}{4e^2}(\frac{\omega_f}{2l_f})^4 \tag{E.32}$$

Appendix F

Supplementary information to chapter 5 "Evaluation of the Fresnel coefficient in the limit of small angles "

Here we use the general wave propagation convention $\exp(ikr - i\omega t)$. The general reflectivity coefficient are given for reflecting material of complex dielectric function $\widetilde{\epsilon}$ under incidence angle θ_i by the following [27]

$$r_p = \frac{\widetilde{\epsilon} cos\theta_i - \sqrt{\widetilde{\epsilon} - sin^2\theta_i}}{\widetilde{\epsilon} cos\theta_i + \sqrt{\widetilde{\epsilon} - sin^2\theta_i}} \tag{F.1}$$

and

$$r_s = \frac{cos\theta_i - \sqrt{\widetilde{\epsilon} - sin^2\theta_i}}{cos\theta_i + \sqrt{\widetilde{\epsilon} - sin^2\theta_i}} \tag{F.2}$$

For illustration for a silver mirror we have $\widetilde{\epsilon} = -41.062 + 0.51265i$ at wavelength $\lambda = 905\ nm$.
In the following we concentrate on total internal reflectivity case (i.e. metallic mirrors). We approximate in what follows $\widetilde{\epsilon} \cong -\epsilon$ and ϵ is a real and positive number $\gg 1$. With this definition we get

$$r_p = \frac{-\epsilon cos\theta_i - \sqrt{-\epsilon - sin^2\theta_i}}{-\epsilon cos\theta_i + \sqrt{-\epsilon - sin^2\theta_i}} \tag{F.3}$$

and

$$r_s = \frac{cos\theta_i - \sqrt{-\epsilon - sin^2\theta_i}}{cos\theta_i + \sqrt{-\epsilon - sin^2\theta_i}} \tag{F.4}$$

This is also

$$r_p = \frac{cos\theta_i + (i/\sqrt{\epsilon})\sqrt{1 + sin^2\theta_i/\epsilon}}{cos\theta_i - (i/\sqrt{\epsilon})\sqrt{1 + sin^2\theta_i/\epsilon}} \tag{F.5}$$

and

$$r_s = \frac{cos\theta_i + (i\sqrt{\epsilon})\sqrt{1 + sin^2\theta_i/\epsilon}}{cos\theta_i - (i\sqrt{\epsilon})\sqrt{1 + sin^2\theta_i/\epsilon}} \tag{F.6}$$

Now let us define a new parameter for notation convenience $u = \theta_i^2/2 \ll 1$, and develop in the small angle of incidence limit $\theta_i \ll 1$. We get

$$r_p \cong \frac{(1-u) + (i/\sqrt{\epsilon})(1 + u/\epsilon)}{cos\theta_i - (i/\sqrt{\epsilon})(1 + u/\epsilon)} \tag{F.7}$$

and

$$r_s \cong \frac{(1-u) + (i\sqrt{\epsilon})(1 + u/\epsilon}{(1-u) - (i\sqrt{\epsilon})(1 + u/\epsilon)} \tag{F.8}$$

The task now is to separate real and imaginary part.

$$r_p \cong \frac{(1-u)^2 - (1+u/\epsilon)^2/\epsilon}{(1-u)^2 + (1+u/\epsilon)^2/\epsilon} + 2i\frac{(1-u)(1+u/\epsilon)/\sqrt{\epsilon}}{(1-u)^2 + (1+u/\epsilon)^2/\epsilon} \tag{F.9}$$

and

$$r_s \cong \frac{(1-u)^2 - (1+u/\epsilon)^2\epsilon}{(1-u)^2 + (1+u/\epsilon)^2\epsilon} - 2i\frac{(1-u)(1+u/\epsilon)\sqrt{\epsilon}}{(1-u)^2 + (1+u/\epsilon)^2\epsilon} \tag{F.10}$$

Now we consider the situation $\epsilon \gg 1$ for which we get

$$r_p \cong (1-2/\epsilon) + \frac{2i}{\sqrt{\epsilon}}(1+u) \tag{F.11}$$

and

$$r_s \cong -(1-2/\epsilon) - \frac{2i}{\sqrt{\epsilon}}(1-u) \tag{F.12}$$

In terms of angles this is

$$r_p \cong (1-2/\epsilon) + \frac{2i}{\sqrt{\epsilon}}(1+\frac{\theta_i^2}{2}) \tag{F.13}$$

and

$$r_s \cong -(1-2/\epsilon) - \frac{2i}{\sqrt{\epsilon}}(1-\frac{\theta_i^2}{2}) \tag{F.14}$$

Both the first order of $1/\epsilon$ and u. These are useful formula for loss-free metallic reflectivity in the limit of small angles of incidence.

Appendix G

Supplementary information to chapter 5 "Jones Vectors and Matrices "

State of polarization	Jones Vector
Horizontal Linear Polarization	$\begin{bmatrix} 1 \\ 0 \end{bmatrix}$
Vertical Linear Polarization	$\begin{bmatrix} 0 \\ 1 \end{bmatrix}$
Linear polarization at +45°	$\frac{1}{\sqrt{2}}\begin{bmatrix} 1 \\ 1 \end{bmatrix}$
Linear polarization at −45°	$\frac{1}{\sqrt{2}}\begin{bmatrix} 1 \\ -1 \end{bmatrix}$
Right circular polarization	$\frac{1}{\sqrt{2}}\begin{bmatrix} 1 \\ -i \end{bmatrix}$
Left circular polarization	$\frac{1}{\sqrt{2}}\begin{bmatrix} 1 \\ i \end{bmatrix}$

Table G.1: Jones Vector for selected polarization states

Optical element	Jones matrix
Horizontal Linear Polarizer	$\begin{bmatrix} 1 & 0 \\ 0 & 0 \end{bmatrix}$
Vertical Linear Polarizer	$\begin{bmatrix} 0 & 0 \\ 0 & 1 \end{bmatrix}$
Linear polarizer at +45°	$\frac{1}{2}\begin{bmatrix} 1 & 1 \\ 1 & 1 \end{bmatrix}$
Linear polarizer at −45°	$\frac{1}{2}\begin{bmatrix} 1 & -1 \\ -1 & 1 \end{bmatrix}$
Left hand circular polarizer	$\frac{1}{\sqrt{2}}\begin{bmatrix} 1 & -i \\ i & 1 \end{bmatrix}$
Right hand circular polarizer	$\frac{1}{\sqrt{2}}\begin{bmatrix} 1 & i \\ -i & 1 \end{bmatrix}$

Table G.2: Jones Matrices for standard optical elements

Appendix H

Supplementary information to all chapters "Gaussian beam propagation"

All plane wave developments done in this thesis are based on the propagation convention $\exp(ikr - i\omega t)$. This applies also to the definition of Fresnel coefficients. The table below show some useful connections in Gaussian optics. ω_0 is the waist at back aperture and f the focal length.

Optical element	Jones matrix
Numerical aperture	$NA = \omega_0/f$
Connection between NA and aperture angle	$NA = \tan(\theta_0)$
in paraxial approximation	$NA = \theta_0$
Waist at focal plane	$\omega_f = \frac{\lambda}{\pi NA}$
Rayleigh length	$l_f = \frac{\lambda}{\pi NA^2}$
Wave vector	$k = \frac{2\pi}{\lambda}$
	$k\omega_0 = \frac{2}{NA}$
	$\frac{1}{\lambda f} = \frac{1}{\pi \omega_f \omega_0}$

Table H.1: Gaussian beam optical parameters

Appendix I

Summary of the present manuscript in french

I.1 Chapitre 1: Spectroscopie résonnante: la motivation d'aller au-delà de la limite de l'instrument

Dans les expériences de spectroscopie optique, il est crucial d'exciter un émetteur avec un laser très proche de son énergie de transition. Les expériences sous excitation résonante sont essentielles pour accéder aux propriétés intrinsèques optiques et de polarisation de spin d'une grande classe d'émetteurs [2–7]. L'exploitation de la polarisation croisée linéaire dans une configuration confocale a été utilisée avec succès dans les expériences de fluorescence résonante en champ sombre comme méthode pour supprimer la lumière laser diffusée, et améliorer d'avantage la résolution spatiale [8, 9]. Les expériences de fluorescence résonante permettent d'accéder à des informations cruciales sur le couplage lumière-matière, comme l'interaction d'un seul émetteur de photons avec son environnement [10], avec des cavités optiques [11] et permettent également l'étude des défauts uniques dans des matériaux atomiquement minces tels que WSe_2 [12]. La technique de microscopie confocal en champ sombre permet de développer des sources de photons uniques avec des degrés élevés d'indiscernabilité des photons [13–15] et une cohérence plus longue [16]. En pratique, la technique de suppression du laser à champ sombre n'est pas seulement un outil de spectroscopie, c'est aussi un élément clé de technologie quantique récente [17].

Malgré de nombreuses avancées basées sur des microscopes confocaux à rejet laser en polarisation croisée, les mécanismes physiques qui rendent ces expériences possibles ne sont pas bien compris, ce qui freine les progrès scientifiques dans ce domaine. Le facteur clé du mérite est la suppression du fond du laser d'excitation d'au moins six ordres de grandeur. En effet, une suppression par un facteur de 10^8 [18] jusqu'à 10^{10} (ce travail) a été mesurée. Mais cela est très surprenant car les miroirs et le séparateur de faisceau dans un tel système réduisent la limite d'extinction théorique à 10^3 et voire même 10^4.

Dans ce travail, nous expliquons la raison physique de l'augmentation géante du taux d'extinction jusqu'à sept ordres de grandeur qui rendent possible

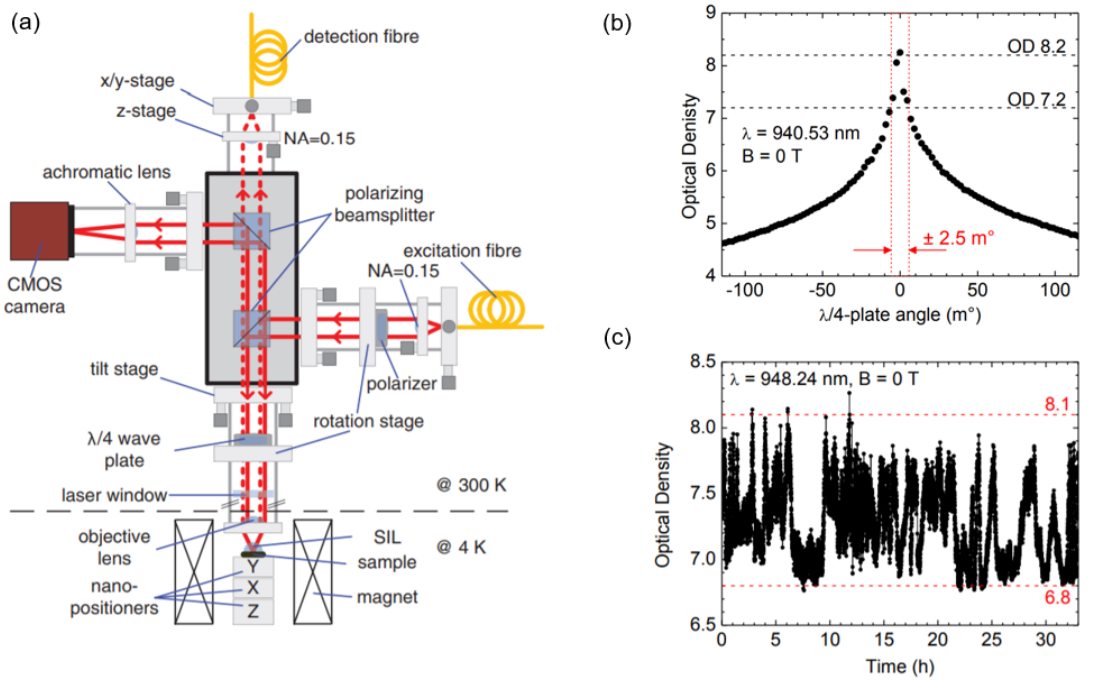

Figure I.1: *extrait de [18]* (a) Configuration du microscope pour des expériences de fluorescence par résonance sur un seul point quantique InGaAs. (b) Sensibilité de la suppression laser à l'angle de plaque quart d'onde. (c) Comportement à long terme. La densité optique, défini comme $OD = -log(1/T)$ avec transmission T, est tracé en fonction du temps. Le microscope est stable sur plusieurs heures avec un $OD > 6.8$.

la microscopie basée sur la suppression laser à champ sombre. Les mesures de fluorescence résonante sont généralement effectuées dans une géométrie d'épifluorescence [18], dans laquelle l'excitation laser et la collection de fluorescence sont obtenues à travers la même lentille de focalisation. Cela implique nécessairement l'utilisation d'un séparateur de faisceau orientant la lumière rétroréfléchie contenant la fluorescence vers le détecteur tel que représenté sur la figure I.1. Le laser rétroréfléchi est supprimé en faisant tourner une lame quart d'onde, commutant entre le mode rejet laser activé et désactivé au maximum. La mise en œuvre de ce schéma Fig. I.1(a) a démontré une suppression remarquablement élevée du fond d'excitation laser dépassant un facteur de 10^8 (Fig. I.1.(b) et (c)) correspondant à une densité optique OD=8. Fig. I.1.(b) montre que cette extinction géante dépend de l'angle de la lame quart d'onde et un changement de seulement quelques mdeg peut diminuer le niveau de rejet laser d'un ordre de grandeur. En d'autres termes, cela souligne la nécessité d'une résolution de rotation mdeg et d'un contrôle extrême de la polarisation pour pouvoir effectuer des expériences de fluorescence résonante sur des émetteurs quantiques.

Dans notre travail, nous identifions deux ingrédients clés qui expliquent l'amplification géante du rapport d'extinction de polarisation croisée: (i) une surface réfléchissante (c'est-à-dire le séparateur de faisceau) placée entre un polariseur et un analyseur, et (ii) un arrangement confocal. Nous démontrons

des taux d'extinction géants dans nos expériences pour différents miroirs (argent, or, diélectrique, cubes séparateurs de faisceaux) et polariseurs (Glan-Taylor, films minces de nanoparticules). Nous démontrons que derrière cette observation générale se cache la physique intrigante de l'effet Imbert-Fedorov [19, 20], qui dévie un faisceau lumineux réfléchi en fonction de son hélicité de polarisation. Nous découvrons qu'un arrangement confocal amplifie non seulement la visibilité de l'effet Imbert-Fedorov de façon spectaculaire, en le faisant passer de l'échelle nanométrique à l'échelle micrométrique, mais exploite également commodément la symétrie des modes Imbert-Fedorov nouvellement observés pour assurer que la composante du faisceau laser en polarisation croisée n'est pas couplé, ce qui explique la suppression presque complète du signal de fond laser. En d'autres termes, nous ne pouvons pas traiter les propriétés spatiales (c'est-à-dire modales) et de polarisation de la lumière séparément dans notre analyse au microscope confocal à champ sombre. En plus des nouveaux développements en microscopie à champ sombre, nos expériences fournissent des outils puissants pour comprendre le couplage spin-orbite de la lumière [21–23], dans le contexte plus large de la photonique topologique [22, 23].

Dans notre travail, nous mettons en place une expérience robuste et hautement reproductible et dérivons un formalisme classique pratique pour étudier ces effets remarquables à la croisée de l'optique quantique et de la photonique topologique.

La thèse est structurée comme suit, dans le chapitre I.2 nous introduisons l'arrangement confocal simplifié pour la mesure d'extinction de polarisation croisée est décrit dans la section. L'annulation de la fuite de polarisation est mesurée et discutée dans un premier modèle simplifié dans le chapitre I.3. La transformation modale d'un faisceau Gaussien réfléchi est analysée dans le chapitre I.4. L'imagerie directe de l'effet Imbert-Fedorov en état de polarisation circulaire de la lumière est présentée dans le chapitre I.5.

I.2 Chapitre 2: Configuration confocal avec extinction de polarisation

Les expériences sur les nanostructures semi-conductrices présentent des exigences difficiles sur le système optique. Les principaux critères de qualité sont la basse température, la haute résolution spatiale, la stabilité mécanique et l'accès au champ magnétique. Ces fonctionnalités pourraient être réalisées par le cryostat $attoCFM$ et $attoDRY1000$ du microscope confocal commercial d'attocube, comme illustré ci-dessous: Le $attoCFM$ à basse température a été conçu pour offrir à l'utilisateur une flexibilité maximale et un fonctionnement pratique. La tête du microscope est constituée de deux canaux principaux qui permettent l'excitation et la détection de signaux optiques. Le train optique du microscope comprend généralement un collimateur disponible dans le commerce, des filtres, des miroirs, des cubes séparateurs de faisceau, un objectif de microscope, un détecteur et des fibres monomodes sont utilisées comme trous d'épingle pour connecter le microscope à la source d'excitation et au canal de détection. Dans

Figure I.2: Le microscope confocal à fibre attocube *attoCFM* et Cryostat *attoDRY*1100. (1) Collimateur. (2) Fibre monomode couplée *FC/APC* vers / depuis le laser d'excitation ou le détecteur / spectromètre. (3) Position du séparateur de faisceau facilement commutable de l'extérieur. (4) Deux supports de filtre supplémentaires sur un cube séparateur de faisceau. (5) Options de diviseur de faisceau. (6) Facultatif: cube séparateur de faisceau polarisant. (7) Facultatif: cube séparateur de faisceau non polarisant. (8) Tiroir à filtre. (9) Miroirs Theta / phi pour chaque canal facilement réglables de l'extérieur.

notre cas, le microscope confocal avec sa conception complexe nous a permis d'atteindre un niveau de suppression de fond laser de 7 ordres de grandeur, à un facteur 10 du travail [18]. La figure I.3b est un tracé du rapport d'extinction de polarisation en fonction de l'angle de la lame quart d'onde qui est montée sur un rotateur de haute précision permettant une résolution de rotation de mdeg. En outre, nous définissons le rapport d'extinction de polarisation (ER) comme le rapport de la transmission minimale à la transmission maximale d'un faisceau laser incident dont la direction du champ électrique est soit parallèle (p-polarisée) ou orthogonale (s-polarisée) au plan d'incidence. Plus intéressant encore, nous avons effectué des mesures de fluorescence par résonance sur des points quantiques uniques avec un tel système. Fig. 2.2c correspondent à l'émission de points quantiques résonnants filtrés à travers un filtre spectral Fabry-Pérot à balayage de grande finesse. Il révèle deux pics latéraux qui s'éloignent du pic central avec des puissances d'excitation croissantes allant de 0.15 μW jusqu'à 6 μW. Le spectre de fluorescence résultant d'un système à deux niveaux entraîné par un champ incident résonant est connu sous le nom de triplet de Mollow [25].

Après cette brève explication du principe d'un microscope confocal, on peut

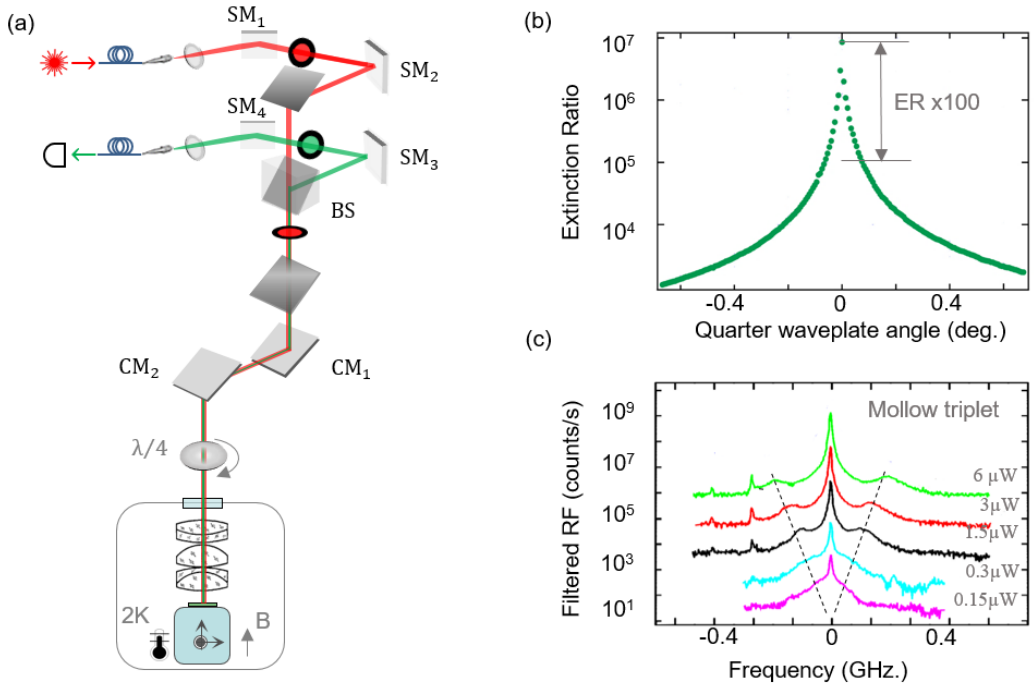

Figure I.3: (a) Dessin schématique de l'attoCFM basse température où l'échantillon est monté sur un nanopositionneur piézo-piloté x,y,z comme expliqué dans le texte. (SM), (CM) désignent les miroirs de direction et d'accouplement respectivement. ($\lambda/4$) plaque quart d'onde montée sur un rotateur piézoélectrique pour contrôler l'état de polarisation (b) Le rapport d'extinction tracé en fonction de l'angle de la lame quart d'onde. Dans une région angulaire étroite d'environ 30 mdeg, l'extinction dépasse six ordres de grandeur, démontrant finalement le besoin de rotateurs à entraînement piézoélectrique à haute résolution. (c) Triplet de Mollow d'un système à deux niveaux à excitation résonnante. Spectres mesurés du signal de fluorescence de résonance de points quantiques pour différentes puissances d'excitation à partir de 0.15 μW jusqu'à 6 μW. Les deux pics latéraux s'éloignent du pic central avec une puissance d'excitation croissante.

remarquer que les miroirs et les cubes séparateurs de faisceaux sont couramment utilisés pour des applications en microscopie confocale à fluorescence sous une source d'excitation à la fois résonante et non résonnante (photoluminescence). Par la suite, nous introduisons un agencement de microscope confocal optique simplifié pour améliorer de plusieurs ordres de grandeur l'extinction laser en polarisation croisée, rendant ainsi possible les expériences de fluorescence résonante.

Nous avons utilisé un arrangement confocal simplifié comme illustré dans la Fig. I.1 a, b afin de nous concentrer sur la physique la plus pertinente menant à un rejet laser extrême. Un faisceau laser à diode (1) à une longueur d'onde $\lambda = 905\ nm$ est lancé dans une fibre monomode (2). La lumière émerge de l'extrémité polie plate inclinée 4° avec un faisceau gaussien presque parfait

avec un rayon de taille de mode $\omega_0 = 2.5\ \mu m$ à $1/e^2$ de l'intensité maximale. Un objectif de microscope à diffraction limitée (3) d'ouverture numérique NA = 0.25 et de distance focale de $f = 26\ mm$ focalisé sur l'extrémité de la fibre collimate la lumière en un faisceau Gaussien de 3 mm de rayon de taille. Nous choisissons que le NA soit significativement plus grand que le demi-angle du faisceau divergent hors de la fibre afin de préserver la qualité Gaussienne du faisceau.

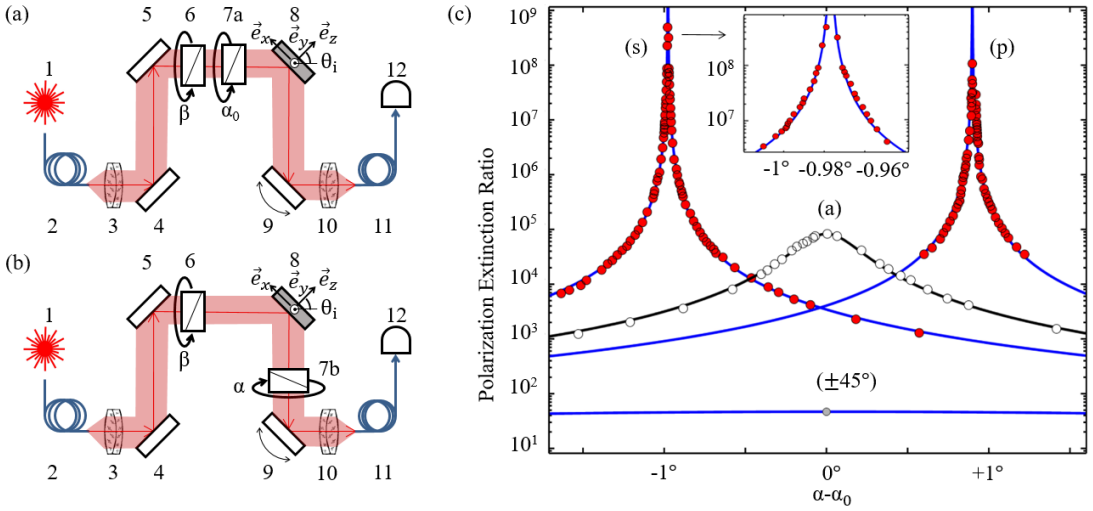

Figure I.4: (a) (b) Configuration d'extinction de polarisation croisée dans une configuration d'agencement de microscope confocal comme décrit dans le texte. (c) Rapport d'extinction de polarisation linéaire mesuré et modélisé pour le faisceau polarisé à la fois *p*- et *s*- autour des conditions de polarisation croisée obtenues en plaçant l'analyseur avant (panneau (a)) et après (panneau (b)) un protégé miroir argenté. Une amélioration d'extinction géante de plus de 3 ordres de grandeur est obtenue dans les configurations *s*- et *p*- avec la surface réfléchissante placée entre des polariseurs croisés. L'encart est un grossissement de l'extinction de polarisation proche du maximum pour la polarisation *s*. Un décalage angulaire de la localisation des maxima d'extinction est systématiquement trouvé pour les polarisations *s* et *p* par rapport à la référence. (±45°) Rapport d'extinction de polarisation linéaire mesuré et modélisé pour ±45° faisceau polarisé linéairement autour des conditions de polarisation croisée obtenues en plaçant l'analyseur après (panneau (b)) un miroir argenté.

Une paire de miroirs (4,5) montés sur des étages d'inclinaison à deux axes permet un guidage fin de l'axe du faisceau collimaté. Ensuite, le faisceau se déplace vers un polariseur linéaire (6) orienté à un angle β et monté sur un étage de rotation piézoélectrique tournant avec une résolution 20 μrad autour de l'axe optique. Le faisceau se déplace ensuite vers un miroir (8), élément clé de cette expérience, soit en passant d'abord par un polariseur d'analyse (Fig. I.1 a) orienté à un angle α_0 pour la mesure de contrôle (7a), ou en passant par l'analyseur orienté à un angle α après une surface réfléchissante pour l'expérience de test

(7b). Nous avons également monté l'analyseur sur un étage de rotation piézoélectrique. Le miroir (9) monté sur un étage piézoélectrique à deux axes qui permet d'orienter le faisceau dans un objectif de microscope (10) identique à (3) focalisant la lumière dans le coeur d'une fibre monomode (11) identique à (2) permettant le filtrage confocal modal et la détection optique (12) à l'autre extrémité du câble fibre de 5 m.

Cet arrangement confocal simule les composants essentiels d'un microscope confocal à fluorescence résonnante. Le plan de surface réfléchissant (8) à 45° d'incidence, définit l'état de polarisation standard p et s avec des projections le long de $\vec{e}_x$ et $\vec{e}_y$ respectivement. Les surfaces de test réfléchissantes en position (8) de la Fig. I.4a,b que nous avons utilisé dans ce travail sont des mirroirs commerciaux en argent protégé, aluminium, or évaporé, diélectrique, de Bragg à haute réflexion ainsi que les cubes séparateurs non polarisants. Toutes ces surfaces réfléchissantes sont généralement utilisées dans des microscopes confocaux à diffraction limitée. Les résultats étaient qualitativement très similaires pour toutes ces surfaces réfléchissantes. Nous choisissons de montrer ici les données mesurées avec des miroirs en argent uniquement, ceci à l'exception des données mesurées à des fins de comparaison sur une surface de verre réfléchissant de l'air (comme discuté au chapitre 4).

Nous discutons maintenant des mesures dans la configuration illustrée dans la figure I.4b, pour laquelle la surface de test réfléchissante est comprise entre le polariseur et l'analyseur. Tout d'abord, l'angle du polariseur β est ajusté près de 0 ou $\pi/2$, respectivement pour p ou s polarisation, tout en définissant l'angle de l'analyseur α près de la polarisation croisée à $\beta \pm \pi/2$. Ensuite, le polariseur et l'analyseur sont tournés finement pour atteindre l'extinction maximale aux valeurs β et α respectivement. Une fois l'optimisation est atteinte, β reste intacte et l'analyseur dans son rotateur est ensuite placé avant la surface réfléchissante juste après le polariseur pour notre mesure d'extinction de contrôle (Fig.I.4a). L'angle de l'analyseur doit alors être ajusté à une nouvelle valeur α_0 afin de récupérer l'extinction nominale maximale inhérente aux polariseurs; α_0 définit alors la référence p ou s. Les valeurs d'extinction mesurées en fonction de l'angle de l'analyseur α en référence à α_0 sont représentées sur la Fig. I.4c pour la mesure de contrôle (Fig. I.4a) ainsi que pour les polarisations p et s dans la configuration (Fig. I.4b). Deux observations frappantes ressortent. (i) Pour tous les réflecteurs testés indiqués ci-dessus, le rapport d'extinction obtenu de cette manière a été amélioré au-delà de 10^8 lorsque le miroir de test est compris entre le polariseur et l'analyseur, réduisant ainsi considérablement la fuite de polarisation des polariseurs. (ii) L'angle de l'analyseur pour l'extinction maximale est décalé de α_0 de $+0.898°$ et $-0.977°$ respectivement pour les polarisations p et s, un écart angulaire significatif étant donné notre résolution d'environ 10^{-3} deg. Dans le chapitre I.3, nous présentons une première explication de ces deux observations frappantes.

I.3 Chapitre 3: Les origines physiques de l'annulation de fuite de polarisation

Intuitivement, la réduction significative du champ de fuite de polarisation doit trouver son origine dans un effet d'interférence destructeur. Le premier défi pour trouver une réponse à notre problème est de proposer un modèle de fuite de polarisation. En effet, de nombreuses facteurs entraînent des fuites de polarisation telles que la diffusion de la lumière, le désalignement, et des erreurs lors du processus de fabrication des polariseurs croisés. L'hypothèse que nous faisons sur l'origine physique de la fuite de polarisation est qu'elle est due à une diffusion cohérente sans perte telle que les inclusions de diffusion de Rayleigh dans le cristal. En particulier, lorsque la lumière traverse une feuille polarisante constituée de chaînes de nanoparticules, elle interagit avec le milieu et cela provoque la diffusion de la lumière. Les photons avec une direction de polarisation le long des chaînes sont fortement absorbés, alors que l'absorption est faible pour les photons avec une direction de polarisation perpendiculaire à ceux-ci. L'absorption fait vibrer les nanoparticules qui réémettent des photons dans des directions aléatoires, mais avec la même fréquence et la même longueur d'onde. La diffusion de Rayleigh est un type d'interaction de diffusion cohérente qui fait que la lumière transmise est $(\pi/2)$ déphasée avec le faisceau lumineux initial. Dans cette interaction, l'énergie des particules diffusantes n'est pas modifiée. et la fuite doit être invariante sur une rotation angulaire arbitraire autour de l'axe optique. Dans notre cas la fuite nominale mesurée est $(1.5 \pm 0.5) \times 10^5$ (voir Fig. I.4c). On note que notre formalisme peut également être étendu aux polariseurs circulaires.

Après un long mais simple calcul (équation (3.6), Annexe A.3), nous déterminons l'intensité lumineuse juste après l'analyseur. Parce que la surface réfléchissante a des composantes réelles et imaginaires des coefficients de Fresnel, on montre que pour une " valeur suffisamment petite " de fuite on peut toujours trouver un choix des angles α, β qui conduit à une annulation parfaite de la fuite indésirable. Ceci est toujours vrai dans des conditions de réflexion interne totale ce qui est le cas d'un miroir métallique dans le domaine visible et infrarouge et pour un cube séparateur de faisceau typique. Une «valeur suffisamment petite» de dépolarisation pour obtenir une annulation parfaite signifie dans le cadre de notre travail typiquement $< 6 \times 10^{-3}$ lors de l'utilisation d'un miroir argenté comme nous nous l'avons dérivés dans le texte. La surface de test réfléchissante en combinaison avec la rotation des polariseurs agit pour interférer de manière destructive avec la fuite de polarisation sans perte invariante de rotation résiduelle inhérente même aux meilleurs polariseurs linéaires commerciaux. Inversement, pour une surface purement diélectrique un tel verre (c'est-à-dire BK7) réfléchissant du côté air, pour lequel les coefificents de Fresnel pour p et s sont tous deux réels, aucune annulation de fuite de polarisation complète n'était possible.

Pour avoir une meilleure idée des paramètres pertinents en pratique pour l'annulation presque parfaite de la fuite de polarisation, nous illustrons les mesures complètes et le modèle dans la Fig. I.4 qui sont obtenues en utilisant

l'équation (3.6) et en tenant compte de manière convaincante de l'amplification d'extinction de polarisation croisée et du léger décalage de rotation du polariseur et de l'analyseur nécessaire pour l'atteindre. Pour un miroir argenté parfait et une fuite de polarisation de 10^5 on évalue un taux de chromaticité de $0.0019°/nm$ pour une longueur d'onde autour de $\lambda = 905\ nm$. Dans cet exemple particulier, en gardant l'angle de l'analyseur à la valeur d'extinction maximale de 905 nm, la longueur d'onde pourrait être décalée jusqu'à $\pm 10\ nm$ tout en maintenant l'extinction à un niveau $> 10^7$.

À ce stade, nous avons pu conclure notre travail ici car nous avons pu expliquer de manière convaincante toutes les caractéristiques de l'extinction de polarisation renforcée. Notre analyse a cependant occulté jusqu'à présent un point crucial, à savoir le fait expérimental que l'annulation de fuite n'était mesurable que dans un agencement confocal, point qui sera élucidé dans les chapitres suivants. Plus précisément, l'analyse que nous avons menée conduisant au résultat principal dans l'équation (3.6) jusqu'à présent a été faite uniquement pour une onde plane pour laquelle le formalisme de la matrice de Jones est valide. En réalité cependant, la taille finie du faisceau laser Gaussien collimaté impose une distribution d'onde angulaire finie autour de l'angle d'incidence sur le miroir [29]. Les coefficients de Fresnel pour p et s deviennent alors une fonction de la distribution angulaire [29]. Ceci, comme nous le verrons, conduit à des effets de dépolarisation géométriques importants sous forme de nouveaux modes optiques limitant l'extinction totale à la plage 10^4. Nous verrons qu'une disposition confocale filtre les modes de dépolarisation et que le résultat de ce chapitre se révèle fortuitement exploitable.

I.4 Chapitre 4: Transformation modale de la réflectivité d'un faisceau Gaussien polarisé

Pour expliquer l'origine du rapport de réjection de polarisation étonnamment élevé $> 10^8$, nous avons effectué une imagerie par balayage x, y de l'intensité détectée dans des conditions de polarisation croisée. L'imagerie peut être réalisée en balayant un miroir (9) ou en balayant la position spatiale de la fibre collectrice dans le plan focal de l'objectif de focalisation (Fig. I.4b). Dans l'absence de surface réfléchissante entre l'analyseur et le polariseur en polarisation croisée, à savoir la configuration de référence de la Fig. I.4a, les mesures de la Fig. I.5a, b (rangée du haut) montrent un mode pur TEM_{00} Gaussien champ atténué de 8.3×10^4 et 9.6×10^4 pour p et s faisceau polarisé, respectivement. Ce niveau est attendu pour les spécifications de fuite du polariseur. En revanche, lorsque nous plaçons l'analyseur après la surface de test réfléchissante, les mesures montrent que le mode se divise en deux lobes répartis le long de $\vec{e}_y$ et situés au-dessus et au-dessous du plan de réflectivité. Dans cette configuration à polarisation croisée, on trouve un «trou» d'intensité à l'emplacement du centre de la fibre optique. Là, l'extinction d'intensité est légèrement supérieure à 10^8, un facteur 100 de notre limite de détection de configuration réelle.

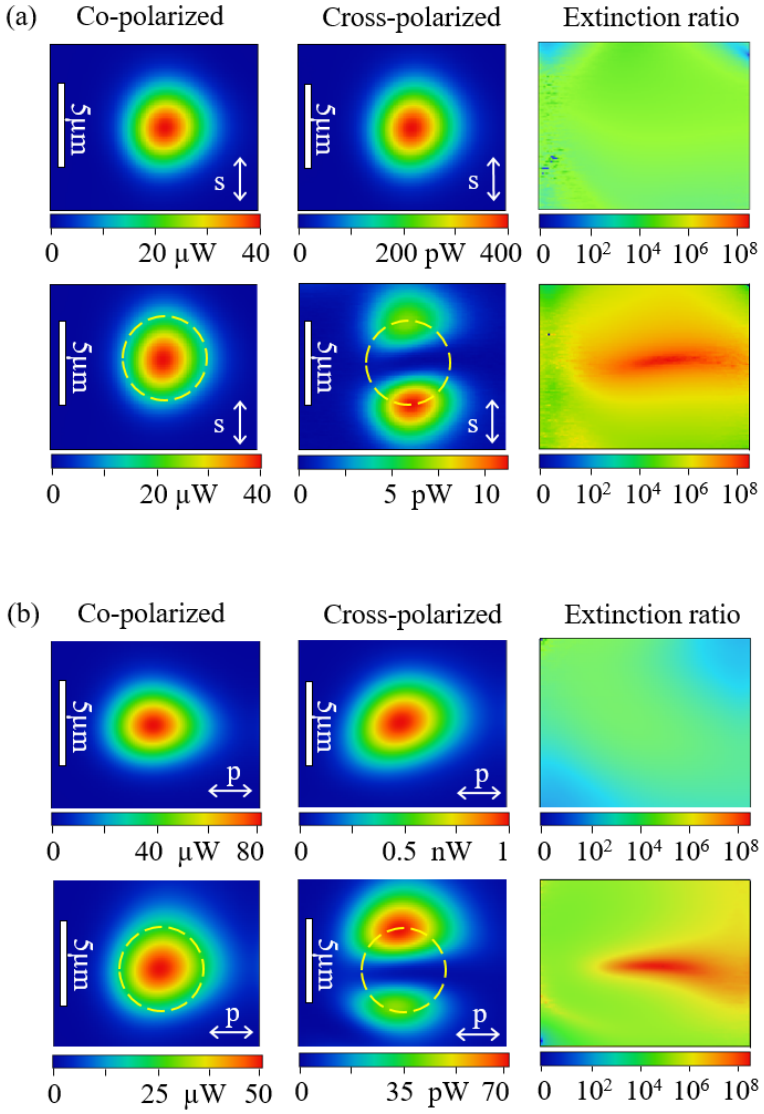

Figure I.5: Cartographie confocale du faisceau laser s (a) et p (b) en copolarisation et polarisation croisée à l'aide d'un miroir de balayage (9). Les lignes supérieure et inférieure des figures sont des mesures avec l'analyseur placé avant (Fig. I.4 a) et après (Fig. 2.3 b) la surface réfléchissante de test respectivement, en s polarisation et p polarisation (panneaux a et b). Nous traçons la carte du taux d'extinction en divisant, pixel par pixel, le co-avec les données de polarisation croisée. En polarisation croisée, un découpage modal le long de $\vec{e}_y$ au-dessus et au-dessous du plan d'incidence est observé à la fois pour les polarisations s et p. Le cercle en pointillé est le niveau d'intensité $1/e$ de la distribution Gaussienne résultant de la convolution confocale entre le point focalisé et le mode de fibre collectrice. L'emplacement des maxima de la division modale se trouve exactement sur ce cercle. Le diamètre de ce cercle donne également le diamètre de taille de la tache focale non alambiquée à $1/e^2$ focalisé sur l'extrémité de la fibre collectrice. La barre blanche verticale représente 5 μm.

Pour avoir une idée de la transformation modale mesurée pour p et s, nous avons mesuré et montré sur les Fig. I.6 et Fig. I.7 l'évolution de la lumière confocale cartes d'intensité pour différents angles de rotation de l'analyseur variation $\delta\alpha$ autour du mode divisé symétriquement. Fig. I.6d et I.7d montrent quantitativement pour les polarisations p et s les positions mesurées des décalages de pics de faisceaux le long de $\vec{e}_y$ et la division au-dessus et sous le plan d'incidence en fonction de $\delta\alpha$. Nous avons observé un comportement très similaire pour les cubes séparateurs de faisceaux généralement utilisés dans la configuration de fluorescence résonnante, comme dans la référence [8, 9, 16, 18], à la différence cependant que ce chiffre équivalent semble plutôt reflété par rapport à l'axe $\Delta y = 0$. Dans tous les cas, une telle distribution d'intensité à lobes séparés rappelle beaucoup un mode TEM_{01} Hermite-Gaussien.

Les figures I.6c et I.7c montrent après une inspection minutieuse que les minima d'intensité ou maxima d'extinction ne se produisent pas exactement à $y = 0$ mais sont plutôt très légèrement décalés symétriquement le long de y pour les deux la polarisation p et s. Cela signifie qu'il n'y a pas une seule position de l'emplacement de fibre y qui puisse conduire à une extinction maximale pour les polarisations p et s en même temps. Ceci est également clairement visible sur la figure I.4c pour laquelle l'extinction est au-delà de 10^9 pour la polarisation s et 10^8 pour p dans cette mesure particulière. Cette observation suggère clairement que les nouveaux modes le long de y semblent contribuer à stimuler l'extinction bien au-delà du niveau de 10^8. Nous avons atteint un niveau record de 10^{10} pour lequel le facteur limitant était le bruit sombre de notre détecteur. Le défi dans une telle expérience est d'avoir un rotateur de polarisation qui permet un pas avec des angles de rotation suffisamment petits. À ce stade, nous devons découvrir pourquoi (i) la disposition confocale permet l'amélioration dramatique de l'extinction comme le montre la Fig. I.4c, et (ii) pourquoi le faisceau se déplace et se sépare en polarisation croisée en Fig. I.5(rangée du bas) et ceci toujours au-dessus et au-dessous du plan d'incidence.

Pour répondre à ces questions, nous avons d'abord modéliser la distribution spatiale du champ au plan focal de la lentille de focalisation juste avant la fibre optique monomode collectrice, puis utiliser la fibre collectrice comme fonction de filtre Gaussien confocal portant la lumière vers le détecteur. Dans l'approximation paraxiale, la lentille de focalisation transforme chaque champ d'onde plane de la distribution angulaire en une densité de champ dans la focale plan, donc le faisceau atteignant le plan focal à la distance f résulte d'une superposition cohérente de toutes ces composantes focalisées (Annexe B.2). Un tel problème a été modélisé pour une distribution de champ Gaussien dans [31] par Aiello et Woerdman. Nous en tirons ici une version simplifiée décrivant de manière pratique la physique essentielle nécessaire pour modéliser nos observations. Lorsque le faisceau se réfléchit sur la surface de test, chaque composante d'onde plane acquiert un coefficient de réflexion de Fresnel. Nous montrons que la matrice de réflectivité de Jones transforme un mode Gaussien parfait incident, tel que l'équation (4.2), en la somme de TEM_{00}, TEM_{01} et TEM_{10} Hermite-Gauss

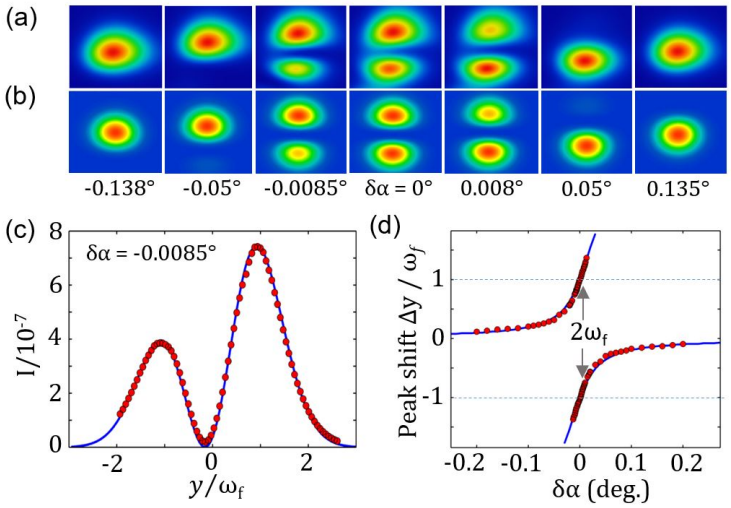

Figure I.6: Faisceau Gaussien p polarisé réfléchi par un miroir argenté. Évolution mesurée (a) et simulée (b) de la cartographie d'imagerie confocale modale par extinction maximale (c) pour différents angles d'analyseur $\delta\alpha$ comme expliqué dans le texte. En (d), les positions de décalage de crête et de division du faisceau sont indiquées en unités de taille de faisceau ω_f que nous avons modélisé pour notre miroir argenté $\Delta = 102.48°$ et une fuite de $1/b^2 = 8.3 \times 10^4$

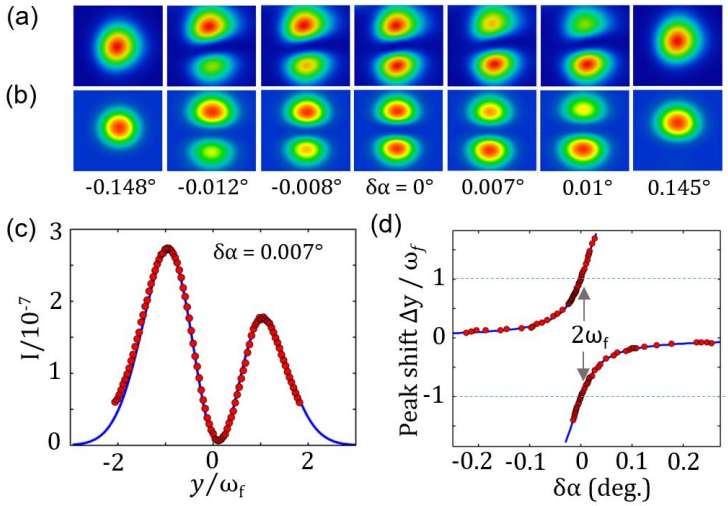

Figure I.7: Faisceau Gaussien s polarisé réfléchi par un miroir argenté. Évolution mesurée (a) et simulée (b) de la cartographie d'imagerie confocale modale par extinction maximale (c) pour différents angles d'analyseur $\delta\alpha$ comme expliqué dans le texte. En (d), les positions de décalage de crête et de division du faisceau sont indiquées en unités de taille de faisceau ω_f que nous avons modélisé pour un miroir argenté $\Delta = 100.7°$ et une fuite de $1\ /\ b^2 = 9.6 \times 10^4$

modes. Les indices pour TEM $_{nm}$ indiquent respectivement le nombre de nœuds. Le premier terme est la réflectivité normale de la surface de test que nous avons utilisée dans la première partie de cet article. Le second terme est responsable de la génération d'un mode TEM_{10} le long du plan d'incidence. Ce terme est

en fait responsable de l'effet Goos-Hänchen [32], car il a son origine physique dans la dispersion angulaire des termes de réflectivité à θ_i. Ici les différentes ondes planes les composants acquièrent des phases légèrement différentes lors du déplacement du faisceau dans le plan d'incidence. Comme cette matrice est diagonale, l'effet Goos-Hänchen fait ne contribue pas à la dépolarisation dans le cas d'une polarisation p ou s parfaite. Le troisième terme, le plus pertinent pour ce travail, est chargé de générer un mode TEM_{01} hors plan d'incidence avec deux lobes le long de l'axe y. Ce terme est la physique responsable de l'effet Imbert-Fedorov [19, 20, 22, 38] connu pour dévier un faisceau lumineux réfléchi au-dessus ou au-dessous du plan d'incidence en fonction de son hélicité de polarisation à droite ou à gauche. Notre calcul détaillé dans ce travail montre que ce terme provient purement de projections géométriques dans lesquelles le déphasage progressif gagné par chaque composante d'onde plane lors de la réflexion, se résume à une matrice diagonale croisée qui mélange les phases p et s composantes d'onde plane réfléchies décalées. Par conséquent, ce terme est responsable d'une dépolarisation induite par réflectivité intrinsèque pour p et s polarisation même en utilisant des polariseurs idéalement parfaits. En raison de la nature de projections purement géométriques de l'argumentation, le lien entre l'effet Imbert-Fedorov, la phase de Berry et l'effet spin-Hall de la lumière est discuté dans la littérature [22, 38]. Nous pouvons voir à présent à partir d'un argument de symétrie que notre arrangement confocal améliore l'extinction de la polarisation croisée. Sans l'arrangement confocal, l'extinction aurait été naturellement limitée dans la gamme 10^4 dans notre expérience comme nous le verrons après dans le texte.

Par ailleurs, nous avons exprimés la distribution de champ transmise par le polariseur, le miroir et l'analyseur à l'ouverture arrière de la lentille de focalisation en utilisant la transformée de Fourier (4.6). Après quelques calculations algèbriques (Annexe B.2), nous obtenons le champ de polarisation croisée pour la lumière incidente p (s). Un résultat important se dégage, à savoir que l'objectif amplifie considérablement le champ du mode Imbert-Fedorov. Il est facile de montrer que le facteur d'amplification de l'intensité lumineuse est ω_0^2/ω_f^2. Dans notre cas, nous obtenons une amplification de $3mm/2.5\mu m = 1200$. C'est la raison pour laquelle nous pouvons détecter ce mode si clairement dans une configuration confocale. L'autre paramètre physique essentiel qui régit l'intensité du champ du mode Imbert-Fedorov est la somme $r_p + r_s$ donnée par le matériau reflétant les propriétés. Nous concluons que la cartographie des champs de mode Imbert-Fedorov dans une configuration de microcopie confocale fournit un accès direct et sensible à l'amplitude et aux phases de réflectivité différentielle d'une surface réfléchissante.

Ce résultat se révèle être dans un contexte différent dans le travail perspicace et pionnier d'Aiello *et al.* [39]. Dans leur travail, les auteurs ont fourni dans une approximation paraxiale, une solution analytique complète pour la distribution de champ d'un faisceau Gaussien monomode réfléchi par un miroir. Le résultat essentiel de notre travail est que l'arrangement confocal transforme la taille du

faisceau collimaté ω_0 et la longueur de Rayleigh l et de la distribution du champ Aiello *et al.* [39] au plan miroir, en l_f et ω_f dans notre cas. Ce résultat semble bénin au début, mais comme évoqué plus haut, il s'agit d'une amplification importante de l'intensité du mode faible proportionnellement à ω_0^2/ω_f^2. Aiello *et al.* [39] a montré que c'est la taille finie du faisceau à la surface réfléchissante qui est responsable des termes de champ supplémentaires qui affectent le mode Gaussien initial. De nos travaux, il devient maintenant clair ici qu'en utilisant un arrangement confocal, la taille du faisceau au niveau du miroir n'est pas pertinente pour nos mesures mais plutôt la taille du faisceau focalisé qui joue un rôle crucial. Ce fait, au départ non intuitif, fournit un avantage précieux pour explorer expérimentalement la géométrie de polarisation croisée avec une sensibilité suffisante et une résolution spatiale très fine. En particulier, l'extinction de polarisation croisée à extinction élevée est apparentée à la «procédure de mesure faible» d'Aharonov *et al.* [40,41] que nous étendons ici à un agencement confocal permettant l'avantage supplémentaire de la résolution spatiale. La littérature récente [22] fournit une interprétation de la dépolarisation comme résultant d'une interaction spin-orbite efficace de la lumière se produisant à la surface du miroir se manifestant sous la forme d'un effet spin-Hall de la lumière [42]. Dans le travail, nous nous limitons à une interprétation purement modale et laissons de côté la discussion concernant le spin-orbite.

Le dernier point que nous avons aussi aborder pour obtenir une interprétation quantitative complète de notre expérience est de traiter l'effet de la fonction de filtre confocal de la fibre collectrice. La fibre monomode collecte et achemine le champ vers le photo-détecteur, elle le fait cependant en agissant comme un filtre spatial Gaussien. Pour notre configuration symétrique illustrée à la Fig. I.4, nous éclairons et collectons la lumière avec des fibres monomodes de taille de mode identique et avec des lentilles de collimation et de focalisation identiques. Le filtrage spatial est une convolution entre la distribution spatiale du champ au plan focal et le mode Gaussien de la fibre équivalant à une intensité de champ détectée par rapport à l'axe optique. Les résultats du calcul pour le champ sont les suivants (Annexe C.1). Nous obtenons d'abord la cartographie du champ de référence sans utiliser de polariseur ni de surface réfléchissante vue par le détecteur. Nous notons que la taille du faisceau au foyer semble maintenant être élargie d'un facteur $\sqrt{2}$ en comparaison avec la distribution de l'équation (4.7). Deuxièmement, nous avons trouvé que le filtrage confocal par convolution avec un mode Gaussien conduit à une matrice de Jones efficace modifiée pour la surface réfléchissante agissant sur le champ vu depuis le détecteur (voir Annexe C.2). Avec le filtrage confocal, les termes des champs Goos-Hänchen et Imbert-Fedorov (c'est-à-dire les deuxième et troisième termes des rhs dans l'équation) sont divisés par deux par rapport à l'équation (4.6) la matrice de Jones liée aux polariseurs et à la fuite de polarisation reste inchangée. Avec cette dernière correction, nous avons maintenant toutes les équations nécessaires pour simuler la transformation modale induite par une surface réfléchissante agissant sur un faisceau Gaussien polarisé et ce pour tout arbitraire polarisation et niveau de fuite de polarisation. Le premier résultat important que nous obtenons de

cette analyse est lorsque l'emplacement du centre de la fibre et l'axe du point focal coïncident le résultat est le même que celui trouvé dans l'analyse simplifiée des ondes planes du chapitre 3 et l'équation d'annulation de polarisation donnée dans l'équation (3.6) est fortuite. C'est le cas car la fonction de filtrage de l'agencement confocal élimine les modes de dépolarisation supérieurs. Sans le filtrage confocal (voir Annexe D), le champ dépolarisé collecté en imagerie à champ large du point focalisé limiterait l'extinction à 1.56×10^3 et 2.1×10^3 pour p et s polarisé faisceau respectivement. Cela démontre le rôle clé de l'arrangement confocal pour l'extinction de polarisation géante atteinte dans les mesures de fluorescence de résonance de pointe [8, 9, 16, 18].

Comme le montre la Fig. I.5, notre calcul numérique est en parfait accord avec nos mesures pour l'argent. Nous avons confirmé quantitativement ces résultats pour les miroirs de Bragg et les cubes séparateurs de faisceaux. Fig. I.6 et Fig. I.7 montrent l'évolution de la transformation de mode près de la condition de polarisation croisée pour une surface métallique. Dans notre expérience, nous mesurons les maxima typiques des lobes dans la plage de 0.3 à 1.4×10^{-6}. Pour une raison non encore élucidée, nos intensités maximales mesurées sont plus faibles que celles modélisées. Nous pensons qu'il nous manque encore une compréhension quantitative complète de la manière dont la fibre réceptrice filtre les modes non Gaussiens. En effet la sensibilité de notre configuration aurait dû permettre de détecter les modes de termes supérieurs TEM_{11} qui ont une symétrie xy. Ces modes proviennent de la taille finie du faisceau Gaussien le rendant naturellement divergent [43]. En fait, nous pouvons utiliser le formalisme exact développé ci-dessus pour montrer que de tels termes proviennent également de projections géométriques autour de l'axe optique. Cette fois, la projection n'implique aucune surface réfléchissante mais juste la divergence naturelle du faisceau avant la lentille, conduisant à un déphasage progressif gagné par chaque composante d'onde plane ici encore dépolarisant naturellement le faisceau (voir Annexe E). En utilisant ce résultat pour nos paramètres d'expérimentation, l'intensité du pic de mode devrait être de 3.8×10^{-7}, une valeur qui se situe bien dans notre plage de sensibilité. C'est un fait étonnant que nous n'ayons observé aucune trace de ce signal TEM_{11}. Il n'y a aucun doute cependant que ce mode est présent tel que mesuré dans [43], c'est pourquoi nous pensons que notre compréhension de la façon dont la fibre optique filtre le signal n'est pas encore complète.

I.5 Chapitre 5: Base de polarisation circulaire: directe imagerie de l'effet Imbert-Fedorov avec la microscopie confocale

En utilisant les résultats des chapitres précédents, nous déplaçons maintenant notre exploration vers un aspect plus fondamental de l'optique afin de tester la capacité prédictive du modèle et plus important encore la puissance expérimentale de la microscopie confocale à révéler des effets de polarisation très

faibles. En particulier ici, nous voulons nous concentrer sur la façon dont les surfaces réfléchissantes affectent la lumière polarisée de manière circulaire. Ce qui est bien établi, c'est qu'un faisceau laser à polarisation circulaire est réfléchi avec un décalage spatial transversal au plan d'incidence. Ce décalage d'Imbert-Fedorov, également connu sous le nom d' effet spin-Hall de la lumière, a été mesuré pour la première fois par C. Imbert [20] pour un faisceau laser de lumière polarisée circulairement dans un prisme de verre dans des conditions de réflectivité interne totale (Fig. I.8 (a) (b)). En fonction de la chiralité de sa polarisation circulaire, la trajectoire d'un faisceau polarisé circulairement se déplacera au-dessus ou au-dessous du plan d'incidence lorsqu'il est réfléchi sur une surface. Ce décalage est dû au couplage spin-orbite de la lumière à chaque réflexion [21, 38, 46, 47] et est normalement très petit, typiquement, plusieurs ordres de grandeur plus petit que la longueur d'onde du photon. Pour cette raison, il a auparavant nécessité des schémas de détection complexes limitant les investigations expérimentales détaillées. Ici, nous rapportons une nouvelle méthode pour mesurer et cartographier le décalage Imbert-Fedorov du faisceau laser Gaussien basé sur une technique de polarisation croisée en champ sombre dans un arrangement confocal.

Il existe une quantité considérable de littérature [42, 48] sur la mesure du décalage d'Imbert-Fedorov en utilisant l'état de polarisation linéaire de la lumière où le mode de faisceau réfléchi se divise en deux lobes situés au-dessus et au-dessous du plan de réflectivité, comme déjà discuté dans les chapitres précédents. À notre avis, cette approche n'est pas pertinente pour le couplage spin-orbite de la lumière car la notion de spin photonique est généralement liée à la polarisation circulaire. Parce que ce déplacement est perpendiculaire au plan de réflectivité, l'effet Imbert-Fedorov a été renommé en effet spin-Hall de la lumière par des auteurs comme *Onoda et al.* [38], *Bliokh et al.* [46, 47], *Aiello et al.* [49]. Ils ont interprété l'interaction spin-orbite de la lumière en termes de phases géométriques et de conservation du moment angulaire total de la lumière, comme déjà prédit par *Liberman et al.* En 1992 dans un milieu inhomogène [21]. Des preuves plus récentes de cet effet ont été montrées par *Bliokh et al.* En utilisant des réflexions multiples dans un verre cylindrique dans lequel le décalage spin-Hall s'accumule le long d'une trajectoire hélicoïdale (Fig. I.8(c)). Dans ce cas, la division du spin-hall est amplifiée par de multiples réflexions et devient perceptible à un nombre de tours plus élevé (Fig. I.8 (d)). Dans ce contexte, la rotation bien connue du plan de polarisation pour une trajectoire torsadée est expliquée à partir de la phase de Berry et de l'effet optique Magnus. La première observation de ce phénomène en cas de réflexion métallique a été démontrée dans [49] par Aiello et son équipe. Dans leur expérience (Fig. I.8(e)), ils ont mesuré directement le décalage d'une lumière polarisée circulairement au lieu de regarder la division d'une lumière polarisée linéairement. Le décalage détecté est de l'ordre du nanomètre et n'est pas mesurable à un angle d'incidence inférieur à 50° (Fig. I.8(f)).

Malgré les différentes approches (Fig. I.8) qui ont été développées pour

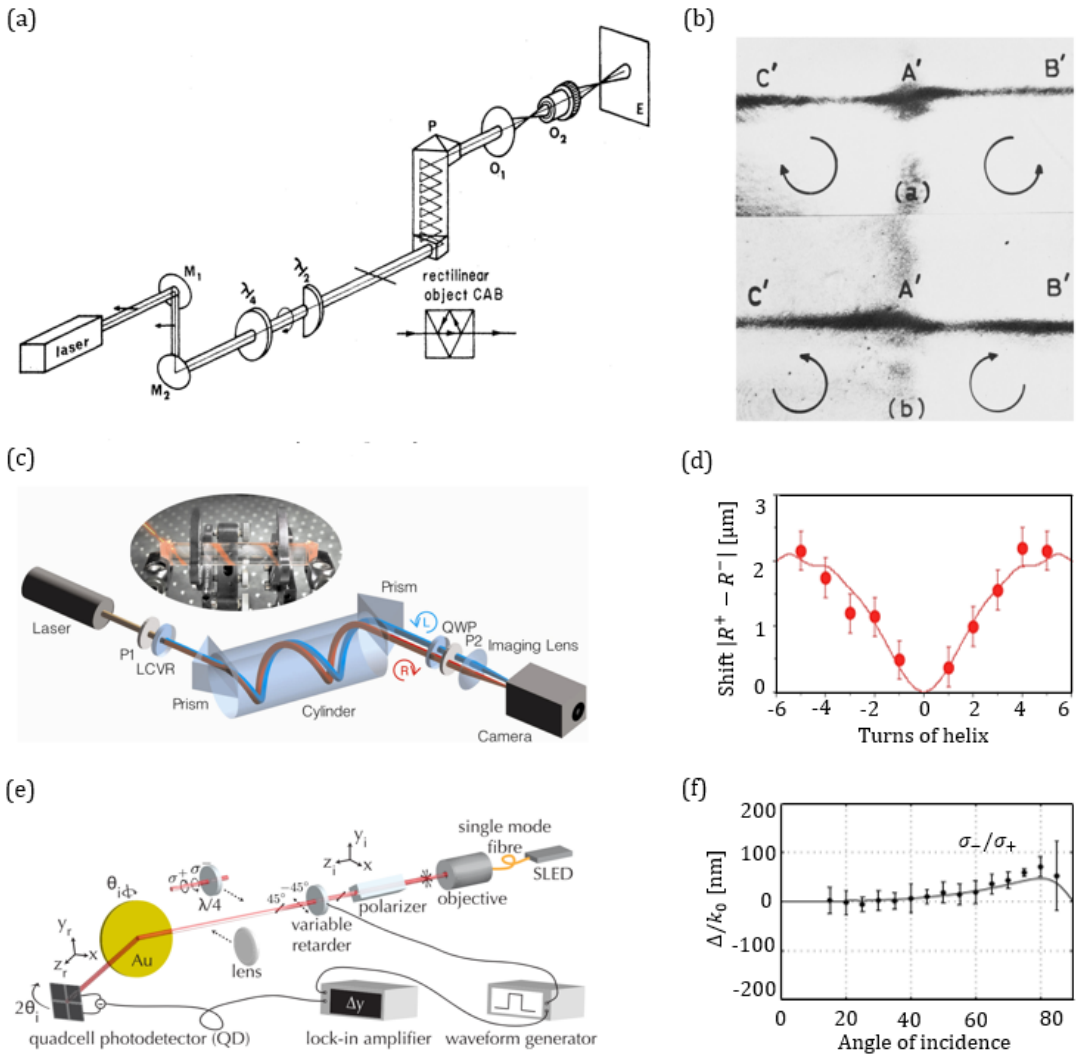

Figure I.8: (a) Dispositif expérimental global pour mesurer le décalage d'Imbert-Fedorov dans l'état de polarisation circulaire. Un faisceau laser, avec linéaire horizontal polarisation, traverse une lame quart d'onde puis une lame demi-onde couvrant la moitié du faisceau; le faisceau résultant, qui éclaire l'objet rectiligne CAB, est ainsi polarisé circulairement avec des hélicités opposées sur ses deux moitiés. Cela produira l'effet de doublement différentiel que nousont fait allusion à. Après avoir éclairé l'objet rectiligne CAB, le faisceau entre dans l'un de nos deux prismes multiplicateurs, et l'image de CAB est finalement observée. La haute luminosité du prisme P permet de projeter cette image sur un écran. (b) Image d'un objet rectiligne affichant le décalage transversal d'un faisceau polarisé de manière circulaire. Les états de polarisation circulaire des deux moitiés du faisceau sont indiqués. (Voir [20] pour plus de détails). (c) Mesure directe du spin-Hall de la lumière dans un cylindre de verre dans lequel le décalage s'accumule le long d'une trajectoire hélicoïdale. (d) Le décalage relatif entre les deux composantes de spin par rapport aux tours de l'hélice. (Voir [47] pour plus de détails). (e) Le montage optique pour mesurer le décalage différentiel de polarisation d'un faisceau réfléchi par un film d'or épais. (f) Décalage différentiel de polarisation mesuré entre σ_-/σ_+ lumière polarisée en fonction de l'angle d'incidence. (Voir [49] pour plus de détails).

étudier l'effet spin-Hall de la lumière, ce phénomène n'a pas été directement observé. Il n'a été mesuré que dans certaines situations très particulières telles que des réflexions multiples et un schéma de mesure faible. Cela limite l'utilisation de cet effet comme moyen pour générer, manipuler et détecter des photons polarisés en spin. La seule preuve à ce jour est une mesure d'un décalage différentiel de polarisation soit en faisant varier l'angle d'incidence ou la position du détecteur. L'incertitude associée à la mesure du décalage soulève de nombreuses questions quant à l'utilité et à la recherche expérimentale de cet effet. Dans ce travail, nous visons à faire un pont mental entre tous ces travaux et à fournir une explication claire des origines fondamentales du couplage spin-orbite de la lumière aux interfaces optiques. Pour cela, nous présentons une description mécanique de la trajectoire d'une onde plane à polarisation circulaire en fonction de son spin et de son moment angulaire orbital. Nous trouvons une formule simple du décalage Imbert-Fedorov qui révèle l'effet Hall de la lumière dépendant de la polarisation précédemment discuté dans la littérature. La même expression est dérivée en utilisant l'approche Maxwell complète qui est pertinente pour expliquer les subtilités importantes des déphasages induits par les coefficients de Fresnel lors de la réflexion. Nous avons mis en place une expérience simple et hautement reproductible pour observer et mesurer directement le décalage d'Imbert-Fedorov pour un faisceau Gaussien à polarisation circulaire.

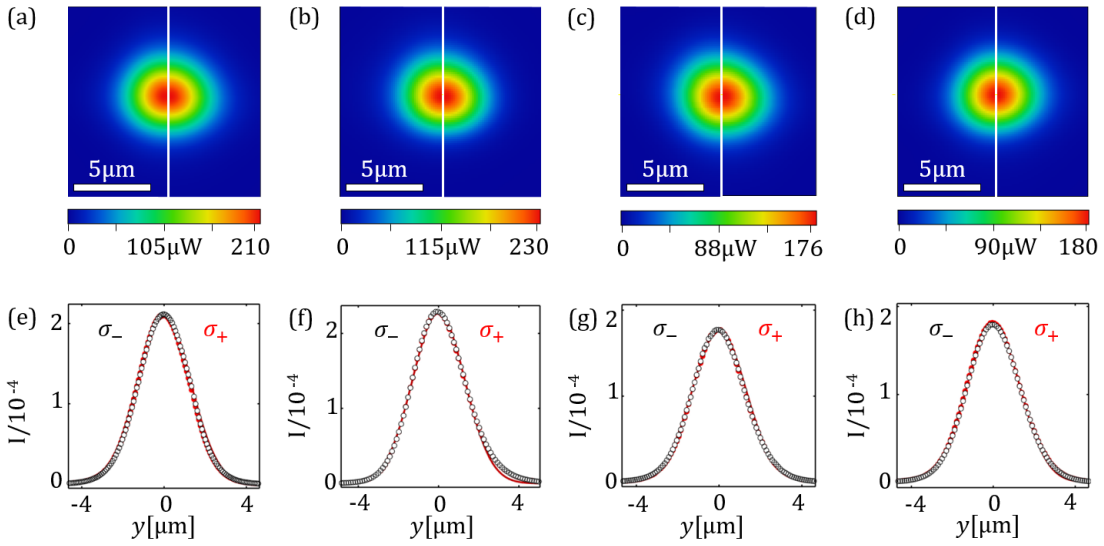

Figure I.9: Mesures en champ clair dans un arrangement confocal pour les angles d'incidence $\theta_i = 44°(a)(e), 30°(b)(f), 21°(c)(g), 13°(d)(h)$ en utilisant σ_+ et σ_- polarisation circulaire. Les mesures démontrent qu'aucun décalage technique parasite n'affecte notre configuration expérimentale dans des configurations pour lesquelles aucun décalage mesurable n'est attendu. Seul le demi-faisceau est affiché pour chaque polarisation circulaire σ_+ et σ_-. Les profils d'intensité mesurés pour la polarisation σ_+ (cercles rouges) et σ_- (cercles blancs) sont indiqués dans la ligne inférieure.

D'après le calcul pour une onde plane, le décalage Imbert-Fedorov devrait évoluer en $cotg\theta_i$, en d'autres termes, nous sommes obligés d'explorer la région

des petits angles pour pouvoir mesurer de grandes valeurs de décalage . Ici, nous nous sommes intéressés à observer le décalage aux angles d'incidence $\theta_i = 44°, 30°, 21°, 13°$. En pratique, nous avons mis en place quatre expériences différentes en modifiant l'angle d'incidence θ_i. En particulier, le miroir de test est déplacé par rapport au faisceau lumineux incident pour changer l'angle entre le faisceau et le miroir de surface de test. Pour chaque réglage d'angle d'incidence θ_i, nous avons mesurés l'intensité lumineuse, pour σ_+ et σ_- polarisation circulaire, mesurée en champ clair et sombre (Fig. I.9), respectivement. Seul un demi-faisceau est affiché pour chaque polarisation circulaire pour une meilleure illustration de l'observation directe du décalage d'Imbert-Fedorov. Dans tous les cas, le profil d'intensité en champ clair est essentiellement un faisceau gaussien TEM $_{00}$ pour la polarisation σ_+ et σ_-, respectivement. L'emplacement de l'intensité du pic est centré à 0, il n'y a pas de dérive parasite technique de position maximale du faisceau laser pendant le processus de balayage confocal qui pourrait être causée par un mauvais montage mécanique des pièces optomécaniques ou lors de la rotation de composants optiques tels que la quart d'onde. Ces mesures (Fig. I.9) ont pour but d'évaluer les performances de positionnement du faisceau de notre configuration et aussi la fidélité et la stabilité à long terme du décalage Imbert-Fedorov mesuré avec notre arrangement confocal en champ sombre. Nous avons vérifié expérimentalement la stabilité de la position des maxima du faisceau $\theta_i = 44°, 30°, 21°, 13°$ comme le montre la Fig. I.9(e)(f)(g)(h) attestant de la robustesse du montage expérimental.

En nous appuyant sur notre modèle détaillé pour les faisceaux laser Gaussiens dérivé pour la première partie de ce travail, nous avons vérifié quantitativement que le décalage augmente de manière significative en diminuant l'angle d'incidence, ceci, à notre connaissance, est un nouveau régime qui n'était pas explorée précédemment. Le modèle analytique montre un excellent accord avec nos mesures effectuées sur un miroir en argent. En particulier, le modèle révèle clairement un régime d'angle d'incidence plus faible en dessous duquel l'approche simpliste de la quasi-onde plane conduirait à une divergence non physique du décalage aux angles de fuite. Dans un régime d'angles aussi bas, notre modèle élimine cette divergence de décalage et prédit à la place une transformation modale des photons minoritaires réfléchis vers le mode Hermite-Gaussien supérieur suivant d'une manière très similaire à celle explorée dans la première partie de ce travail. Les premières données indiquent la transition vers un tel régime.

En conclusion, nous avons présenté une nouvelle méthode pour mesurer et cartographier le décalage Imbert-Fedorov basée sur une technique de polarisation croisée en champ noir dans un arrangement confocal. Dans notre configuration de champ sombre proposée sous polarisation circulaire, la majorité des photons réfléchis sur une surface qui ne contribuent pas au décalage sont filtrés. Les photons minoritaires possèdent la chiralité appropriée pour le couplage spin-orbite de la lumière permettant ainsi le grossissement du décalage Imbert-Fedorov de plusieurs ordres de grandeur. Nous avons vérifié que le

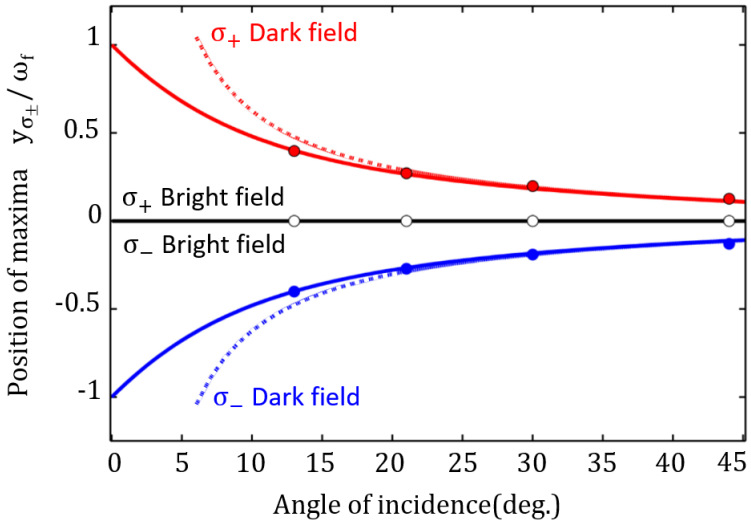

Figure I.10: Décalage Imbert-fedorov mesuré pour une polarisation circulaire $\sigma_\pm$ en unité de rayon de taille du faisceau ω_f dans le cas d'un miroir argenté et pour une longueur d'onde laser $\lambda = 905nm$. On trace la position des maxima d'intensité pour une onde plane (trait en pointillé) et un faisceau gaussien (trait plein) réfléchi par un miroir d'argent en fonction de l'excitation et de la détection de polarisation. $\sigma_\pm$ Dark-field et $\sigma_\pm$ Bright-field désignent le dark-field ($\sigma_\pm M \sigma_\pm$) et le Bright-field ($\sigma_\pm M \sigma_\mp$) configurations respectivement, lorsque le miroir (M) est placé entre deux polariseurs circulaires. Les mesures à $\theta_i = 13°$ montrent clairement le départ de la divergence d'approximation de l'onde plane (trait en pointillé) pour de faibles angles d'incidence. Le modèle est en très bon accord (trait plein).

décalage hors plan d'incidence mesuré de cette manière est une conséquence directe de la conservation du moment cinétique total.

I.6 Chapitre 6: Conclusion et perspectives

Notre étude fournit une boîte à outils robuste pour une nouvelle façon de faire des expériences de spectroscopie de fluorescence et de polarimétrie à l'aide de la microscopie confocale. Nous avons exposé une méthode expérimentale systématique basée sur un agencement de microscopie confocale pour obtenir une amélioration géante de l'extinction de polarisation croisée en champ sombre et ce jusqu'à 3 ordres de grandeur et éventuellement au-delà. Nous avons constaté que l'effet exploite les propriétés matérielles d'une surface ou d'une interface sous condition de réflectivité interne totale notamment. En termes plus généraux, l'effet s'est avéré être entièrement régi par la différence de phase, telle qu'induite par les cubes séparateurs de faisceaux et les miroirs de Bragg, entre la réflectivité des composantes lumineuses polarisées dans et hors du plan d'incidence. Maintenant que le principe de base de l'annulation de la fuite de polarisation est établi, il existe des options pour améliorer la limite de détection expérimentale du rapport d'extinction de polarisation croisée. Tout d'abord,

il est possible d'améliorer le rapport signal sur bruit. En général, il est utile d'augmenter la puissance d'entrée optique par un meilleur alignement. Cependant, cela dépend principalement de l'application. Dans les mêmes cas, les lasers bruyants ne peuvent pas être stabilisés et un type et un modèle appropriés de photo-détecteur peuvent (et ne peuvent pas) améliorer le rapport signal / bruit. La deuxième possibilité consiste à amplifier la précision de l'angle de rotation. Il est démontré au chapitre I.4 qu'une résolution de positionnement de 10^{-6} degrés permet de mesurer une valeur de rapport d'extinction au niveau de 10^{11} et au-delà. Il est pratiquement possible d'obtenir une résolution de rotation de sous-taille avec des contrôleurs d'attocube sélectionnés. Une solution déjà existante est le rotateur à roulement ECR4040/Al/NUM/RT avec une ouverture intégrée de 1/2", adapté aux expériences optiques. Il est conçu pour des conditions ambiantes avec une position angulaire fine de 0.04 m°.

De plus, nous avons également présenté l'analyse modale théorique de la réflectivité du faisceau. En effet, la modélisation de cet effet nous a conduit à simuler et cartographier dans les moindres détails la transformation de faisceaux Gaussiens proches de la polarisation croisée en modes supérieurs d'Imbert-Fedorov, une physique régie essentiellement par la divergence finie d'un faisceau Gaussien réfléchissant sur une surface. Jusqu'à présent, les résultats ont été très prometteurs jusqu'à la transformation du premier ordre en x et y. Une application potentielle prometteuse de notre approche serait de simuler et de cartographier la transformation de faisceaux Gaussiens à des modes d'ordre supérieur. Jusqu'à présent, nous n'avons observé aucune trace du signal de mode TEM_{11}. Il n'y a aucun doute cependant que ce mode est présent tel que mesuré dans [43], c'est pourquoi nous pensons que notre modèle n'est pas encore complet. Les travaux futurs devraient également se concentrer sur l'amélioration de la qualité du taux d'extinction dans un dispositif confocal du monde réel composé de plusieurs miroirs et cubes séparateurs de faisceaux de géométries différentes et complexes. Nous sommes convaincus que notre modèle servira de base pour la mise en place de la pierre angulaire de tout futur système de spectroscopie optique. Le présent modèle est basé sur une approche d'expansion d'onde plane de Maxwell pure. L'étape suivante consiste à inclure la connexion entre l'effet Imbert-Fedorov et les phases géométriques. Ceci est absolument essentiel dans la conception et la conception de dispositifs optiques modernes basés sur le spin.

Dans le chapitre I.5, nous avons présenté une observation directe du décalage Imbert-Fedorov, c'est-à-dire l'effet spin-Hall pour le spin vers le haut et vers le bas de la lumière (polarisation circulaire). Cela n'a jamais été clairement vu dans un manuel. Nous avons démontré que l'Imbert-Fedorov, comme il est dit dans les manuels scolaires, que (i) un faisceau laser se déplace hors du plan d'incidence spéculaire lorsque la lumière heurte une polarisation circulaire et est détectée dans la même polarisation circulaire. (ii) Le signe du décalage est donné par la chiralité. Il s'agit d'une nouvelle découverte en microscopie et peut conduire à des problèmes de mesure ou à des opportunités pour le chercheur

effectuant des mesures sous polarisation circulaire. Nous avons montré à la fois théoriquement et expérimentalement, que l'effet est une conséquence de la conservation du moment cinétique total entre le faisceau incident et réfléchi. Pour être convaincant, nous avons également vérifié la stabilité maximale de la position du faisceau de notre installation. La situation idéalisée d'une lumière d'onde plane polarisée circulaire et d'un miroir parfait hautement réfléchissant est parfaitement prédictif, à savoir qu'il prédit un décalage de déplacement typiquement dépendant de la co-tangente de l'angle d'incidence $cotg\theta_i$. Ce beau résultat est issu d'un calcul très simple qui considère le conservation du moment cinétique de la lumière projetée sur l'axe z perpendiculaire au miroir. Dans ce travail et dans des expériences de microscopie réelles, nous nous demandons comment cela s'applique à un faisceau focalisé Gaussien dans une configuration confocale. Pour répondre à cela, nous avons fait notre modèle calculs d'abord dans la limite de NA plus petit et ont trouvé exactement le même résultat pour le décalage de l'emplacement du maximum de l'intensité du faisceau. Nous avons donc maintenant un régime pour lequel un mode Gaussien semble agit comme une onde plane. Nous vérifions notre théorie par des mesures expérimentales à différents angles d'incidence. Notre approche expérimentale présente un certain nombre de similitudes avec la technique de mesure faible, la principale différence est que nous mesurons à une condition de polarisation croisée exacte. Des recherches expérimentales supplémentaires sont nécessaires pour comprendre l'origine de la faible amplification de la mesure du décalage déjà rapporté dans la littérature [42, 48]. C'est une question importante pour les recherches futures.

Ce travail ouvre la voie à la conception méthodique de microscopes à fluorescence à résonance laser sensible avec une extinction de fond extrême, pour une large gamme d'applications en optique quantique et en physique du solide. Les nouvelles méthodes développées pour ce travail peuvent également être appliquées pour mesurer les propriétés optiques des matériaux et les applications de polarimétrie.

Bibliography

[1] Benelajla, M., Kammann, E., Urbaszek, B. & Karrai, K. The physical origins of extreme cross-polarization extinction in confocal microscopy. *arXiv:* **2004.13564** (2020). URL https://arxiv.org/abs/2004.13564.

[2] Aharonovich, I., Englund, D. & Toth, M. Solid-state single-photon emitters. *Nature Photonics* **10**, 631 (2016).

[3] Högele, A. *et al.* Dynamic nuclear spin polarization in the resonant laser excitation of an *InGaAs* quantum dot. *Physical Review Letters* **108**, 197403 (2012).

[4] Paillard, M. *et al.* Spin relaxation quenching in semiconductor quantum dots. *Physical Review Letters* **86**, 1634 (2001).

[5] Högele, A. *et al.* Voltage-controlled optics of a quantum dot. *Physical Review Letters* **93** (2004).

[6] Atatüre, M. *et al.* Quantum-dot spin-state preparation with near-unity fidelity. *Science* **312**, 551–553 (2006).

[7] Gerardot, B. D. *et al.* Optical pumping of a single hole spin in a quantum dot. *Nature* **451** (2008).

[8] Vamivakas, A. N., Zhao, Y., Lu, C.-Y. & Atatüre, M. Spin-resolved quantum-dot resonance fluorescence. *Nature Physics* **5**, 198–202 (2009).

[9] Kaldewey, T. *et al.* Far-field nanoscopy on a semiconductor quantum dot via a rapid-adiabatic-passage-based switch. *Nature Photonics* **12**, 68–72 (2018).

[10] Nguyen, H.-S. *et al.* Ultra-coherent single photon source. *Applied Physics Letters* **99**, 261904 (2011).

[11] Najer, D. *et al.* A gated quantum dot strongly coupled to an optical microcavity. *Nature* 1–1 (2019).

[12] Kumar, S. *et al.* Resonant laser spectroscopy of localized excitons in monolayer wse 2. *Optica* **3**, 882–886 (2016).

[13] Nowak, A. *et al.* Deterministic and electrically tunable bright single-photon source. *Nature communications* **5**, 1–7 (2014).

[14] Müller, M., Bounouar, S., Jöns, K. D., Glässl, M. & Michler, P. On-demand generation of indistinguishable polarization-entangled photon pairs. *Nature Photonics* **8**, 224 (2014).

[15] Schöll, E. *et al.* Resonance fluorescence of GaAs quantum dots with near-unity photon indistinguishability. *Nano Letters* **19**, 2404–2410 (2019).

[16] Kuhlmann, A. V. *et al.* Charge noise and spin noise in a semiconductor quantum device. *Nature Physics* **9**, 570–575 (2013).

[17] Ollivier, H. *et al.* Reproducibility of high-performance quantum dot single-photon sources. *ACS Photonics* **7**, 1050–1059 (2020). URL https://doi.org/10.1021/acsphotonics.9b01805.

[18] Kuhlmann, A. V. *et al.* A dark-field microscope for background-free detection of resonance fluorescence from single semiconductor quantum dots operating in a set-and-forget mode. *Review of scientific instruments* **84**, 073905 (2013).

[19] Fedorov, F. I. K teorii polnogo otrazheniya. *Doklady Akademii Nauk SSSR* **105**, 465–468 (1955).

[20] Imbert, C. Calculation and experimental proof of the transverse shift induced by total internal reflection of a circularly polarized light beam. *Physical Review D* **5**, 787 (1972).

[21] Liberman, V. S. & Zel'dovich, B. Y. Spin orbit interaction of a photon in an inhomogeneous medium. *Physical Review A* **46**, 5199 (1992).

[22] Bliokh, K. Y., Rodríguez-Fortuño, F. J., Nori, F. & Zayats, A. V. Spin-orbit interactions of light. *Nature Photonics* **9**, 796 (2015).

[23] Ozawa, T. *et al.* Topological photonics. *Rev. Mod. Phys.* **91**, 015006 (2019).

[24] Benelajla, M., Kammann, E., Urbaszek, B. & Karrai, K. Modal imaging of a laser gaussian-beam reflected off a surface. *Proceedings* **11485** (114850E (2020)). URL https://doi.org/10.1117/12.2568365.

[25] Mollow, B. R. Power spectrum of light scattered by two-level systems. *Physical Review Letters* **188**, 1969–75 (1969).

[26] Shree, S. *et al.* High optical quality of MoS2 monolayers grown by chemical vapor deposition. *2D Materials* **7** (2019).

[27] Stern, F. Elementary theory of the optical properties of solids. In *Solid state physics*, vol. 15, 299–408 (Elsevier, 1963).

[28] Johnson, P. B. & Christy, R.-W. Optical constants of the noble metals. *Physical review B* **6**, 4370 (1972).

[29] Novotny, L. & Hecht, B. *Principles of nano-optics* (Cambridge university press, 2012).

[30] Goodman, J. Introduction to fourier optics (1968).

[31] Aiello, A. & Woerdman, H. The reflection of a maxwell-gaussian beam by a planar surface. *arXiv preprint arXiv:0710.1643* (2007).

[32] Goos, F. & Hänchen, H. Ein neuer und fundamentaler versuch zur totalreflexion. *Annalen der Physik* **436**, 333–346 (1947).

[33] Artmann, K. V. Berechnung der seitenversetzung des total-reflektierten strahles. *Ann. Phys. Leipzig* **2**, 87–102 (1948).

[34] Tamir, T. Nonspecular phenomena in beam fields reflected by multilayered media. *J. Opt. Soc. Am. A* **3**, 558–565 (1986).

[35] Horovitz, B. R. & Tamir, T. Lateral displacement of a light beam at a dielectric interface. *J. Opt. Soc. Am.* **61**, 586–594 (1971).

[36] Ra, J. W., Bertoni, H. L. & Felsen, L. B. Reflection and transmission of beams at a dielectric interface. *SIAM J. Appl. Math.* **24**, 396–413 (1973).

[37] Nasalski, W. Longitudinal and transverse effects of nonspecular reflection. *J. Opt. Soc. Am. A* **13**, 172–181 (1996).

[38] Onoda, M., Murakami, S. & Nagaosa, N. Hall effect of light. *Physical Review Letters* **93**, 083901 (2004).

[39] Aiello, A. & Woerdman, J. Role of beam propagation in goos–hänchen and imbert–fedorov shifts. *Optics letters* **33**, 1437–1439 (2008).

[40] Aharonov, Y., Albert, D. Z. & Vaidman, L. How the result of a measurement of a component of the spin of a spin-1/2 particle can turn out to be 100. *Physical Review Letters* **60**, 1351 (1988).

[41] Duck, I., Stevenson, P. M. & Sudarshan, E. The sense in which a" weak measurement" of a spin-1/2 particle's spin component yields a value 100. *Physical Review D* **40**, 2112–2117 (1989).

[42] Hosten, O. & Kwiat, P. Observation of the spin hall effect of light via weak measurements. *Science* **319**, 787–790 (2008).

[43] Erikson, W. L. & Singh, S. Polarization properties of maxwell-gaussian laser beams. *Phys. Rev. E* **49**, 5778–5786 (1994).

[44] Merano, M. *et al.* Observation of goos-hänchen shifts in metallic reflection. *Physical Review Letters* **15**, 15928–15934 (2007).

[45] Karrai, K. & Miles, H. Inertial rotation device. *Patent No:* (Sep.6, 2005). URL https://patentimages.storage.googleapis.com/a7/40/8d/4a376e806e8773/US6940210.pdf.

[46] Bliokh, K. Y. & Bliokh, Y. Conservation of angular momentum, transverse shift, and spin hall effect in reflection and refraction of an electromagnetic wave packet. *Phys. Rev. Lett.* **96**, 073903 (2006).

[47] Bliokh, K. Y., Niv, A., Kleiner, V. & Hasman, E. Geometrodynamics of spinning light. *Nature Photonics* **2**, 748–753 (2008).

[48] Ling, X. *et al.* Recent advances in the spin hall effect of light. *IOP Publishing Ltd* **80** (2017).

[49] Hermosa, N., Nugrowati, A. M., Aiello, A. & Woerdman, J. Spin hall effect of light in metallic reflection. *Optics letters* **36**, 3200–3202 (2011).